

# Theory

- Airborne
- Spaceborne
- Water
- Geology
- Biodiversity

A project funded by >>



A project of >>



---

---

---

---

---

# Table of Contents

<b>List of Figures</b> .....	<b>6</b>
<b>List of Tables</b> .....	<b>10</b>
<b>Foreword</b> .....	<b>11</b>
<b>1 Short introduction for busy decision-makers</b> .....	<b>12</b>
<b>2 Imaging spectroscopy</b> .....	<b>13</b>
2.1 Physics of spectroscopy .....	13
2.1.1 The electromagnetic radiation EMR .....	13
2.1.2 Interaction of radiation with matter .....	14
2.1.3 Factors influencing spectral reflectance measurements .....	16
2.2 Imaging spectroradiometers .....	18
2.2.1 Airborne .....	21
2.2.1.1 Current .....	21
2.2.1.2 Future .....	21
2.2.2 Spaceborne .....	22
<b>3 Flight planning</b> .....	<b>27</b>
3.1 The mission area .....	27
3.2 Timing and illumination geometry .....	27
3.3 Spectral and spatial resolution and sensor choice .....	28
3.4 Other factors affecting campaign planning .....	29
3.5 Auxiliary equipment and data .....	30
3.5.1 Airborne equipment .....	30
3.5.1.1 Inertial Navigation System .....	30
3.5.1.2 Global Positioning System .....	31
<b>4 Spaceborne data availability</b> .....	<b>35</b>
4.1 Satellite sensor characteristics (spatial, spectral, etc.) .....	35
4.1.1 Water .....	35
4.1.2 Land .....	36
<b>5 Field measurements</b> .....	<b>38</b>
5.1 Planning .....	38
5.2 Equipment .....	38
5.2.1 Field spectroradiometers (FieldSpec Pro FR, GER1500, GER IRIS MARK V, PIMA, OCEAN OPTICS, RAMSES) .....	38
5.2.1.1 Sun photometer (Microtops II) .....	44
5.2.1.2 Global Positioning System .....	45
5.3 Other auxiliary data .....	47

<b>6</b>	<b>Sensor calibration</b>	<b>48</b>
6.1	Lab calibration	48
6.1.1	Geometric calibration	48
6.1.2	Spectral calibration	48
6.1.3	Radiometric calibration	48
6.2	Bundle adjustment	49
6.3	In-flight calibration	49
6.4	Vicarious calibration	49
<b>7</b>	<b>Geometric correction</b>	<b>50</b>
7.1	Geometric distortions in airborne imagery	50
7.2	Parametric geometric correction	52
7.3	Ground control points/polynomial mathematical models	52
7.4	Geometric correction of spaceborne imagery	54
7.4.1	Auxiliary data for georeferencing of spaceborne imagery	54
<b>8</b>	<b>Atmospheric correction</b>	<b>55</b>
8.1	Land	55
8.1.1	Airborne and spaceborne	55
8.1.2	Scene-derived corrections	56
8.1.2.1	Flat Field	56
8.1.2.2	Internal Average Relative Reflectance (IARR)	56
8.1.3	Empirical Line Calibration	56
8.1.4	Radiative transfer codes	57
8.2	Atmospheric correction for water	57
8.2.1	Description of problem	57
8.2.2	Atmospheric correction of airborne data for water applications	59
8.2.3	Atmospheric correction of spaceborne data for water applications	60
<b>9</b>	<b>Data analysis and validation</b>	<b>63</b>
9.1	Land	63
9.1.1	Minimum Noise Fraction, Pixel Purity Index, Endmember selection	63
9.1.2	Discrete Wavelet Transform	64
9.1.3	Abundance techniques	67
9.1.3.1	Linear Spectral Unmixing	67
9.1.3.2	Mixture Tuned Matched Filtering	68
9.1.3.3	Spectral Feature Fitting	68
9.1.4	Classification techniques	68
9.1.4.1	Spectral Angle Mapper	68
9.1.4.2	Fisher's Linear Discriminant	69
9.1.5	Accuracy assessment	70
9.1.5.1	Confusion matrix	70
9.1.5.2	Leave-one-out	71

9.2	Water data analysis and quality control .....	71
9.2.1	Chlorophyll <i>a</i> concentration using blue-green ratios .....	71
9.2.2	Chlorophyll <i>a</i> concentration using red and near-infrared ratios .....	72
9.2.3	Chlorophyll retrieval from multi-band algorithms .....	72
9.2.4	Total suspended matter .....	72
9.2.5	Quality assessment .....	73
<b>10</b>	<b>Water .....</b>	<b>75</b>
10.1	Spectral properties of water bodies .....	75
10.1.1	Introduction: water and its coloured constituents .....	75
10.1.2	Applications, parameters and limitations .....	75
10.2	A simple model of water colour .....	76
10.2.1	Reflectance definition and assumptions .....	76
10.2.2	The HYPERTEACH ocean colour model .....	77
<b>11</b>	<b>Geology .....</b>	<b>80</b>
11.1	Spectral properties of soil, rocks, minerals .....	80
11.1.1	Reflectance properties of minerals .....	82
11.1.2	Reflectance properties of rocks .....	85
11.2	Spectral profiles and libraries in geology .....	86
11.2.1	Mineral mapping with spectral libraries .....	86
11.2.2	Spectral analysis methods in geology .....	87
11.2.3	Linear spectral unmixing .....	88
11.2.4	Partial unmixing for geologic applications .....	88
11.3	General analysis tools .....	89
11.4	Case study: The Cuprite test site (US, Nevada) .....	90
<b>12</b>	<b>Biodiversity applications .....</b>	<b>94</b>
12.1	Spectral properties of vegetation .....	94
12.2	Classification of vegetation species .....	95
12.2.1	Introduction .....	95
12.2.2	Airborne hyperspectral campaign .....	95
12.2.3	Pre-processing .....	96
12.2.4	Vegetation mask .....	97
12.2.5	Field survey .....	97
12.2.6	Spectral Angle Mapper Classification .....	99
<b>13</b>	<b>REFERENCES .....</b>	<b>102</b>
<b>14</b>	<b>ANNEX .....</b>	<b>106</b>
14.1	ASD2 Spectroradiometer: IRRADIANCE – measurements .....	106
14.1.1	Equipment .....	106
14.1.2	Setup .....	106
14.1.3	Measurements .....	106

14.2 ASD2 Spectroradiometer: REFLECTANCE – measurements .....	106
14.2.1 Equipment .....	106
14.2.2 Setup .....	107
14.2.3 Measurements .....	107
14.3 GER1500 Spectroradiometer: REFLECTANCE – measurements .....	107
14.3.1 Equipment .....	107
14.3.2 Setup .....	108
14.4 MICROTOPS II SUN PHOTOMETER - measurements .....	108
14.4.1 Before you leave the office .....	108
14.4.1.1 Switching on .....	108
14.4.1.2 Setting the time and date .....	108
14.4.1.3 Connecting the sun photometer to the computer and save location parameters Optional (recommended) .....	109
14.4.2 Collecting measurements in the field .....	109
14.4.2.1 Switching on .....	109
14.4.2.2 Set the location .....	109
14.4.2.3 Collecting measurements .....	111
14.4.3 Downloading the data to PC .....	111
14.5 GER1500-measurements .....	112
14.5.1 Stand-Alone Measurements .....	112
14.5.2 Computer Measurements .....	112
14.6 Trimble GeoXT GPS–measurements .....	113
14.6.1 Equipment .....	113
14.6.2 GPS measurements (points) .....	113
14.6.3 Trimble GeoXt GPS–measurements with real-time correction .....	113
14.6.3.1 Equipment .....	113
14.6.3.2 Activate Bluetooth on GSM .....	114
14.6.3.3 Activate Bluetooth on Trimble .....	114
14.6.3.4 Preparations of the GPS measurements .....	114
14.6.3.5 Checking the status of the real-time connection .....	114
14.6.4 Trimble GeoXT GPS–measurements – Transfer results .....	115
14.6.4.1 Software .....	115
14.6.4.2 Transfer results .....	115

<b>ACRONYMS .....</b>	<b>116</b>
-----------------------	------------

<b>Footnotes .....</b>	<b>119</b>
------------------------	------------



---

---

---

---

---

## List of Figures

Figure 1: Principle of imaging spectroscopy. ....	13
Figure 2: Energy density of a black body at different temperatures as a function of wavelength. ....	14
Figure 3: Energy interactions with matter. ....	14
Figure 4: Reflectance spectra of minerals and vegetation. ....	15
Figure 5: Specular (a) and diffuse (b) reflection. ....	16
Figure 6: AVIRIS average spectral radiance curve on a bright target. (Source: <a href="http://www.microimages.com/getstart/pdf/hyprspec.pdf">http://www.microimages.com/getstart/pdf/hyprspec.pdf</a> ) ....	16
Figure 7: Solar irradiance spectra for the top of the atmosphere (top le; also called extraterrestrial sun irradiance) and at ground level (bottom ls); the position of the visual wavelength range is indicated in gray. ....	18
Figure 8: Incidence angles of direct sun illumination.(Source: <a href="http://www.microimages.com/getstart/pdf/hyprspec.pdf">http://www.microimages.com/getstart/pdf/hyprspec.pdf</a> ) ....	18
Figure 9: Illustration of spectral sampling interval and spectral resolution (Source: Technical Guide 3 <sup>rd</sup> Ed. Section 3-1). ....	19
Figure 10: Schematic view of the optical system of the CASI-2 sensor. Source: ITRES, Research Ltd ( <a href="http://www.itres.com">www.itres.com</a> ). ....	19
Figure 11: Whiskbroom (left) and pushbroom (right) principle (Nieke, 1997). ....	20
Figure 12: Schematic optical design of the APEX instrument. ....	22
Figure 13: Aeronautical chart of Brussels National Airport and surroundings. ....	27
Figure 14: Aircraft flying within the solar plane. Hence the stronger reflection appears towards the sun and lowest reflection in the opposite direction (Ranson et al., 1994). ....	28
Figure 15: Relation between spatial resolution, height and IFOV of a whiskbroom sensor. ....	29
Figure 16: The six parameters of freedom. A aircraft's actual spatial behaviour or movement can be described with three translational and three rotational components. (Source: <a href="http://www.electronic-engineering.ch/study/ins/ins.html">http://www.electronic-engineering.ch/study/ins/ins.html</a> ) ....	30
Figure 17: Representation of the aircraft's actual spatial situation ( $x''', y''', z'''$ ) referring to the initial system ( $x, y, z$ ) by using 'Euler'-angles. ....	31
Figure 18: The GPS satellite constellation. ....	32
Figure 19: GPS principle. ....	32
Figure 20: Set of possible positions of a GPS receiver relative to a single GPS satellite. After Trimble Navigation Limited. ....	33
Figure 21: Set of possible positions of a GPS receiver relative to two GPS satellites. After Trimble Navigation Limited. ....	33
Figure 22: Set of possible positions of a GPS receiver relative to three GPS satellites. After Trimble Navigation Limited. ....	33
Figure 23: Picture of FieldSpec Pro FR ( <a href="http://www.asdi.com/">http://www.asdi.com/</a> ). ....	39
Figure 24: Picture of the Li-Cor 1800 12S Integrating Sphere. ....	40
Figure 25: Picture of High Intensity Contact Probe ( <a href="http://www.asdi.com/">http://www.asdi.com/</a> ). ....	40
Figure 26: Picture of GER1500 spectroradiometer. ....	40
Figure 27: The optical system of the GER IRIS Mark V (GER users manual, 1995). ....	41
Figure 28: Deployment of the GER IRIS Mark V in the field (left) and in the lab (right). ....	41

Figure 29: Picture of the Ocean Optics spectroradiometer setup. ....	43
Figure 30: PIMA spectroradiometer ( <a href="http://www.pimausa.com/pima2.html">http://www.pimausa.com/pima2.html</a> ). ....	43
Figure 31: Picture of RAMSES ARC hyperspectral radiance sensor ( <a href="http://www.trios.de">www.trios.de</a> ). ....	44
Figure 32: Picture of the Microtops II sun photometer. ....	45
Figure 33: Trimble GeoXT handheld GPS. ....	46
Figure 34: Leica SR530 base station GPS. ....	46
Figure 35: Relation between DN and radiance. ....	48
Figure 36: Roll, pitch, yaw. (Source <a href="http://virtualskies.arc.nasa.gov/aeronautics/tutorial/motion.html">http://virtualskies.arc.nasa.gov/aeronautics/tutorial/motion.html</a> ) ....	50
Figure 37: Scan-angle dependent roll distortion. (Source: <a href="http://www.cis.rit.edu/research/thesis/bs/1998/kopacz/thesis.html">www.cis.rit.edu/research/thesis/bs/1998/kopacz/thesis.html</a> ). ....	50
Figure 38: The effects of roll, pitch and yaw on image geometry (Source: <a href="http://www.cnr.berkeley.edu/~gong/textbook/chapter4/html/sect42.htm">http://www.cnr.berkeley.edu/~gong/textbook/chapter4/html/sect42.htm</a> ). ....	51
Figure 39: Relief displacement. ....	51
Figure 40: Nearest neighbouring method (Source : <a href="http://www.nr.usu.edu/Geography-Department/rsgis/RSCC/v6.2/nn.html">http://www.nr.usu.edu/Geography-Department/rsgis/RSCC/v6.2/nn.html</a> ). ....	54
Figure 41: Plot of atmospheric transmittance versus wavelength. (Source : <a href="http://www.microimages.com/getstart/pdf/hyrspec.pdf">http://www.microimages.com/getstart/pdf/hyrspec.pdf</a> ) ....	55
Figure 42: Sources of radiation received by a remote sensor. ....	56
Figure 43: Reflectance conversion parameters for a single image band using known target reflectance values. (Source : <a href="http://www.microimages.com/getstart/pdf/hyrspec.pdf">http://www.microimages.com/getstart/pdf/hyrspec.pdf</a> ). ....	57
Figure 44: Photons paths from sun to sensor with a single scattering event in the atmosphere, at the air-water interface or in the water body. ....	58
Figure 45: Screen print of the graphical user interface of the WATCOR software used for atmospheric correction of airborne imagery. ....	60
Figure 46: The MNF transform: (a) RGB display of original input image (96 spectral bands), (b) MNF band 2, (c) MNF band 8 and (d) MNF band 30. ....	63
Figure 47: Plot of eigenvalues versus MNF output band showing approximate signal to noise cut-off. ....	64
Figure 48: Single two-MNF component plot showing how the Pixel Purity Index determines potential extreme or pure image pixels. (Source: <a href="http://www.microimages.com/getstart/pdf/hyrspec.pdf">http://www.microimages.com/getstart/pdf/hyrspec.pdf</a> ). ....	64
Figure 49: Example of a one dimensional signal (amplitude vs. time). ....	65
Figure 50: Low-pass (h) and high-pass (g) filter, followed by down sampling with factor 2. ....	66
Figure 51: Analysis Filter Bank computing the Discrete Wavelet Transform. ....	66
Figure 52: Typical vegetation signature in spectral domain (left) and its derived DWT coefficients (right). ....	67
Figure 53: The linear spectral unmixing principle. (Source: <a href="http://www.ltid.inpe.br/tutorial/images/tut14.htm">www.ltid.inpe.br/tutorial/images/tut14.htm</a> ) ....	67
Figure 54: Visualization of the Spectral Angle, $\theta$ , between two 3-D reflectance spectra, $t$ = target spectrum, $r$ = reference spectrum, using the reflectance at spectral bands $\lambda_1, \lambda_2, \lambda_3$ . ....	69
Figure 55: Class assignment in SAM. ....	69
Figure 56: LDA, special case of two classes (red and blue) in two dimensions. The optimal projection vector $w$ is shown at the right. ....	70

Figure 57: A coastal water front marking an abrupt change in water colour because of a change in total suspended matter concentration. Other parameters such as salinity, temperature, etc. often change abruptly at such fronts. ....	73
Figure 58: Typical reflectance spectra for water of various composition: very clear, blue water (black), clear water with some phytoplankton (blue), water with low particle concentration but high chlorophyll <i>a</i> (green), water with high total suspended ....	77
Figure 59: Electronic, vibrational and rotational transitions related to wavelength and frequency (from Drury, 1993 and Atzberger) . ....	80
Figure 60: Electronic transitions. ....	80
Figure 61: Possible vibrational states in a water molecule. Top: energy and energy levels; Middle: vibrational mode (in sense of arrow); Bottom: resulting spectrum. ....	81
Figure 62: Rotational energy levels for one atom (hydrogen) and several (sodium) electrons. Some possible transitions are indicated. ....	81
Figure 63: Reflectance spectra of quartz and feldspars. (Wavelength in $\mu\text{m}$ ) ....	82
Figure 64: Reflectance spectra of carbonates. (Wavelength in $\mu\text{m}$ ) ....	83
Figure 65: Reflectance spectra of ferromagnesians. (Wavelength in $\mu\text{m}$ ) ....	83
Figure 66: Reflectance spectra of clay minerals and mica's. (Wavelength in $\mu\text{m}$ ) ....	84
Figure 67: Reflectance spectra of some alteration minerals. (Wavelength in $\mu\text{m}$ ) ....	84
Figure 68: Reflectance spectra of some oxides, hydroxides and sulfides. (Wavelength in $\mu\text{m}$ ) ....	85
Figure 69: Spectral analysis of a hand specimen compared to the USGS mineral database. ....	86
Figure 70: Example of a material map as a result of spectral library matching. ....	87
Figure 71: Sample image spectrum and matched spectrum of the mineral alunite from the USGS Spectral Library (goodness of fit = 0.91). ....	87
Figure 72: Reflectance spectrum for the mineral gypsum (A) with several absorption features. Curve B shows the continuum for the spectrum and C the spectrum after removal of the continuum. ....	87
Figure 73: Portion of an AVIRIS scene with forest, bare and vegetated fields, and a river, shown with a color-infrared band combination (vegetation is red). Fraction images from linear unmixing are show gray-scale. ....	88
Figure 74: (Left) A simple example of linear unmixing a scene in its basic components.(Right): An example of partial unmixing; here only targeting the presence of alunite. ....	89
Figure 75: Schematic overview of the "hourglass" processing sequence. ....	89
Figure 76: Alteration minerals at Cuprite. ....	90
Figure 77: Reflectance spectra of alteration minerals in the Cuprite area (JPL spectral library in ENVI). ....	91
Figure 78a: HYPERION mineral mapping. ....	91
Figure 78b: AVIRIS mineral mapping. ....	92
Figure 79: HYPERION SWIR mineral map (left). HYPERION SWIR apparent reflectance spectra (middle) and spectral library reference reflectance spectra (right). ....	92
Figure 80: Typical reflectance spectrum characteristic to green plants. ....	94
Figure 81: Monitor (left), control unit (middle) and optical sensor head (right) of the CASI-2 sensor (ITRES Research Limited, Canada). ....	95
Figure 82: Location of the study area 'De Westhoek'. ....	96

---

---

---

---

---

Figure 83. Reduction of the hyperspectral variability by applying a NDVI based mask for selecting vegetation pixels only. Where a = the hyperspectral image; b = NDVI image; c = mask; d = masked hyperspectral image. ....	97
Figure 84: Part of the hyperspectral track above 'De Westhoek' nature reserve, indicating the different ROIs collected during field survey. ....	98
Figure 85: Plot of the eigenvalues obtained after MNF transform. The first 6 bands were used for SAM classification. ....	99
Figure 86: Classification result of 'De Westhoek' nature reserve, using 13 different ROIs (classes). ....	99
Figure 87: MICROTOPS II sun photometer and the sun target. ....	111

---

---

---

---

---

## List of Tables

Table 1:	Summary of Landsat missions and sensors. ....	22
Table 2:	MSS bands. ....	23
Table 3:	TM bands. ....	23
Table 4:	ETM+ bands. ....	23
Table 5:	Synoptic overview of the SPOT series of satellites. ....	24
Table 6:	Spectral bands and resolution of SPOT 5 instruments. ....	24
Table 7:	ASTER Instrument characteristics. ....	25
Table 8:	Specifications of the GER IRIS Mark V. ....	42
Table 9:	Advantages and disadvantages of solar and artificial illumination. ....	44
Table 10:	Location error (horizontal offsets from nadir) as a function of the scan angle and DEM elevation error. ....	52
Table 11.	Quality and processing flags supplied with level 2 SeaWiFS imagery. Each pixel of radiometric data is accompanied by a 24-bit pixel for which each bit is set to one or zero according to the corresponding flag. ....	61
Table 12:	Leaf pigments and their absorption maxima. ....	94
Table 13:	CASI-2 characteristics. ....	95
Table 14:	The added extensions and their corresponding image pre-processing steps. ....	96
Table 15:	ROIs used for classification. In total 9 different ROIs were selected from the field survey. The grass type ROIs were manually selected from the imagery on the basis of field knowledge. ....	98
Table 16:	Confusion matrix calculated with ENVI. The obtained overall accuracy using 13 classes was 77% with a Kappa coefficient of 0.75. ....	100
Table 17:	Regions of interest collected during field survey. ....	101

---

---

---

---

---

## Foreword

Hyperspectral imaging is an innovative remote sensing technique with potential in many scientific disciplines due to its high spectral and spatial resolution. Worldwide more than 80 airborne imaging spectrometers are operational on a commercial or scientific basis while data from several spaceborne imaging spectrometers are available for scientific use. During the last decade many hyperspectral data processing and analysis tools were developed by scientists and software companies. Due to the high data dimensionality inherent to hyperspectral images, processing and analysis of these images remain complex. There is a lack of widespread expertise in hyperspectral image processing and analysis to optimally exploit the hyperspectral images. To interpret the hyperspectral images knowledge of the sensor, data acquisition, processing, analysis and the physical processes under investigation is required.

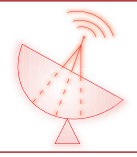
With HyperTeach (<http://hyperteach.vgt.vito.be>) we have the ambition to educate the hyperspectral user community. HyperTeach, a joint project of the Flemish Institute for Technological Research (VITO), the Management Unit of the North Sea Mathematical Models (MUMM), the Royal Museum for Central Africa (RMCA) and the Katholieke Universiteit Leuven (K.U.Leuven) funded by the Belgian Science Policy Office, aims at developing course material to theoretically and practically introduce researchers and decision-makers to the emerging field of hyperspectral remote sensing.

From 26-30 September 2005 the first HyperTeach training course is organised at the premises of VITO, K.U.Leuven and RMCA and instructed by teachers from MUMM, RMCA and VITO. There is an equal focus on theory and practical hands-on exercises. After 2 days of theoretical introduction and 1 day of self-study, the participants decide which of the 3 applications (water, geology or biodiversity) they prefer to follow during a 2-day parallel session with hands-on exercises. The target audience are decision-makers, early-stage researchers and potential users of airborne and spaceborne data who want to become acquainted with hyperspectral remote sensing. Depending on your interest, the pictograms (airborne, spaceborne, water, geology and biodiversity) will guide you through the course material.



## 1 Short introduction for busy decision-makers

With multispectral sensors, a limited number of broad spectral bands in the visible and infrared wavelength range are imaging the Earth's surface. Multispectral sensors have been quite successful to create maps of objects with discernible spectral differences in the multispectral's band set. However multispectral sensors undersample the reflected solar spectrum and their spectral resolution is insufficient to detect subtle spectral variations. In contrast, imaging spectrometers sample contiguously in the visible and infrared part of the reflected solar spectrum using hundreds of narrow spectral bands. Such data allows an experienced analyst to extract useful and more precise quantitative information about the Earth's surface.



This innovative remote sensing technique provides relevant input to numerous applications. Hyperspectral remote sensing is applied successfully for vegetation & forestry (ecosystem monitoring, vitality mapping), agriculture (estimation of yields, detection of stress), coastal zone management (beach erosion monitoring, detection of oil pollution), snow & ice (avalanche prediction), limnology (water quality), soil (organic carbon content, erosion), atmosphere (plume detection of volcanic activity), geology (mineral identification and prospecting), security and emergency response (leaching pollutants, land-slide prediction).



Currently about 80 airborne imaging spectrometers are available worldwide. Two next-generation imaging spectrometers (ARES and ARES) are under construction and will be available in 2005 and 2007 respectively. There are several spaceborne hyperspectral missions (HYPERION, CHRIS, ...) mainly used for atmosphere or ocean studies but their spatial resolution is often too coarse to study other environmental processes.



The raw airborne images suffer from spatial distortions due to the frequent motions of the aircraft caused by side winds and air turbulences. The motion of the aircraft is measured using a GPS and gyroscope. These external geometric distortions need to be compensated for in the post-processing with commercially available software using the GPS (eventually d-GPS differentially corrected GPS data using an in-situ base station GPS) and gyroscope data as input. For raw spaceborne images, georeferencing information is generally supplied. The stable and well-controlled flight of spaceborne systems simplifies greatly the georeferencing of data and the problems of spatial distortion as for airborne data are generally avoided.



Besides spatial distortions the airborne and spaceborne images are affected by the presence of the atmosphere between the Earth's surface and the airborne sensor. Software is available to eliminate the effect of the atmosphere using e.g. input from sun photometer measurements used to characterise the atmosphere. As you notice the use of in-situ equipment is indispensable for high quality hyperspectral remote sensing data.

Intrinsic to hyperspectral images is their huge information content. Once the hyperspectral images are corrected for geometric and atmospheric effects, the inherent dimensionality of the images often will be reduced to eliminate redundant information.

Finally, these georeferenced reflectance images can be used to identify objects at the Earth's surface. Depending on the application the images can be analysed or classified with several techniques (mapping, classification or abundance techniques).

Often the hyperspectral remote sensing data are combined with ancillary data (e.g. laser altimetry data, in-situ data) to deliver an information product to the decision-makers.

## 2 Imaging spectroscopy

Imaging spectroscopy is the acquisition of images in hundreds of registered, contiguous spectral bands such that for each picture element of an image it is possible to derive a complete reflectance spectrum (Goetz, 1992). Each picture element contains a unique reflectance spectrum which can be used for the identification of Earth's surface materials. The high spatial and spectral resolution reflectance images acquired by imaging spectrometers offer the opportunity to study the Earth's surface in great detail. The principle of imaging spectroscopy is illustrated in Figure 1.

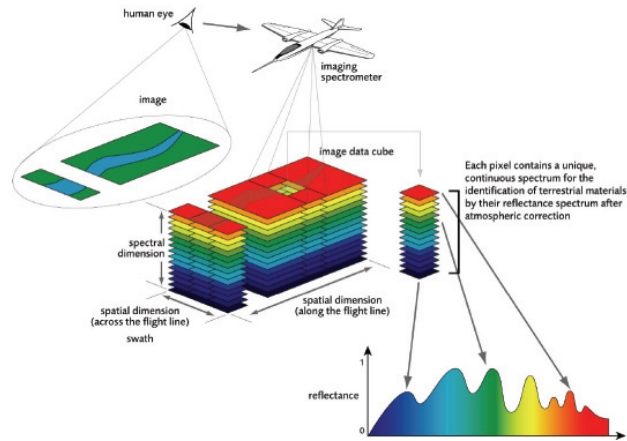


>> Figure 1: Principle of imaging spectroscopy.

The principle of airborne imaging spectroscopy is based on classical spectroscopy.

### 2.1 Physics of spectroscopy

#### 2.1.1 THE ELECTROMAGNETIC RADIATION EMR

To understand how remote sensing can be used to study the Earth, we need to understand what electromagnetic radiation is and how electromagnetic radiation interacts with matter (Drury, 1993; Atzberger). In this section the main concepts and definitions of spectroscopy will be briefly discussed. A more in depth discussion can be found in Section 1.2 of the Introduction to Satellite Remote sensing Module 1: Basic Concepts, K.U. Leuven (Willekens et al., 2001).

Electromagnetic radiation (EMR) propagates as a harmonic sinusoidal wave. EMR consists of oscillating electric and magnetic fields that are perpendicular to each other and perpendicular to the direction of travel. EMR can affect the electronic, vibrational and rotational properties of atoms or molecules.

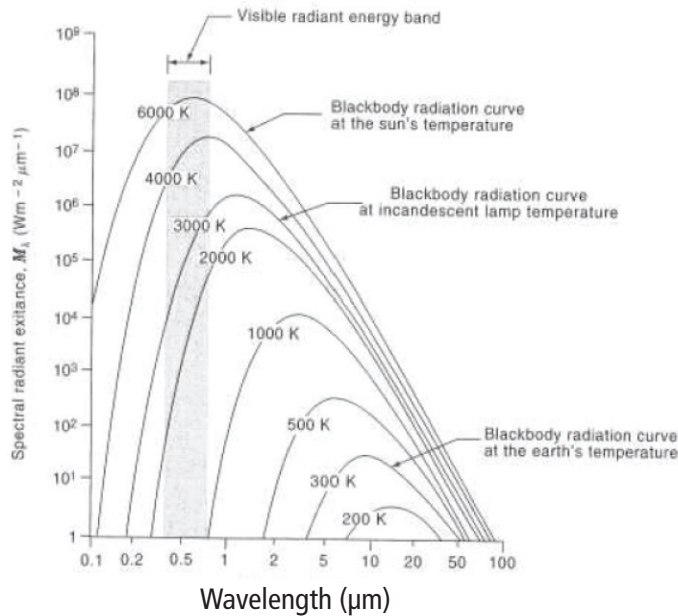
Electromagnetic radiation is thus a form of energy and is expressed in units of Joule (J). The electromagnetic radiation per unit of time and area or the radiant flux per unit area is called the radiant flux density and is expressed in  $\text{Wm}^{-2}$  (Watts per square meter). The radiant flux density incident on a surface is the irradiance (E) and emanating from a surface is the exitance (M). Because of the limited dimension and viewing angle of a detector, it only captures the electromagnetic radiation within a solid angle. The radiant flux density per unit solid angle is the radiance (R) and is expressed in units of  $\text{Wm}^{-2}\text{ster}^{-1}$  (Watts per square meter, per steradian, where steradian is the unit of solid angle).

Remote sensing instruments often have the capabilities of dispersing the light (a process which depends on the wavelength) in several detector elements. Therefore, monochromatic irradiance ( $E_\lambda$ ) or exitance ( $M_\lambda$ ) are expressed in units of  $\text{Wm}^{-2}\mu\text{m}^{-1}$  and spectral radiance ( $R_\lambda$ ) expressed in units of  $\text{Wm}^{-2}\text{ster}^{-1}\mu\text{m}^{-1}$ .

The prevalent source of energy excitation used to illuminate targets at the Earth's surface is the sun. According to Planck's law, the energy density of a black body is determined by its temperature (Figure 2). The radiant flux density of sunlight is determined by the photospheric temperature of the sun which peaks near 6000 K.

Incoming solar radiation is mainly confined to the spectral interval between 200 and 3400 nm (0.2 and 3.4 μm), with the maximum power input close to 480 nm (0.48 μm). As solar rays pass through the Earth's atmosphere, a fraction of the radiant energy is absorbed or backscattered, with the remainder transmitted.

**Planck's Law (1901)**



$$M(\lambda, T) = C_1 \frac{\lambda^{-5}}{e^{\frac{C_2}{\lambda T}} - 1} \tag{2.1}$$

λ in meters, T in K

with:

$$C_1 = 3.74 \times 10^{-16} \text{ W m}^2 \text{ (} 2\pi^5 h^6 c^2 \text{)}$$

$$h: \text{Planck's constant} = 6.626 \times 10^{-34} \text{ Js}$$

$$c \approx 3 \times 10^8 \text{ m/s}$$

$$C_2 = 1.44 \times 10^{-2} \text{ m K (} hc/k \text{)}$$

k: Boltzmann's constant

>> Figure 2: Energy density of a black body at different temperatures as a function of wavelength.

**2.1.2 INTERACTION OF RADIATION WITH MATTER**

When light interacts with the Earth's atmosphere or surface, light at certain wavelengths is preferentially absorbed while light at other wavelengths is transmitted or scattered (reflected). These three types of energy interaction are shown in Figure 3 and described below:

- (1) **transmission** - some radiation will penetrate into certain surfaces and will be transmitted through the surface;
- (2) **absorption** - some radiation will be absorbed through electron or molecular reactions within the medium encountered. A portion of the incorporated energy can then be re-emitted (as emittance), mainly at longer wavelengths
- (3) **reflection** - some radiation will be reflected (and scattered) from the target's surface at different angles. The angle of reflection depends on surface roughness as well as on the incidence angle.

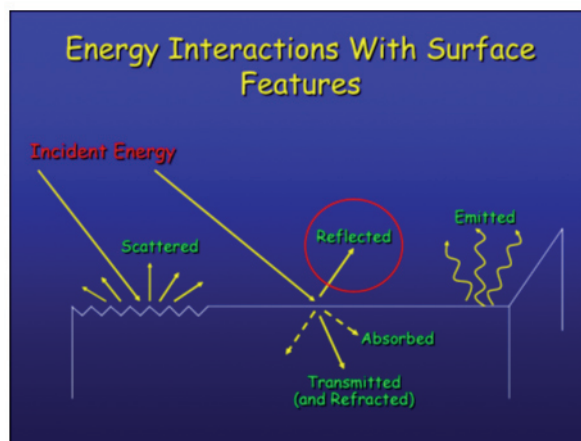


>> Figure 3: Energy interactions with matter.



Remote sensing systems in the VNIR (visible and near-infrared) and SWIR (short wave infrared) ranges are designed to monitor reflected radiation, whereas systems in the TIR (thermal infrared) measure emitted radiation.

The principle of energy conservation states that the incident radiant flux ( $E_i$ ) is totally distributed between reflected ( $E_r$ ), transmitted ( $E_t$ ) and absorbed ( $E_a$ ) energy.

$$E_i = E_t + E_a + E_r \tag{2.2}$$

Dividing this equation by the incident radiant flux  $E_i$  results in

$$E_i/E_i = E_t/E_i + E_a/E_i + E_r/E_i \tag{2.3}$$

$$1 = E_t/E_i + E_a/E_i + E_r/E_i \tag{2.4}$$

Transmittance ( $\tau$ ), absorptance ( $\alpha$ ), and reflectance ( $\rho$ ) are defined as the ratios of  $E_t/E_i$ ,  $E_a/E_i$  and  $E_r/E_i$  respectively.

$$1 = \tau + \alpha + \rho \tag{2.5}$$

Albedo is the ratio of the reflected radiance to the incident radiance over a broad wavelength range.

The nature of the material determines the degree in which light of different wavelengths is absorbed, transmitted or reflected. The part of the sunlight that is not absorbed is reflected and determines the "colour" of the material.

Most colours originate due to various absorption mechanisms. Where the striking light is absorbed at some wavelengths, it is reflected at others. Absorption is due to interactions between photons and electrons. Only unpaired electrons are bound loosely enough to interact with visible light photons.

By these effects, each material has its own spectral identity by which it can be identified (Figure 4). This so called "spectral signature" depicts the reflectance of a material as a function of the wavelength and is as characteristic for the material as a fingerprint is for a human being. The more, it is independent of the light source or the environment. At some wavelengths sand reflects more light than vegetation while at other wavelengths the opposite may be true.

In principle, through hyperspectral remote sensing various kinds of surface materials can be recognized and distinguished from each other by their spectral signature.

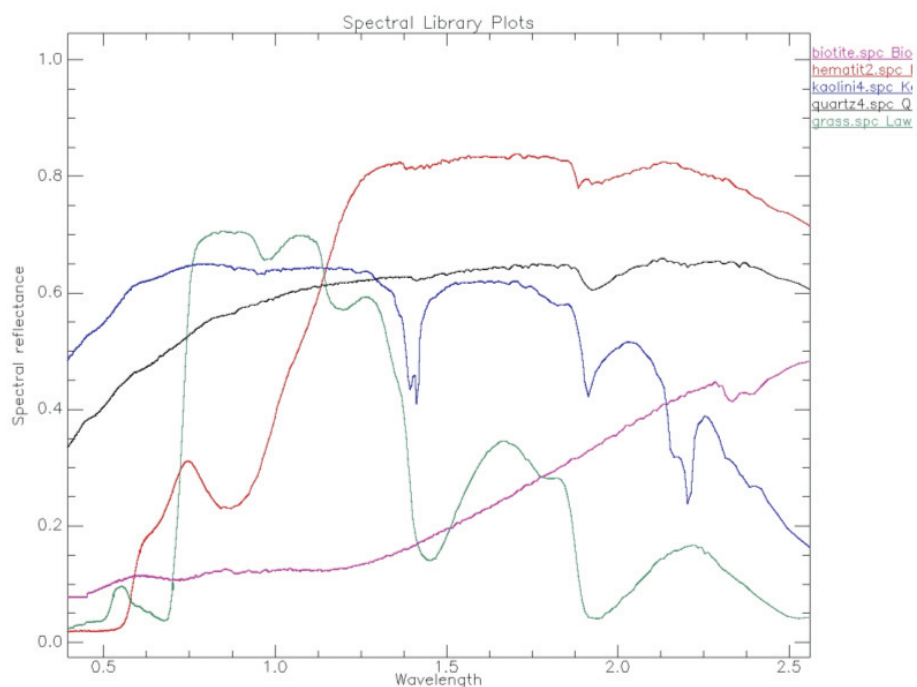
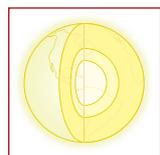
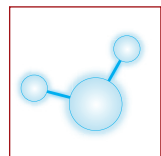
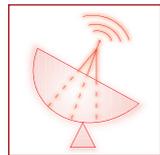


>> Figure 4: Reflectance spectra of minerals and vegetation.

## Specular and diffuse reflection

There are two extreme cases of scattering surfaces: the perfectly smooth surface (specular surface) and the perfectly rough surface (Lambertian surface). A surface is rough (smooth) if its texture is comparable or larger (smaller) than the wavelength of the incident radiation. A Lambertian surface reflects the incident radiation homogeneously in all directions, while a specular surface reflects the radiation in a single direction (Figure 5). In the latter case the angle of reflection equals the angle of incidence. Most surfaces are a combination of perfectly specular and perfectly Lambertian.

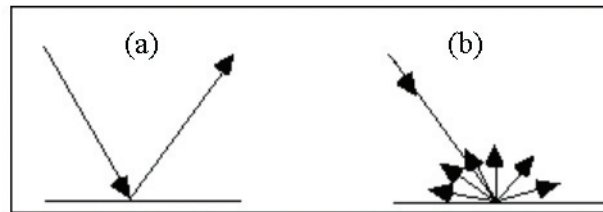


>> Figure 5: Specular (a) and diffuse (b) reflection.

## Hemispherical, bidirectional reflectance

Reflectance measurements can be hemispherical with hemispherical (directional) angles of incidence and reflection or bidirectional with directional angles of incidence and reflection. The Bidirectional Reflectance Distribution Function (BRDF) characterises the angular distribution (upper hemisphere) of the bidirectional reflection from a surface illuminated from a single direction. In practice BRDF is difficult to measure and therefore an approximation of the BRDF, the Bidirectional Reflectance Factor (BRF), is measured. BRF is defined as the ratio of the radiance reflected from a target to the radiance reflected from a loss-less Lambertian surface in the same direction measured under identical illumination conditions (Atzberger).

For further reading, see Introduction to Satellite Remote sensing Module 1: Basic Concepts, K.U. Leuven (Willekens et al., 2001).

### 2.1.3 FACTORS INFLUENCING SPECTRAL REFLECTANCE MEASUREMENTS

#### Radiance and Reflectance

The spectral reflectance of an object at the Earth's surface is a property that we would like to measure precisely and accurately using an airborne or spaceborne hyperspectral sensor.

The radiance spectrum in Figure 6 is the average of 25 image pixels spectra measured by the airborne AVIRIS sensor over a bright dry lake bed surface in the Cuprite, Nevada.

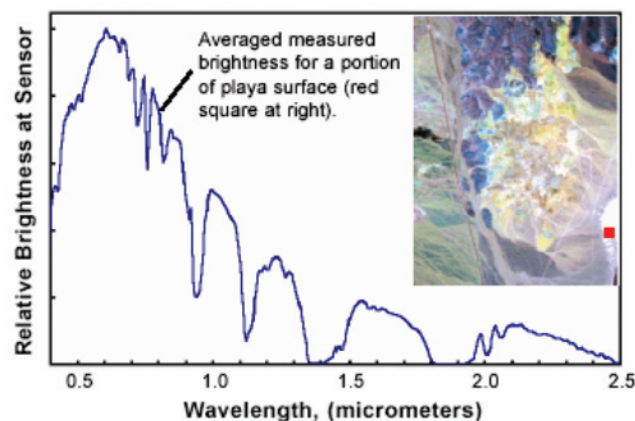


>> Figure 6: AVIRIS average spectral radiance curve on a bright target. (Source: <http://www.microimages.com/getstart/pdf/hyprspec.pdf>)

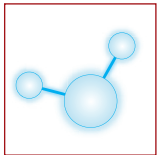


The input spectra have been adjusted for sensor effects using on-board calibration data, but no other transformations (like atmospheric corrections) have been applied.

This spectrum does not bear much resemblance to the reflectance spectra illustrated previously (Figure 4), measured in the lab. This is because the sensor measures spectral radiance at the sensor from an altitude of about 20 kilometres.



The similarity of the shape of the curve in Figure 6 to the sun irradiance in Figure 7 strongly suggests that the reflectance spectrum of the sample area is actually relatively flat and featureless.



The spectral reflectance of the surface materials is only one of the factors affecting the measured at-sensor radiance. In addition to surface reflectance, the spectral radiance measured by a remote sensor depends on the spectrum of the input solar radiation, interactions of the solar radiation during its downward and upward passage through the atmosphere, the geometry of illumination for individual areas on the ground and characteristics of the sensor system itself.



These additional factors not only affect our ability to retrieve accurate spectral reflectance values for objects at the Earth's surface, but also introduce additional variability which hampers comparisons between reflectances calculated from remotely sensed data and laboratory spectral libraries.



### Atmosphere

Radiation detected by airborne or spaceborne remote sensors passes through the atmosphere. Scattering and absorption in the atmosphere can have a profound effect on the radiation detected by the remote sensor. The effect of the atmosphere depends on the distance the radiation has to travel through the atmosphere, the atmospheric conditions and the wavelength of the radiation. More details on the atmospheric effects and how to correct for it can be found in Section 8 of the HyperTeach Theory Syllabus.

### Rayleigh/Mie scattering

Scattering is the diffusion of radiation caused by particles in the atmosphere. Rayleigh scattering occurs when radiation interacts with atmospheric molecules or particles that are much smaller in diameter than the wavelength of the radiation. The effect is inversely proportional to the fourth power of the wavelength.

Mie scattering occurs when the particles have a diameter which equals the wavelength of the radiation. Mie scattering intends to influence longer wavelengths compared to Rayleigh scattering.

### Absorption

Atmospheric gasses like water vapour, carbon dioxide and ozone absorb radiation at certain wavelengths in an efficient way. The wavelength region where the atmosphere is transmissive are referred to as atmospheric windows. Airborne or spaceborne remote sensing of the Earth's surface is only possible in the atmospheric windows.

For further details on atmospheric effects, the reader is redirected to Section 1.4.1 Atmospheric interaction of the basic RS course Introduction to Satellite Remote sensing Module 1: Basic Concepts, K.U. Leuven (Willekens et al., 2001) or Lillesand and Kiefer, 2004.

### Source illumination

Figure 7 shows a typical solar irradiance curve for the top of the Earth's atmosphere ( $I_e$ ). The incoming solar energy varies greatly with wavelength, peaking in the range of visible light. The spectrum of incident solar radiance at the time the radiance was acquired by the sensor must be known, assumed, or derived indirectly from other measurements in order to convert image sensor radiance values to targets' reflectance values.

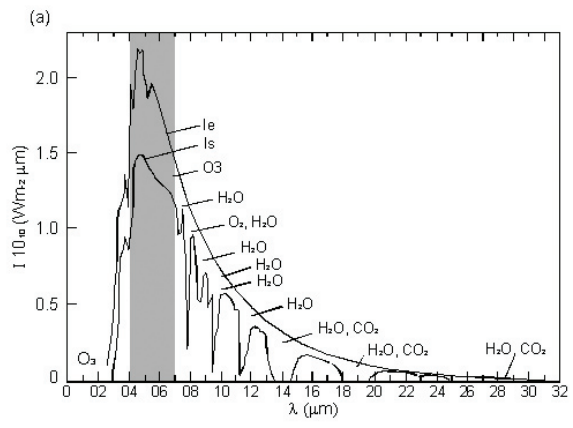
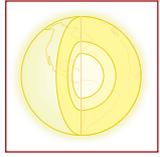
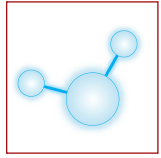
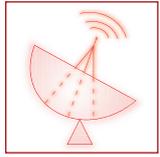
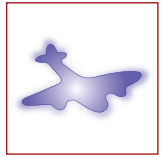
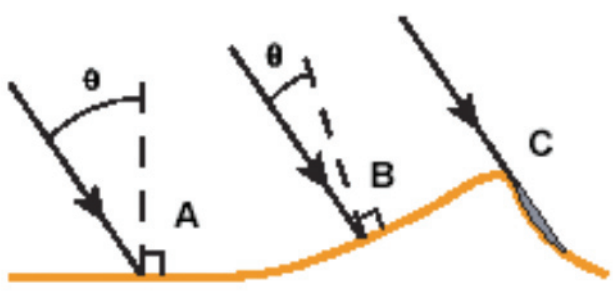


>> Figure 7: Solar irradiance spectra for the top of the atmosphere (top I<sub>e</sub>; also called extraterrestrial sun irradiance) and at ground level (bottom I<sub>s</sub>); the position of the visual wavelength range is indicated in gray.

**Illumination geometry**

The amount of energy reflected by an area on the ground depends on the amount of solar energy illuminating the area, which in turn depends on the angle of incidence: the angle between the path of the incoming energy and a line perpendicular to the ground surface. Specifically, the energy received at each angle  $E(\theta)$  varies as the cosine of the angle of incidence ( $\theta$ ):  $E(\theta) = E_o \times \cos \theta$ , where  $E_o$  is the amount of incoming energy. The energy received by any ground area therefore varies with time of day and season. If the terrain is not flat, the energy received also varies instantaneously across a scene because of differences in slope angle and direction.



**Illumination differences can arise from differing incidence angles ( $\theta$ ) as for A and B, or from shadowing (C).**

>> Figure 8: Incidence angles of direct sun illumination. (Source: <http://www.microimages.com/getstart/pdf/hyprspec.pdf>)

**Shadowing**

The amount of illumination received by an area can also be reduced by shadows. Shadows cast by topographic features or clouds can affect areas including many contiguous image cells.

Trees, crop rows, rock outcrops or other small objects can also cast shadows that are confined to an individual image cell. Both types of shadows have the effect of lowering the measured brightness across all wavelengths for the affected pixels.

**2.2 Imaging spectroradiometers**

The human eye has three sensors ( $\rho$  (Rho),  $\gamma$  (Gamma),  $\beta$  (Beta)) which are sensitive in three broad spectral bands centred around 580 nm, 540 nm and 450 nm respectively. Our eye can detect visual light from 400 nm (blue) to 700 nm (red). Light within this range will excite one or more of the three sensors. Our perception of colour is determined by the combination of the proportional excitation of the three sensors.

Imaging spectroradiometers have often more than hundred sensors which are sensitive in narrow spectral bands and can detect not only the visual light (400-700 nm) but also near-infrared (700-1000 nm) and short wave infrared radiation (1000-2500 nm).

Please be careful when interpreting sensor specifications. Often different definitions are used for band width, spectral resolution and sampling interval. The **spectral sampling interval** is the spacing between two sample points in the spectrum and is independent of the **spectral resolution** of a sensor. The spectral resolution is defined as the Full Width at Half Maximum (FWHM) of a sensor's response to a monochromatic source. The Full Width at Half Maximum (FWHM) of a sensor is defined as the full width at 50% of the peak height of the spectral response of the sensor to a monochromatic source. The FWHM is the definition of spectral resolution we use in the HyperTeach Syllabi. Figure 9 illustrates the difference between spectral sampling width and spectral resolution.

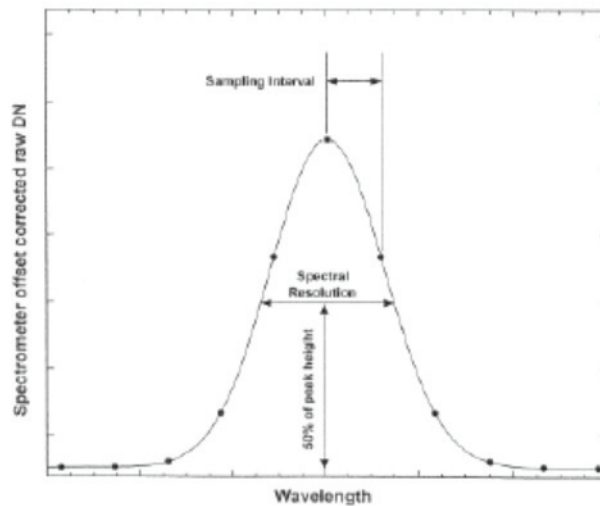


>> Figure 9: Illustration of spectral sampling interval and spectral resolution (Source: Technical Guide 3<sup>rd</sup> Ed. Section 3-1).

Figure 10 shows an example of the optical system of an imaging spectrometer.

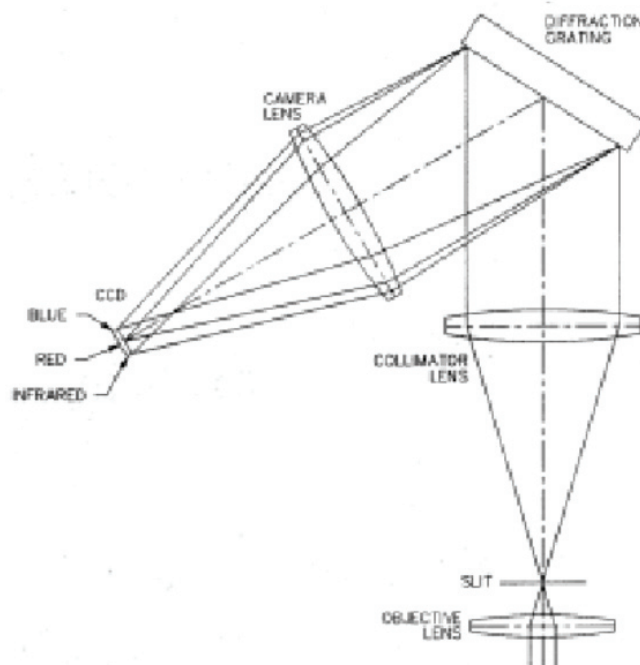


>> Figure 10: Schematic view of the optical system of the CASI-2 sensor. Source: ITRES, Research Ltd ([www.itres.com](http://www.itres.com)).

Incident rays are focussed in the imaging plane of the objective lens where they pass through the entrance slit. A collimator collimates the rays (makes parallel). The diffraction grating disperses the rays into different spectral components. A camera lens refocuses the rays onto the detector in the focal plane.

An imaging spectrometer often consists of a prism or grating to disperse the incoming light into different wavelengths and a 1- (**whiskbroom**) or 2-dimensional (**pushbroom**) sensor array. Figure 11 illustrates the whiskbroom and pushbroom principle (Nieke, 1997).

A whiskbroom sensor registers the reflected solar radiance of one ground cell in the different wavelengths and scans the landscape below from side to side using rotating mirrors. The rotating mirrors are used to redirect the light onto the sensor. The dwell time for each ground cell must be very short at a given IFOV (Instantaneous FOV) because each scan line consists of multiple ground cells which will be detected. Well known example of whiskbroom imager are AVHRR, Landsat and SeaWiFS, HyMAP.

A pushbroom sensor does not use scanning mirrors and registers the reflected solar radiance of the landscape below for the entire swath at once in the different wavelengths using a 2-dimensional array. The number of pixels is equal to the number of ground cells for a given swath. The motion of the aircraft or the satellite provides the scan in along-track-direction, thus, the inverse of the line frequency is equal to the pixel dwell time. If more bands are used, a more continuous reflectance spectrum will be registered. Pushbroom imaging spectrometers have many advantages. They are lighter, smaller and less complex because of less moving parts. They are characterized by a higher signal to noise ratio due to a longer dwell or exposing time (i.e. residence time over a given ground area). They also often have a better spectral and spatial resolution. A disadvantage is that their calibration is time and labour-consuming due to the large number of individual detector elements. Examples of pushbroom sensors are CASI, ROSIS, MERIS.

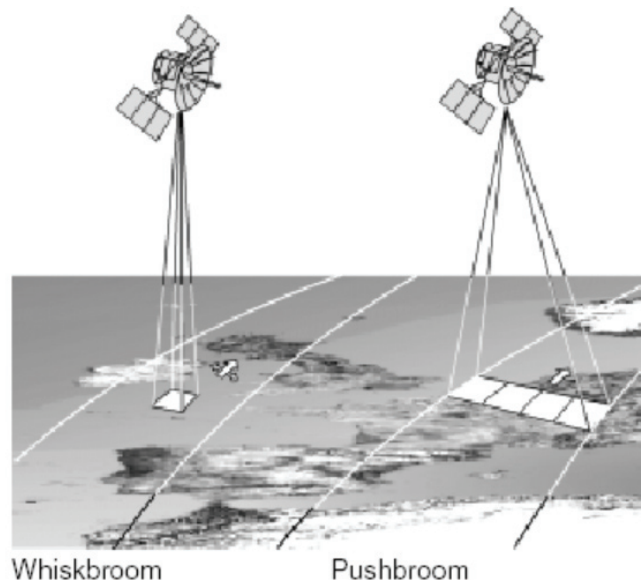


>> Figure 11: Whiskbroom (left) and pushbroom (right) principle (Nieke, 1997).

Once the photon (radiation) has reached the detector this gives rise to the creation of electron-hole pairs in the sensor material. During a certain integration time an electrode collects all the free electrons. An amplifier converts the electron charge into an analogue signal and amplifies (gain – intercept and offset – slope) the signal. An analogue-to-digital converter (ADC) converts the analogue signal to a discrete integer (Digital Number - DN). The ADC determines the dynamic range of the instrument (e.g. 12-bit ADC results in a dynamic range of 4096 Digital Numbers). Finally, the DN are stored on hard disk or tape drive.



## 2.2.1 AIRBORNE

### 2.2.1.1 Current

Imaging spectroradiometers acquire images in hundreds of calibrated, contiguous spectral bands, such that for each picture element it is possible to derive a complete reflectance spectrum.



The first scanning imaging spectrometer was the Scanning Imaging Spectroradiometer (SIS) constructed in the early 1970s for NASA. The Airborne Imaging Spectrometer (AIS) developed by NASA was operational from 1983 onward. This imaging sensor with a field of view of 3.7 degrees acquired data in 32 pixels across track in 128 spectral bands in the 1200-2400 nm wavelength range. The AIS-2 sensor acquired images with 64 pixels across track in the 800-2400 nm wavelength range. Since 1987 NASA is operating the AVIRIS sensor (Airborne Visible/Infrared Imaging Spectrometer), the successor of the AIS sensors. The AVIRIS sensor acquires data in 224 contiguous spectral bands in the 400-2500 nm wavelength region with a spectral sampling interval of < 10 nm. The AVIRIS Field-of-View is 30 degrees. The AVIRIS sensor consists of scanning optics and four spectrometers to image a 614 pixel swath.



Nowadays, many instruments (approximately 80) are commercially available worldwide. Since 1989 ITRES Research Ltd. is operating the Compact Airborne Spectrographic Imager (CASI). This pushbroom sensor collects data in 288 spectral bands in the 400 – 870 nm wavelength range with a spectral resolution of 1.9 nm in 512 pixels across track. Recently, ITRES Research Ltd., developed three new sensor types: the CASI-550 which is a refined design of the original CASI product line, the CASI-1500 which has a superior spatial resolution (25 cm) and the SASI-640, a SWIR sensor. The Geophysical Environmental Research Corporation (GER) developed the GERIS, the Digital Airborne Imaging Spectrometer (DAIS) and the Environmental Protection Systems (EPS). The Hyperspectral Mapper (HyMAP) constructed by Integrated Spectronics is operated by HyVISTA. This whiskbroom instrument collects data in 126 spectral channels in the VNIR-SWIR wavelength region (400-2500 nm), MIR (3-5  $\mu\text{m}$ ) and TIR (8-10  $\mu\text{m}$ ). In the VNIR and SWIR the at-sensor radiance is dispersed onto four detector arrays. The HyMAP with a Field-of-View of 61.3 degrees acquires 512 pixels across track. The Airborne Imaging Spectrometer AISA is a pushbroom imaging sensor developed by SPECIM, Finland. In standard mode the data is acquired in 288 spectral bands. The spectral range is 400-970 nm with a spectral sampling interval of 1.63 nm. The band width is programmable from 1.63 nm to 9.8 nm. The sensors Field-of-View is 21 degrees across-track and 0.055 degrees along-track to image a 360 pixels swath. The Reflective Optics System Imaging Spectrometer (ROSIS) is a pushbroom imaging spectrometer developed by Dornier Satellite Systems, GKSS Research Centre and the German Aerospace Center. ROSIS acquired images in 32 or 84 spectral bands in the 430-850 nm wavelength range with a spectral resolution of 7.6 nm. The Field-of-View is 16 degrees to image a 500 pixel swath.

Currently two next-generation airborne imaging spectrometers are under construction: the Airborne Reflective Emissive Spectrometer (ARES) and the Airborne Prism EXperiment (APEX). The sensors will be available in 2005 and 2007 respectively.

For more information on the history of Imaging Spectrometry the reader is referred to Van der Meer et al., 2001.

### 2.2.1.2 Future

The APEX sensor is an airborne pushbroom imaging spectrometer under development by a Swiss-Belgian consortium on behalf of the European Space Agency (ESA). APEX is intended as a simulator and a calibration and validation device for future spaceborne imaging spectrometers. Furthermore, APEX is an advanced scientific instrument for the European remote sensing community, recording images in approximately 300 spectral bands in the wavelength range between 380 nm and 2500 nm. The APEX sensor acquires images of 1000 pixels across track with a Field-of-View of 28 degrees. The spectral sampling interval is less than 10 nm. (In the 560-780 nm range it is less than 5 nm). The spectral resolution is smaller than 1.5 times the spectral sampling interval. Figure 12 shows the optical design of the APEX instrument. The reader can find more information on APEX on <http://www.apex-esa.org>.

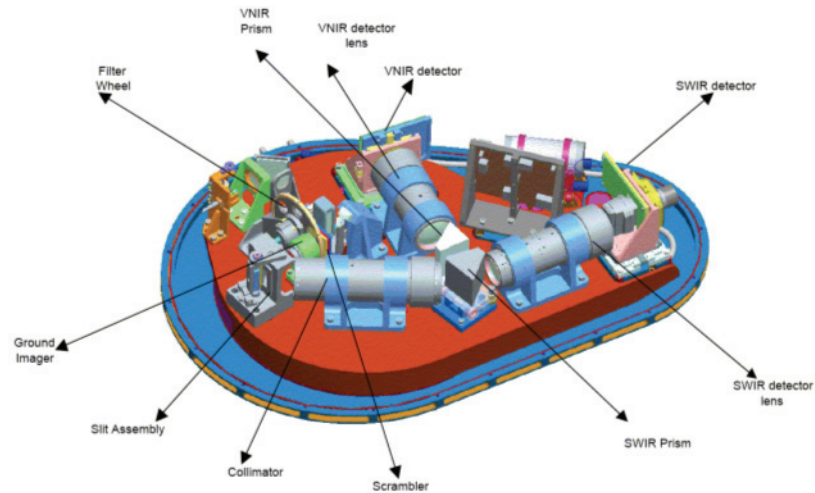


>> Figure 12: Schematic optical design of the APEX instrument.

The ARES instrument, a joint initiative of the Deutschen Zentrum für Luft- und Raumfahrt (DLR) and the GeoResearch Center (GFZ), will be manufactured by Integrated Spectronics, Sydney, Australia. ARES with a Field-of-View of 60-70 degrees will register images with 512-700 pixels per scan line. ARES, sensitive in the VNIR and SWIR wavelength region from 470-2410 nm and in the TIR region from 8.0-12 μm, will provide images containing information in 160 spectral bands. The targeted spectral resolution in the VNIR and SWIR will be 15 nm (12 nm for 2000-2410 nm wavelength region) while the targeted spectral resolution in the TIR will be 150 nm.

### 2.2.2 SPACEBORNE

In contrast to airborne remote sensing, where imaging spectrometers were becoming operational in the 1980s and ubiquitous in the 1990s, satellite remote sensing has until recently been dominated by systems based on multispectral radiometers with a much more limited number of bands.

The first satellite designed to monitor the Earth’s surface with a spatial resolution acceptable for geological applications was Landsat-1, launched by NASA in 1972. Initially referred to as ERTS-1, (Earth Resources Technology Satellite), Landsat was designed as an experiment to test the feasibility of collecting multi-spectral Earth observation data from an unmanned satellite platform. Since that time, this highly successful program has collected an abundance of data from around the world from several Landsat satellites.

Landsat’s success is due to several factors, including: a combination of sensors with spectral bands tailored to Earth observation; functional spatial resolution; and good areal coverage (swath width and revisit period). The long lifespan of the program has provided a voluminous archive of Earth resource data facilitating long term monitoring.

Satellite	Launch Date	Sensors	Status
Landsat 1	7-23-72	MSS	Expired 1-6-78
Landsat 2	1-22-75	MSS	Expired 2-5-82
Landsat 3	3-5-78	MSS	Expired 3-31-83
Landsat 4	7-16-82	MSS, TM	Sensors no longer operational since 7-87; expired 6-15-01.
Landsat 5	3-1-84	MSS, TM	Operational
Landsat 6	10-5-93	MSS, ETM	Lost at launch
Landsat 7	4-15-99	ETM+	Operational

>> Table 1: Summary of Landsat missions and sensors.

Each of these sensors collected data over a swath width of 185 km, with a full scene being defined as 185 km x 185 km.

**The Landsat Multi Spectral Scanner MSS**

The MSS sensed the electromagnetic radiation from the Earth’s surface in four spectral bands. Each band has a spatial resolution of approximately 60 x 80 metres and a radiometric resolution of 6 bits, or 64 digital numbers (DN) (6 bits variable offers  $2^6 = 64$  DN, compared to one byte = 8 bits, which gives  $2^8 = 256$  values).

Landsat 1-3 Band	Landsat 4-5 Band	Micrometers	Resolution
4	1	0.5 - 0.6	80 m
5	2	0.6 - 0.7	80 m
6	3	0.7 - 0.8	80 m
7	4	0.8 - 1.1	80 m
8	-	10.41 - 12.6	237 m

>> Table 2: MSS bands.

Routine collection of MSS data ceased in 1992, as the use of TM data, starting on Landsat 4, superseded the MSS.

**The Landsat Thematic Mapper TM and ETM+**

The TM sensor provides several improvements over the MSS sensor. It is characterised by higher spatial and radiometric resolution. TM has a resolution of 28.5 m for all bands, except for the thermal infrared band 120 m. All channels are recorded over a range of 256 digital numbers (8 bits).

Band	Micrometers	Resolution
1	0.45 - 0.53	30 m
2	0.52 - 0.60	30 m
3	0.63 - 0.69	30 m
4	0.76 - 0.90	30 m
5	1.55 - 1.75	30 m
6	10.40 - 12.50	120 m
7	2.08 - 2.35	30 m

>> Table 3: TM bands.

The earth observing instrument on Landsat 7, the Enhanced Thematic Mapper Plus (ETM+), replicates the capabilities of the highly successful Thematic Mapper instruments on Landsats 4 and 5. The ETM+ also includes new features:

a panchromatic band with 14.5 m spatial resolution, on board, full aperture, 5% absolute radiometric calibration and a thermal IR channel with 60 m spatial resolution.

Band	Micrometers	Resolution
1	0.45 to 0.515	30 m
2	0.525 to 0.605	30 m
3	0.63 to 0.690	30 m
4	0.75 to 0.90	30 m
5	1.55 to 1.75	30 m
6	10.40 to 12.5	60 m
7	2.09 to 2.35	30 m
Pan	0.52 to 0.90	15 m

>> Table 4: ETM+ bands.

Data from both the ETM+, TM and MSS sensors are used for a wide variety of applications, including resource management, mapping, environmental monitoring, and change detection (e.g. monitoring forest clear cutting).

More info on Landsat: <http://landsat.usgs.gov>.

## Système Probatoire pour l'Observation de la Terre: SPOT

SPOT is a series of Earth observation imaging satellites designed and launched by CNES (Centre National d'Études Spatiales) of France, with support from Sweden and Belgium. SPOT-1 was launched in 1986, with successors following every three or four years. All satellites are in sun-synchronous, near-polar orbits at altitudes around 830 km above the Earth, which results in an orbit cycle of 26 days. They have equator crossing times around 10:30 AM local solar time. SPOT was designed to be a commercial provider of Earth observation data, and was the first satellite to use along-track, or pushbroom scanning technology.

<b>Initiator</b>	CNES
<b>Origin</b>	studies for an Earth observation system carried out by CNES in the 1970s
<b>Status</b>	Currently operational
<b>Participants</b>	CNES, Belgian Science Policy Office, SNSB (Swedish National Space Board)
<b>Goals</b>	Help to improve knowledge and management of our planet
<b>Objectives</b>	Explore Earth's resources; detect and forecast phenomena involving climatology and oceanography; monitor human activities and natural phenomena
<b>Principal missions</b>	SPOT 1 – 1986 SPOT 2 – 1990 SPOT 3 – 1993/1996 SPOT 4 – 1998 SPOT 5 – 2002

>> Table 5: Synoptic overview of the SPOT series of satellites.

The viewing angle of the sensors can be adjusted to look to either side of the satellite's vertical (nadir) track, allowing off-nadir viewing which increases the satellite's revisit capability. This ability to point the sensors up to 27° from nadir, allows SPOT to view within a 950 km swath and to revisit any location several times per week. The off-nadir viewing also provides the capability of acquiring imagery for stereoscopic coverage. By recording the same area from two different angles, the imagery can be viewed and analyzed as a three dimensional model, a technique of tremendous value for terrain interpretation, mapping, and visual terrain simulations.

A single SPOT scene covers a geographical area of 60 x 60 km. Two alternative modes of imaging are possible :

- Panchromatic, black and white, with a ground resolution of 10 m.
- Multispectral, colour, with 20 m ground resolution acquired simultaneously in 3 bands : green, red and near-infrared.

Many operational applications in a variety of domains ranging from Earth sciences to economic planning and decision making take benefits of SPOT data : vegetation, agriculture, forestry, soils, geology, erosion, oil and mineral exploration, water resources, urban and rural planning, civil engineering, development projects or environmental monitoring.

### SPOT5

The SPOT5 satellite is composed of two new HRG (High Resolution Geometric) viewing instruments derived from SPOT4 HRVIR (High Resolution Visible and InfraRed) instruments which have a better resolution : 2.5 to 5 meters in panchromatic mode and 10 meters in multispectral mode.

Spectral band	HRG	HRV
PA 0.49 - 0.69 $\mu\text{m}$	2.5 m or 5 m	10 m
B0 0.43 - 0.47 $\mu\text{m}$	-	-
B1 0.49 - 0.61 $\mu\text{m}$	10 m	-
B2 0.61 - 0.68 $\mu\text{m}$	10 m	-
B3 0.78 - 0.89 $\mu\text{m}$	10 m	-
SWIR 1.58 – 1.75 $\mu\text{m}$	20 m	-
Swath	60 km	120 km

>> Table 6: Spectral bands and resolution of SPOT 5 instruments.

More info on SPOT: [http://www.spotimage.fr/html/\\_\\_.php](http://www.spotimage.fr/html/__.php).



**Indian Remote Sensing satellite series IRS**

The Indian Remote Sensing (IRS) satellite series, combines features from both the Landsat MSS/TM sensors and the SPOT HRV sensor.

It was commissioned with the launch of IRS-1A in March 1988 and at present there were four satellites which produced data that can be used in geology: IRS-1B launched in August 1991, IRS-1C launched in December 1995 and IRS-1D launched on September 29, 1997. Others were built for agricultural (IRS-P6) and cartographical purposes (IRS-P5; with a Very High Resolution Panchromatic camera).

Data from IRS satellites are received and processed by the National Indian Remote Sensing Agency, Hyderabad and commercialised by ESA and other operators.

**Advanced Spaceborne Thermal Emission and Reflection Radiometer: ASTER**

ASTER is a cooperative effort between NASA and the Japanese Ministry of Economy Trade and Industry (METI). The ASTER instrument consists of three separate instrument subsystems, each operating in a separate spectral region: the Visible and Near-infrared (VNIR), the Shortwave Infrared (SWIR) and the Thermal Infrared (TIR).

The VNIR subsystem operates in three spectral bands in the visible and near-infrared wavelengths, with a ground resolution of 15 m. It consists of two telescopes: one nadir-looking (3 bands) and one backward-looking (1 band). The backward-looking telescope provides a second view of the target area in Band 3, used for stereo observations.

The SWIR subsystem operates in six spectral bands in the NIR wavelength region through a single, nadir-pointing telescope that provides 30 m resolution.

The TIR subsystem operates in five bands in the thermal infrared region using a single, fixed-position, nadir-looking telescope with a resolution of 90 m.

Characteristic	VNIR	SWIR	TIR
Spectral Range	Band 1: 0.52 - 0.60 $\mu\text{m}$ , Nadir looking	Band 4: 1.600 - 1.700 $\mu\text{m}$	Band 10: 8.125 - 8.475 $\mu\text{m}$
	Band 2: 0.63 - 0.69 $\mu\text{m}$ , Nadir looking	Band 5: 2.145 - 2.185 $\mu\text{m}$	Band 11: 8.475 - 8.825 $\mu\text{m}$
	Band 3: 0.76 - 0.86 $\mu\text{m}$ , Nadir looking	Band 6: 2.185 - 2.225 $\mu\text{m}$	Band 12: 8.925 - 9.275 $\mu\text{m}$
	Band 3: 0.76 - 0.86 $\mu\text{m}$ , Backward looking	Band 7: 2.235 - 2.285 $\mu\text{m}$	Band 13: 10.25 - 10.95 $\mu\text{m}$
		Band 8: 2.295 - 2.365 $\mu\text{m}$	Band 14: 10.95 - 11.65 $\mu\text{m}$
		Band 9: 2.360 - 2.430 $\mu\text{m}$	
Ground Resolution	15 m	30 m	90 m
Swath Width (km)	60	60	60
Detector Type	Si	PtSi-Si	HgCdTe
Quantization (bits)	8	8	12

>> Table 7: ASTER Instrument characteristics.

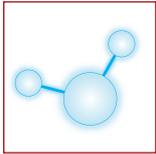
The performances of the ASTER channels make it the best spaceborne tool for geology up to now:

- good spatial resolution in the VNIR range (15 m)
- stereographic capabilities
- 6 spectral bands in the SWIR range, allowing the identification of carbonates and good discrimination between alteration mineral, including clays
- 5 bands in the TIR range allowing a mapping of the SiO<sub>2</sub> content.

More info: <http://www.science.aster.ersdac.or.jp/en/index.html>

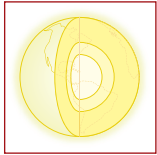


In the coming years improvements in the data transfer rate for satellite-ground transmission and in the capacity of mass data storage facilities needed for global satellite missions will facilitate the use of spaceborne imaging spectrometers with much finer spectral resolution, thus providing more information to improve the detection and discrimination of both land and water features.



### **HYPERION**

The HYPERION instrument on board of NASA's EO1 satellite provides a high resolution hyperspectral imager capable of resolving 220 spectral bands (from 0.4 to 2.5  $\mu\text{m}$ ) with a 30 meter spatial resolution. The instrument images a 7.5 km by 100 km land area per image and provides detailed spectral mapping across all 220 channels with high radiometric accuracy.



The focus of the HYPERION instrument is to provide high quality calibrated data that can support evaluation of hyperspectral technology for Earth observing missions. The HYPERION capabilities provide resolution of surface properties into hundreds of spectral bands versus the ten multispectral bands flown on traditional Landsat imaging missions. Through this large number of spectral bands, complex land eco-systems can be imaged and accurately classified.



Though the HYPERION instrument provides very high spectral resolution data, unfortunately a low signal to noise ratio makes it difficult to exploit for geologic applications in the SWIR range.

More info: [http://www.eoc.csiro.au/hswwww/EOC\\_data.htm](http://www.eoc.csiro.au/hswwww/EOC_data.htm).

### **CHRIS-PROBA**

The CHRIS sensor onboard the experimental PROBA satellite is, along with HYPERION, one of the first imaging spectrometers in space suitable for aquatic applications (Van Mol and Ruddick, 2004). CHRIS provides 63 spectral bands of data for an image of about 14 km square and at five different look angles (2 forward-pointing, one at nadir and two backward-pointing). Although not intended as an operational mission and highly restricted in terms of data throughput (typically one site is imaged per day somewhere in the world) CHRIS-PROBA can be seen as a technology-proving mission, which is providing vital information for the design of future systems. The CHRIS-PROBA mission supports scientific investigations for aerosol, coastal and inland water and vegetation.

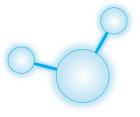
Further information on multispectral sensors suitable specifically for aquatic applications can be found in Section 4.1.1.

More info: <http://earth.esa.int/missions/thirdpartymission/proba.html>.



### 3 Flight planning

Careful campaign planning is one of the most important keys towards a successful mission. Airborne missions with complex sensors such as imaging spectrometers require a lot of preparation and are dealing with a lot of trade-off's and uncertainties. A first step within this process is a clear definition of the mission goals and data requirements. Planning a campaign is a process in which one has to find a compromise between data/scientific requirements on the one hand and operational and logistic requirements and constraints on the other hand. Changing one parameter can have a significant impact and sometimes requires a complete campaign redesign.



#### 3.1 The mission area

The mission definition starts with a clear delineation of the area one wants to cover. Delineate the zone, preferably by a polygon, and fix it by defining the coordinates of the corner points (preferably WGS 84). An important consideration one must make as soon as possible is the location of the area with regard to Air Traffic Control, the location of airfield and military training areas around. This can have important consequences on the planning (flight height, timing,...) and in the worst case make it almost impossible to acquire data in the target zone.

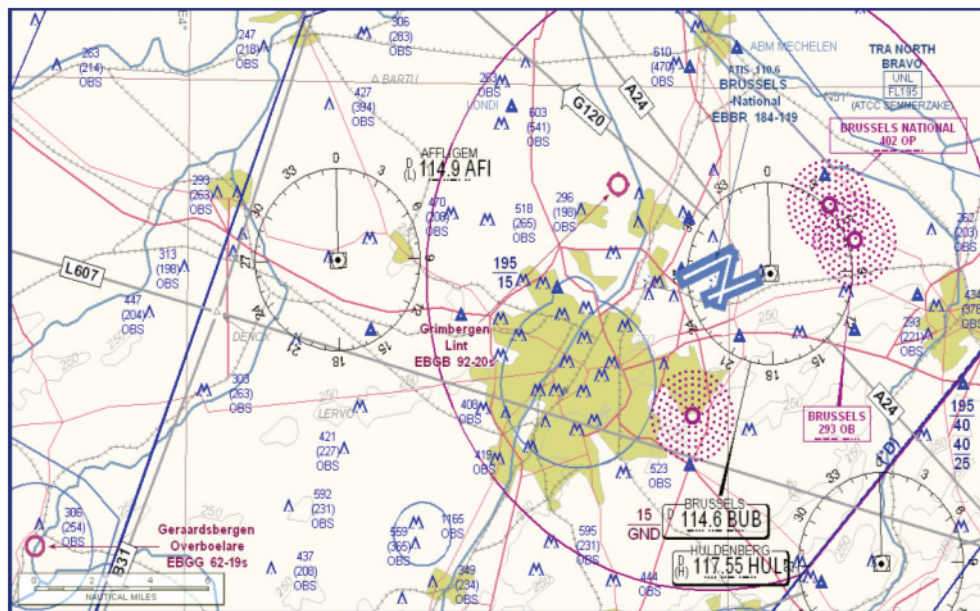


>> Figure 13: Aeronautical chart of Brussels National Airport and surroundings..

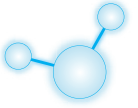
An other important issue in hyperspectral remote sensing campaign planning is the availability of reference targets within the mission area. Those reference targets can be used for radiometric calibration correction of the sensor and later on for atmospheric correction checks.

If no sufficiently large (rule of thumb is minimum 5x5 pixels), homogeneous, near-Lambertian and featureless reference targets (e.g. asphalt, water bodies, ...) are available within the mission area, artificial black and white reference targets can be used.

#### 3.2 Timing and illumination geometry

Airborne imaging spectroscopy, as a passive remote sensing technique, requires some minimal requirements with regard to illumination conditions. The optimal time for hyperspectral data acquisition is local solar noon +/- 2 hours because of the best illumination conditions. Around summer solstice a time window of solar noon +/- 3 hours at our latitude (52°) still guarantees, acceptable illumination conditions.

As the above statements are especially true for flying conditions during late spring and early summer, a minimum solar elevation angle of 30-35° can be put forward as essential for any airborne hyperspectral data acquisition. Keep in mind that times in sun elevation and aviation tables are often expressed in Greenwich Mean Time GMT instead of local time (LT).



Flight line orientation is mainly a function of illumination geometry. To obtain a homogeneous image illumination and to minimize bidirectional reflectance (BRDF) effects, flight lines have to be oriented into the solar plane, which is the vertical plane that contains the sun, ground target, and sensor.

The phenomenon of **bidirectional reflectance**, is the variation in reflectance depending on the location of the sensor in relation to the ground target and sun position (Asner et al., 1998). The BRDF appears mainly within the solar plane and the strongest reflection appears towards the sun (backscatter) whereas lowest reflection appears in the opposite direction (forward scatter). This is illustrated in Figure 14.

BRDF is caused by the anisotropic properties of the earth surface (vegetation, soil, ...) and depends on wavelength. The effect depends on the structural and optical properties of the surface, such as shadow-casting, multiple scattering, mutual shadowing, transmission, reflection, absorption and emission by surface elements, facet orientation distribution and facet density.

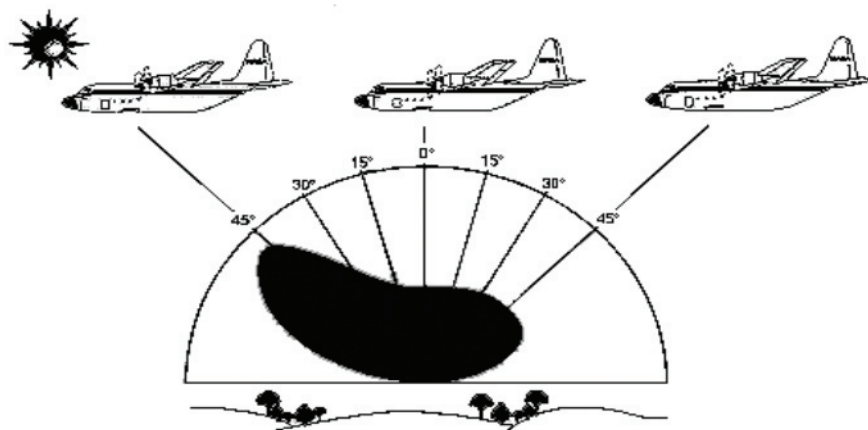


>> Figure 14: Aircraft flying within the solar plane. Hence the stronger reflection appears towards the sun and lowest reflection in the opposite direction (Ranson et al., 1994).

Figure 14 clearly illustrates that flying perpendicular to the solar plane (e.g. E→W, W→E), especially with sensors with a large FOV, will cause anisotropic illumination of the image and has to be avoided.

Ideally the flight lines are always oriented within the solar plane with the sun behind the plane. However, in practice this is not always feasible and flight lines are often oriented in N-S direction. For nadir looking sensors, flying N→S or S→N doesn't make any difference.

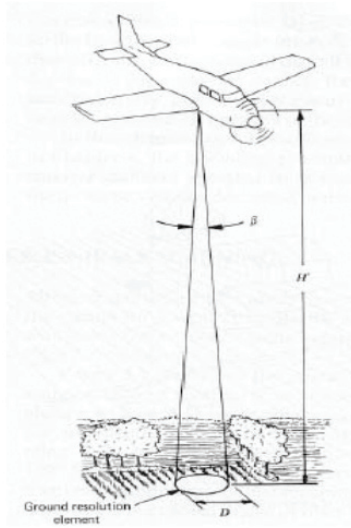
### 3.3 Spectral and spatial resolution and sensor choice

Defining the spectral and spatial resolution of a mission is not always as easy as it looks at first sight. Ideally, one would prefer a maximum number of spectral bands combined with a minimal pixel size. However this choice depends on a number of factors.

The main factor influencing the spectral and spatial resolution is the choice of the sensor. A system with a large Instantaneous Field Of View (IFOV), determined by the instrument's optical system and the size of its detectors, has a high signal-to-noise ratio. This results from the longer dwell time over which they can measure energy from the ground cell and therefore a much stronger signal can be recorded. This is translated into an improvement in the radiometric resolution (amount of energy required to increase a remotely sensed pixel value by one quantisation level). What is sacrificed for this high signal-to-noise ratio (radiometric resolution) is the spatial resolution. Similar, the signal-to-noise ratio can be increased by broadening the spectral bands. In the latter case the spectral resolution is sacrificed.

Depending on the sensor chosen one can have a fixed number of spectral bands recorded (e.g. HyMAP) or a number of programmable bands (e.g. CASI, AISA sensor). In the latter case the number of possible spectral bands determines the spatial resolution.

The spatial resolution of a whiskbroom scanner can be expressed as:



$$D = H' \cdot \beta \quad (3.1)$$

Where  $D$  is the diameter of the ground cell sensed by the sensor at any instant in time (spatial resolution),  $H'$  is the flying height above the terrain and  $\beta$  is the Instantaneous Field Of View (IFOV) of the system (expressed in radians).  $\beta$  is the cone angle within which energy is focused on the detector.

>> Figure 15: Relation between spatial resolution, height and IFOV of a whiskbroom sensor.

The spatial resolution of a pushbroom system depends on the optics (if applicable), the total FOV of the system, the along-track IFOV and the number of spatial pixels in the sensor.

As a consequence the spatial resolution of a system is directly related to the flying height above the target.

As illustrated in Figure 15 an additional constraint or trade-off can be the aircraft availability to execute the airborne mission. Most important factors are the operating altitude and the aircraft speed. However, in most cases the maximum operating altitude of an aircraft is not a restrictive factor, but due to air traffic constraints, the desired operating altitude and thus the intended spatial resolution can not always be achieved.

### 3.4 Other factors affecting campaign planning

As mentioned under Section 3.3 the choice of the aircraft may play an important role in the planning of a mission especially when multiple areas should be covered.

Important issues are:

- pressurized versus non-pressurized aircraft
- minimal airspeed
- aircraft endurance.

The observation hole used for remote sensing instruments with pressurized aircrafts, is sealed mostly with a glass plate. This plate can be made of different materials with differing optical properties. The presence of a glass plate may limit the sensor choice as the glass plate may affect the incoming light especially in the SWIR region and at longer wavelengths. The optical properties of any glass plate must be taken into account when retrieving the data.

The minimal flying speed of the aircraft is also an important factor when considering the spatial/spectral resolution. An aircraft surveying at lower speed gives rise to a smaller along-track pixel size. In some cases the minimal airspeed will be a limiting factor when choosing the spectral/spatial resolution for the scene. This especially is true when flying with a turboprop aircraft compared to a piston engine aircraft. Also air traffic control constraints or restrictions can be a limiting factor.

Other operational constraints such as coordination with tides, multiple overpasses and simultaneous in-situ measurements are strongly mission dependent and might be a severe constraint in operation.

Meteorological conditions are by far the most important but also the most unpredictable factor to account for. Hyperspectral remote sensing requires very good meteorological conditions (none or very few clouds (maximum 1/8)) and therefore the campaign planner should closely observe the weather forecast and consult multiple sources to obtain the most accurate view as possible on the weather evolution.

### 3.5 Auxiliary equipment and data

#### 3.5.1 AIRBORNE EQUIPMENT

An aircraft in operation is subjected to side winds and air turbulences. An Inertial Navigation System (INS) on-board registers the aircraft's movement.

##### 3.5.1.1 Inertial Navigation System

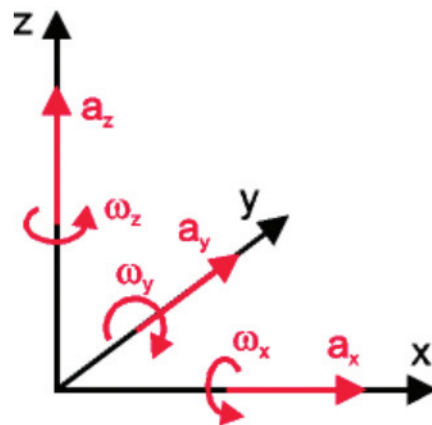
The fundamental function of an INS is to indicate the position, velocity, heading and direction of a vertical over a period of time (Broxmeyer, 1964).

The aircraft actual spatial behaviour or movement can be described with six parameters: three translational (x-, y-, z-acceleration) and three rotational components (x-, y-, z-angular velocity) (Figure 16).

To be able to define the movement of the aircraft, three acceleration sensors and three gyroscopes have to be put together on a platform in such a way, that they form an orthogonal system. Gyroscopes are instruments that sense angular rate. They are used to give the orientation of an object (angles of roll, pitch and yaw of an aircraft). Accelerometers sense a linear change in rate (acceleration) along a given axis.

The travelled distance and the angle over which the aircraft has actually rotated can be obtained by integration of the individual translational and rotational components.

Performing these calculations accurately and periodically enables the ideal system to trace its movement and to indicate its current position and heading.



$$s(t) = \iint a(t) dt^2 \quad (3.2)$$

$$\varphi(t) = \int \omega(t) dt \quad (3.3)$$

>> Figure 16: The six parameters of freedom. A aircraft's actual spatial behaviour or movement can be described with three translational and three rotational components. (Source: <http://www.electronic-engineering.ch/study/ins/ins.html>)

The main limitation of the system performance is given with the finite precision of the sensors. A continuous small error in acceleration will be integrated once to result in a large error in actual speed. Integrated during a second time it will result in a huge error in distance. Therefore very precise sensors and error correction mechanisms (feedback algorithms) are necessary to get an accurate inertial navigation platform. As an example, the g-vector method is a 'cheap' feedback algorithm. It does not require additional hardware, but simply assumes that the average direction of the z-acceleration vector points exactly rectangular down towards the earth surface and its average value is  $-9.81 \text{ m/s}^2$ . Another feedback method is the introduction of GPS position data fed into the INS, but this concept requires careful considerations about the update mechanism for not disturbing the entire system, especially in case you want to control devices and not simply measure their movements. Another consideration is the choose of the right coordinate system to be used. Different solutions exist - some of them with added redundancy to allow for improved precision.

We have chosen the representation based on 'Euler'-angles. It is defined by 3 axes: roll (alpha), pitch (beta) and direction (gamma). The translation to the components referring to the initial system proceeds as follows:

$$(x''', y''', z''') = (\alpha) \Rightarrow (x'', y'', z'') = (\beta) \Rightarrow (x', y', z') = (\gamma) \Rightarrow (x, y, z).$$

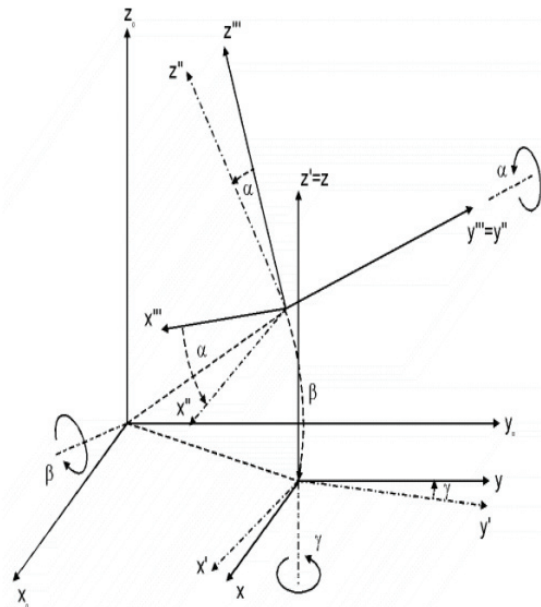
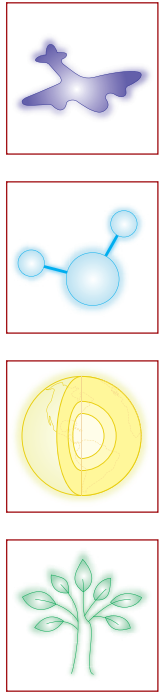


>> Figure 17: Representation of the aircraft's actual spatial situation ( $x'''$ ,  $y'''$ ,  $z'''$ ) referring to the initial system ( $x$ ,  $y$ ,  $z$ ) by using 'Euler'-angles.

$$\begin{pmatrix} \Delta x \\ \Delta y \\ \Delta z \end{pmatrix} = \begin{pmatrix} \cos(\gamma) * \cos(\alpha) & -\sin(\gamma) * \cos(\beta) & -\cos(\alpha) * \sin(\beta) * \sin(\gamma) \\ -\sin(\gamma) * \sin(\beta) * \sin(\alpha) & \cos(\gamma) * \cos(\beta) & +\sin(\alpha) * \cos(\gamma) \\ \sin(\beta) * \sin(\alpha) * \cos(\gamma) & \cos(\gamma) * \cos(\beta) & \cos(\gamma) * \sin(\beta) * \cos(\alpha) \\ -\cos(\alpha) * \sin(\gamma) & \cos(\gamma) * \cos(\beta) & +\sin(\gamma) * \sin(\alpha) \\ \cos(\beta) * \sin(\alpha) & -\sin(\beta) & \cos(\beta) * \cos(\alpha) \end{pmatrix} \begin{pmatrix} \Delta x''' \\ \Delta y''' \\ \Delta z''' \end{pmatrix} \quad (3.4)$$

Matrix representation to calculate the actual acceleration ( $dx$ ,  $dy$ ,  $dz$ ) referring to the initial system ( $x$ ,  $y$ ,  $z$ ) and using the mathematic transformation based on 'Euler'-angles.

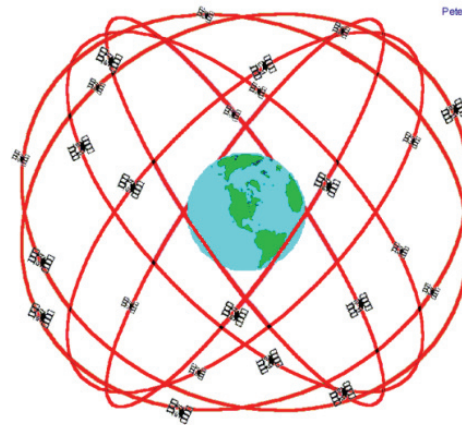
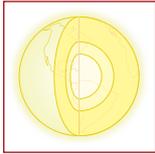
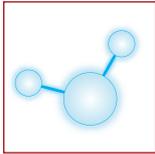
$$\begin{pmatrix} \Delta \alpha \\ \Delta \beta \\ \Delta \gamma \end{pmatrix} = \begin{pmatrix} 1 & \sin(\alpha) * \tan(\beta) & -\cos(\alpha) * \tan(\beta) \\ 0 & \cos(\alpha) & \sin(\alpha) \\ 0 & -\sin(\alpha) / \cos(\beta) & \cos(\alpha) / \cos(\beta) \end{pmatrix} \begin{pmatrix} \Delta \alpha''' \\ \Delta \beta''' \\ \Delta \gamma''' \end{pmatrix} \quad (3.5)$$

Matrix representation to calculate the actual angular velocity ( $d\alpha$ ,  $d\beta$ ,  $d\gamma$ ) referring to the initial system ( $x$ ,  $y$ ,  $z$ ) and using the mathematic transformation based on 'Euler'-angles.

Note that the sequence of transforming the actual data to the components of the initial system matters if the angles are large! Near the north pole you will not arrive at the same place if you first head for south and afterwards for west or first for west and then for south. Therefore keep the sampling frequency high enough in case you intend to allow fast angular movements.

### 3.5.1.2 Global Positioning System

The U.S. Global Positioning System (GPS), originally developed for defense purposes, includes a 24 satellites orbiting around the Earth in precisely known orbits, with subgroups of four satellites operation in six different orbit planes. These satellites revolve around the Earth every 12 hours at an altitude of 20,200 km. The nearly circular orbital planes of the satellites are inclined about 55° from the equator and space every 60° in longitude, permits that an observer at any point on Earth can receive the signal of at least four GPS satellites at any given time. (see Figure 18)

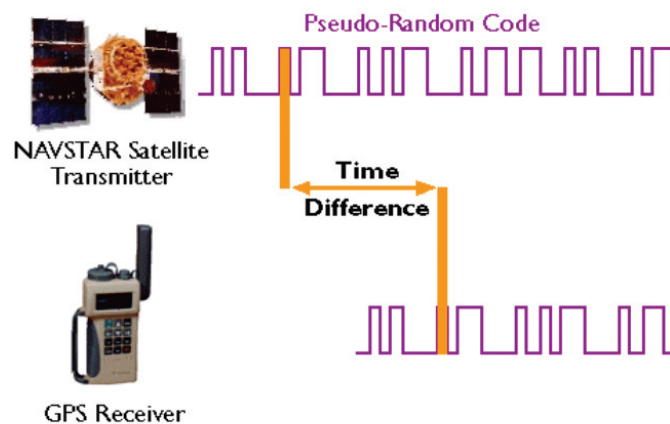


**GPS Nominal Constellation**  
 24 Satellites in 6 Orbital Planes  
 4 Satellites in each Plane  
 20,200 km Altitudes, 55 Degree Inclination

>> Figure 18: The GPS satellite constellation.

The means by which GPS signals are used to determine positions is called satellite ranging and simply involves measuring the time required for a signal transmitted by a given satellite to reach the receiver.

GPS receivers calculate distances to satellites as a function of the amount of time it takes for satellites' signals to reach the receiver. To make such a calculation, the receiver must be able to tell precisely when the signal was transmitted, and when it was received. Satellites are equipped with extremely accurate atomic clocks, so the timing of transmissions is always known. Receivers contain cheaper clocks, which tend to be sources of measurement error. The signals broadcast by satellites, called "pseudo-random codes", are accompanied by the almanac data that describes the shapes of satellite orbits.



$$\text{Distance} = \text{Speed of Light} \cdot \text{Time Difference}$$

(3.6)

>> Figure 19: GPS principle.

The GPS constellation is configured so that a minimum of four satellites is always "in view" everywhere on Earth. If only one satellite signal was available to a receiver, the set of possible positions would include the entire range sphere surrounding the satellite.

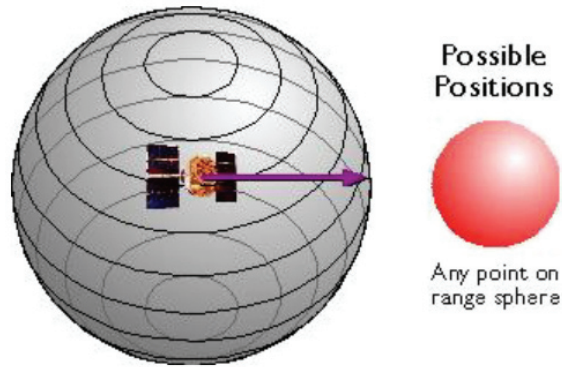
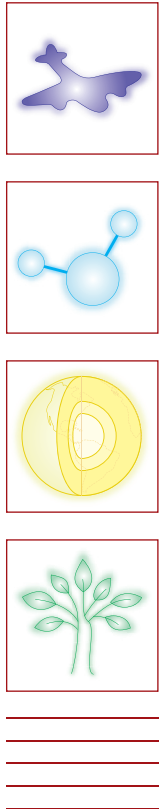


>> Figure 20: Set of possible positions of a GPS receiver relative to a single GPS satellite. After Trimble Navigation Limited.

If two satellites are available, a receiver can tell that its position is somewhere along a circle formed by the intersection of two spherical ranges.

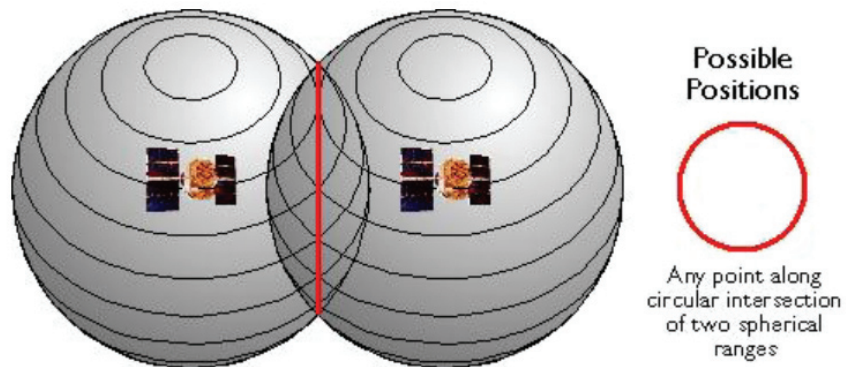


>> Figure 21: Set of possible positions of a GPS receiver relative to two GPS satellites. After Trimble Navigation Limited.

If distances from three satellites are known, the receiver's position must be one of two points at the intersection of three spherical ranges. GPS receivers are usually smart enough to choose the location nearest to the Earth's surface. At a minimum, three satellites are required for a two-dimensional (horizontal) fix. Four ranges are needed for a three-dimensional fix (horizontal and vertical)

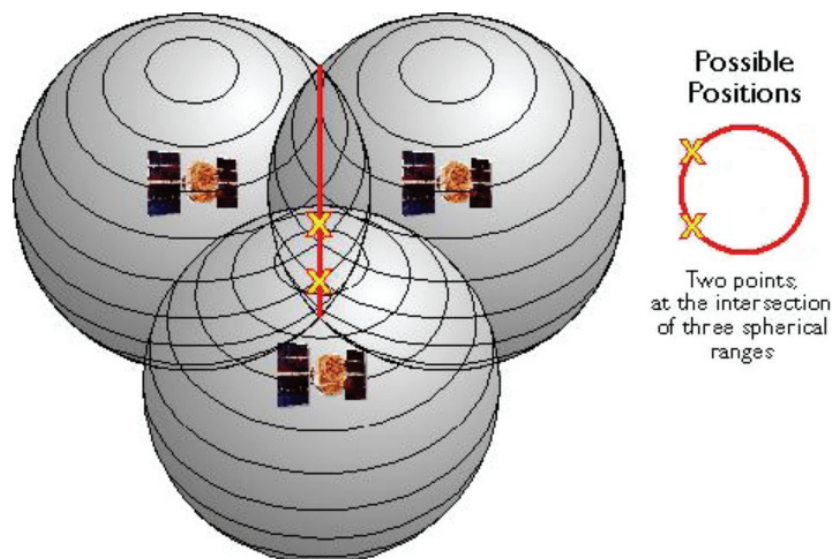
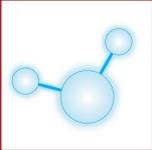


>> Figure 22: Set of possible positions of a GPS receiver relative to three GPS satellites. After Trimble Navigation Limited.



GPS measurements are subject to numerous sources of errors e.g. uncertainties in satellite orbits, errors due to atmospheric conditions, receiver errors, ... One can compensate for these errors using differential GPS (dGPS) methodology. In this approach, simultaneous measurements are made by a stationary "base station" receiver, located over a point of precisely known position, and a roving receiver (e.g. aircraft) moving from point to point. The positional errors measured at the base station are used to refine the position measured by the rover at the same instant in time. This can be done either by instantaneously broadcasting the base station corrections to the rovers (real time dGPS) or by bringing the data from the base and rover together. The latter is the most commonly used method in airborne remote sensing



The interested reader is referred to <http://www.colorado.edu/geography/gcraft/notes/gps/gps.html>, [https://www.e-education.psu.edu/courses/geog5121/L05\\_IIIB.html](https://www.e-education.psu.edu/courses/geog5121/L05_IIIB.html) and Lillesand and Kiefer, 2004.



## 4 Spaceborne data availability

Spaceborne data is generally obtained from the national and international space agencies operating the systems either directly, usually for research users, or via commercial distributors, for commercial use. An in-depth overview of existing systems was given in Section 2.2.2. The following sections describe the main characteristics looked for in these platforms and sensors by different users in function of their field of interest. Further information is given in the HyperTeach Hands-on Lessons.

The satellites currently used for aquatic remote sensing are almost entirely sun-synchronous polar-orbiters which acquire imagery for a specified time at a regular time each day or every few days. The rare exceptions are generally systems designed for other purposes but which can, in certain circumstances, be used for aquatic applications such as the pointable SPOT sensor which can be used for Total Suspended Matter detection in turbid waters and possible future geostationary sensors designed for meteorology. The main difference between spaceborne systems lies in the sensor characteristics rather than platform characteristics as described in the following section.

The satellites currently used for terrestrial remote sensing (in opposition to aquatic remote sensing) are those with a sun-synchronous polar-orbit that acquire imagery at a specified time of day (usually around 10.00 am) at a (repeat) interval of between a few days and a month.

### 4.1 Satellite sensor characteristics (spatial, spectral, etc.)

The usefulness of information that can be extracted from a spaceborne system is mainly a function of the sensor characteristics.

#### 4.1.1 WATER

The following section describes the main characteristics of sensors. Further information is given in Hyperteach Hands-on Lesson 4, where students will gather information on the most important sensors used for aquatic remote sensing.

- **Spectral bands:** the number, location and width of spectral bands is crucial in determining whether the sensor can be used for phytoplankton related applications such as chlorophyll *a* mapping. For the open ocean the International Ocean Colour Coordinating group (IOCCG, 1998) recommends that three reasonably narrow bands (e.g. 20 nm bandwidth or less) are needed at 443 nm, 490 nm and 560 nm plus at least two near-infrared bands (e.g. 750 nm and 865 nm) for atmospheric correction. This is, however, an absolute minimum and for coastal or inland waters much better spectral resolution is required as described in (Ruddick et al., 2005). For total suspended matter mapping much less resolution is required and even the two broad red and near-infrared bands of AVHRR can be used for highly reflective water (Stumpf and Pennock, 1989).
- **Spatial resolution:** most sensors used for aquatic applications have spatial resolution between 250 m and 1.2 km. This range covers the most popular ocean sensors, SeaWiFS, MODIS and MERIS, which provide global data, imaging any location of the Earth (except for very high latitudes) a few times per week. Higher spatial resolution is generally not yet available for sensors with the minimal spectral resolution needed for chlorophyll *a* mapping, though notable exceptions are HYPERION and the experimental CHRIS-PROBA mission described in Section 2.2.2.
- **Swath:** swath is the width of the ground area measured by an optical remote sensor and, along with the orbit, determines the frequency for which data will be available for any given site. The most popular ocean colour sensors, SeaWiFS, MODIS and MERIS, have swath of more than 1000km enabling frequent global coverage.
- **Calibration and validation:** the quality of data depends greatly on the calibration and validation activities organized by the satellite data providers. The most popular ocean colour sensors, SeaWiFS, MODIS and MERIS have extensive calibration and validation, which are documented on the respective web sites.

These characteristics are considered in detail in HyperTeach Hands-on Lesson 4.

## 4.1.2 LAND

### Spectral bands:

There where a limited amount of well chosen bands is enough to carry out water-related applications, for land surface applications there is a much wider variety of "objects" whose spectra will contribute to the overall signal captured by an airborne or spaceborne sensor. Generally, two main types of objects can be identified which will influence the choice of a suitable sensor. These are respectively vegetation (applications in ecology, agronomy, forestry, ...) and mineral matter (applications in geography, geology, pedology, ...).

For vegetation, properties are partly similar to those for water, at least for what the spectral property of chlorophyll is concerned. We refer to the section above for more detailed information.

As illustrated in Section 2, Figure 4, mineral matter has no single unequivocal absorption features. Different minerals will show a different spectrum, with overall shape and discriminant features possibly spread over a wide spectral range between the visible (VIS), near-infrared (NIR), short-wave infrared (SWIR) to the thermal infrared (TIR). The use of these discriminant features in spectral earth-sciences (geological) remote sensing is discussed more in detail in Part II of the HyperTeach Theory Syllabus.

This means that, ideally, for earth-sciences based applications, the complete spectrum between the VIS and SWIR and in the TIR should be recorded as detailed as possible. In practice, as shown in Section 2.2.2, sensors have been built that try to respond to this prerequisite; moreover, there is also a clear "technology driven" evolution. The oldest sensors (MSS 1, 2, 3) had only a limited number of well positioned bands (4) with a low spectral resolution (bandwidth), the recent hyperspectral sensors have more than 200 spectral bands with a much higher spectral resolution that allows to reconstruct a spectrum "almost" as good as measured in the lab.

### Spatial resolution:

For all existing sensors used in earth-sciences applications, there is a direct relationship between spatial and spectral resolution, that is controlled by the limitation of the present-day technology. As a rule of thumb, the higher the spatial resolution in a particular wavelength interval, the lower the spectral resolution over that interval. As such, the (very) high ground resolution (1 m) can until now only be achieved with panchromatic sensors which measure the entire VIS range in one channel (low spectral resolution). At the other end of the scale, the experimental HYPERION sensor has 220 channels in the VIS, NIR and SWIR range (high spectral resolution) for 30 m spatial resolution.

Except in the case of global or continental-scale applications, most sensors used for earth-science applications have resolutions between 1 m and 100 m. This range covers the most popular sensors described in Section 2.2.2. Higher spatial resolution is generally not yet available for the public domain, although it exists for the military.

### Swath:

The most popular earth-science sensors have a swath width of a few km to about 100 km. This has as a result that the repeat cycle of these sensors (the period between succeeding moments that the same area on the ground can be observed again) is usually in the order of several days (5 and 30). This has also as effect that a complete global dataset will only be available after every cycle and thus that these sensors are unsuited for monitoring (dynamic) global events.

### Calibration and validation:

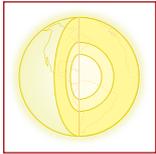
All platforms and sensors have on-board calibration systems. First level correction and validation of the acquired data is usually carried out at processing facilities of the satellite operator, or at a particular terrestrial receiving station which will distribute the data. We refer to the websites of the respective satellite operators for in-depth documentation.

### General considerations:

Although knowledge about the characteristics of the most used sensors in earth-sciences observation is important, even more important is the choice of the sensor(s) that will correspond the closest to the needs of

the investigation that will be carried out. There is no cookbook recipe which will identify that sensor, but a general set of rules can be applied.

1. **application definition:** what features and/or processes relate to the application? Is it possible to extract information about them from images from that particular sensor
2. **resolution and scale:** over what range of scales do the features and processes manifest themselves? In general, the finer the resolution the larger the scale is of representation. The maximum scale needed is often a guide to the minimum resolution size. If requirement involves a scale of 1:1 million, there is little point in using data from a satellite capable of providing 10 m or less spatial resolution.
3. **spectral coverage:** is hyperspectral, multispectral or single spectral (panchromatic) imagery required, and what regions of the spectrum are appropriate for the features being studied?



## 5 Field measurements

### 5.1 Planning

In-situ data like base station GPS data, spectroradiometer data of reference targets and sun photometer data, is necessary to correct the at-sensor radiance images to geocoded reflectance images with optimal accuracy.

It is evident for an accurate geocoding of the images that the base station GPS data to differentially correct the airborne GPS data should be collected during the time of the flight at a distance of maximum 30 km from the airborne GPS. For an accurate atmospheric correction of airborne and spaceborne images it is of utmost importance that sun photometer data, that allows to characterise the atmosphere at the location and time of the flight/overpass, are taken during and at the location of the airborne or spaceborne image acquisition. Notwithstanding reflectance data should be independent of the atmospheric conditions spectroradiometer data of reference targets located in the mission are preferentially taken during the flight/overpass because of changing conditions.

Furthermore, spectroradiometer data (in-situ or in the lab) is used to establish correlations between reflectance data and parameters (e.g. chlorophyll *a* content) determined from alternative measurement techniques and finally spectroradiometer data (in-situ or in the lab) is used to create spectral libraries. Those libraries are used for image classification training and validation purposes.

It is evident that a good communication between the campaign planner and the in-situ team is of utmost importance to guarantee a successful campaign.

### 5.2 Equipment

Since 2004 VITO is managing a pool of in-situ equipment consisting of field spectroradiometers (FieldSpec Pro FR, GER 1500), a sun photometer (Microtops II), a GPS base station (Leica SR530 and GPS receiver) to support the airborne imaging spectroscopy campaigns. The characteristics of the equipment pool instruments and other instruments are described here. The measurement procedure of the equipment pool instruments can be found in Annex Section 14.

#### 5.2.1 FIELD SPECTRORADIOMETERS (FIELD SPEC PRO FR, GER1500, GER IRIS MARK V, PIMA, OCEAN OPTICS, RAMSES)

Field spectroscopy is the quantitative measurement of the continuous radiance, reflectance or irradiance spectrum in the VNIR and/or SWIR wavelength range using portable instrumentation.

In general field spectroradiometers are used:

- to measure the reflectance spectrum of natural or artificial reference targets for calculation of radiometric calibration correction factors of the imaging sensors
- to measure the reflectance spectrum of natural or artificial reference targets to support the atmospheric correction process
- to measure down-welling solar irradiance to support the atmospheric correction process
- to measure the reflectance spectrum of natural or artificial targets to determine a correlation between reflectance and other parameters measured with alternative techniques
- to create spectral libraries of reflectance spectra to support the classification or validation process
- to perform feasibility studies.

To determine reflectance from radiance measurements a reflectance reference (Lambertian) material of well-known reflectance is used. Possible reference materials are Halon (powdered PolyTetraFluoroEthylene (PTFE)), Spectralon® (cintered PTFE), BaSO<sub>4</sub>, Fiberfrax, MgO, ceramics.

#### FieldSpec Pro FR (Analytical Spectral Devices)

VITO's FieldSpec Pro FR manufactured by Analytical Spectral Devices is a portable spectroradiometer measuring the absolute or relative light energy through a fiber optic bundle (of 1.5 m length) and can be used in the lab or in the field. Inside the instrument the light is projected onto a diffraction grating separating the different wavelength components of the light. The separated light is detected by the different detectors of the instrument.

Each detector converts incident photons into electrons. The photoelectric current for each detector is converted to a voltage and is digitized by a 16-bit Analogue to Digital (A/D) Converter. The digital data is transferred to the computer's memory.

The Visible/Near-infrared (VNIR) portion of the spectrum, the 350 - 1050 nanometre wavelength domain, is measured by a 512-channel silicon photodiode array with a minimum integration time (i.e. the time that the electrode collects electrons before a next measurement will start) of 100 ms. In practice the, integration time is set to 10 (indoor measurements) or 40 (outdoor measurements) times the min. integration, in order to filter out noise and to obtain a better signal to noise ratio (see Annex, Section 14.2.2). Each channel, which corresponds to an individual detector, is geometrically positioned to receive light within a narrow (1.4 nm) bandwidth. The VNIR spectrometer has a spectral resolution (FWHM of a single emission line) of approximately 3 nm at around 700 nm.

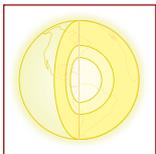
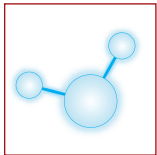
The Short-Wave Infrared (SWIR) portion of the spectrum is acquired with two scanning spectrometers. Rather than measuring all wavelengths simultaneously, these spectrometers measure the wavelengths sequentially. Each spectrometer consists of a concave holographic grating and a single thermo-electrically cooled indium gallium arsenide (InGaAs) detector. Unlike the VNIR, each SWIR spectrometer has only one detector, which is exposed to different wavelengths of light as the grating oscillates. The first spectrometer (SWIR1) measures light between about 900 and 1850 nm while the second (SWIR2) covers the region from about 1700 to 2500 nm. The sampling interval for each SWIR region is about 2 nm, and the spectral resolution varies between 10 nm and 12 nm, depending on the scan angle at that wavelength. The measured results are interpolated by the ASD software to produce readings at every 1 nm. The fiber optic cable has a full angle view of 25 degrees. Light may be collected with bare fiber optic (full angle 25 degrees), with fore optics (1, 8 and 18 degrees) or with a Remote Cosine Receptor to measure irradiance (i.e. hemispherical radiance). A picture of the FieldSpec Pro FR in operation is shown in

Figure 23. More information on the instrument specifications can be found in ASD Technical Guide (3<sup>rd</sup> Ed). The FieldSpec Pro FR measurement procedure is described in Annex, Section 14.2.2.



>> Figure 23: Picture of FieldSpec Pro FR (<http://www.asdi.com/>).

VITO's FieldSpec Pro FR can be combined with an integrating sphere with internal light source (e.g. Li-Cor 1800 12S). The Li-Cor 1800 12S (Figure 24) can be used to measure reflectance from or transmittance through a sample material. The purpose of using an integrating sphere is the collection of all the radiation that is reflected from or transmitted through the sample. The Li-Cor 1800 12 S is an external integrating sphere which means that the sample is external. An internal integrating sphere has a sample inside the sphere, often in the centre.



>> Figure 24: Picture of the Li-Cor 1800 12S Integrating Sphere.

Another type of instrument using an internal halogen bulb and which can be used in combination with the FieldSpec Pro FR is the High Intensity Contact Probe (Figure 25). The instrument is used for mineral, grain and granule applications.



>> Figure 25: Picture of High Intensity Contact Probe (<http://www.asdi.com/>).

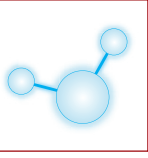
For plant samples a modified version is used. The Plant Probe uses a lower intensity bulb guaranteeing non-destructive data collection.

**GER1500 (GER - Geophysical and Environmental Research Corporation)**

VITO's GER1500 instrument (Figure 26) is a portable spectroradiometer measuring the absolute and relative light energy directly without fiber optic and can be used in the lab or in the field. Inside the instrument the light is separated and detected by a 512-channel silicon array. Light from the Visible/Near-infrared (VNIR) wavelength range, 350 - 1050 nanometre, is received by the 512 channels, i.e. individual detectors, within 1.5 nm bandwidth. The sensor has a spectral resolution of 3 nm. Incident photons are converted to electrons within the detector. The photoelectric current is converted to voltage and digitized by a 16-bit Analogue to Digital (A/D) Converter. Light is collected within a full angle of 8 degrees with a minimum integration time of 5 ms, which is smaller than the 100 ms min. integration time of the FieldSpec Pro FR.



>> Figure 26: Picture of GER1500 spectroradiometer.



### GER IRIS Mark V (GER - Geophysical and Environmental Research Corporation)

The GER Mark V Infra Red Intelligent Spectroradiometer (IRIS) is a self-contained, compact optical system for research and applications in both the laboratory and the field. It provides accurate spectral measurements from 350 to 2500 nm. The sensor head is portable, rugged and battery-operated. The system is controlled by a personal computer (generally a laptop), which also receives and stores the spectral data. The **SIGNATURE** software system developed by GER provides capabilities for data storage, retrieval and plotting.

Accurate spectra are obtained by comparing the spectrum of the target region with a standard of known spectral characteristics. The Mark V is a dual Field-Of-View instrument, allowing the simultaneous measurement of the target and the reference through the same lens. This feature saves data collection and processing time and ensures precise data in variable light conditions.

The optical system performs the scan and makes all required adjustments over the spectral range. The entire spectral range is covered in one continuous scan. As the wavelength is scanned, order-separating filters and detectors are changed automatically by the computer. Gain adjustments are also made automatically, allowing a wide range of light intensities to be accommodated. The grating angle and the positioning of the order-separating filters are each controlled by a stepping motor.

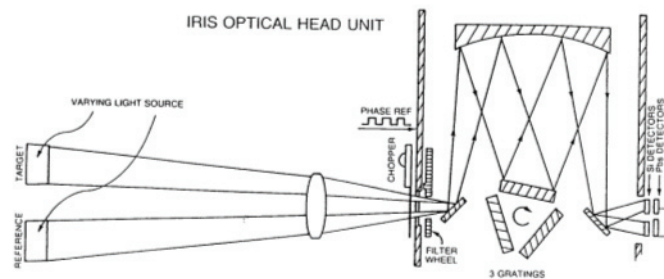


>> Figure 27: The optical system of the GER IRIS Mark V (GER users manual, 1995).

As shown on Figure 27, radiation from the reference and target enters through a single lens and is chopped at 230 Hz by a tuning fork. The radiation passes through an order-separating filter, which ensures that the grating will be illuminated by radiation in its primary spectral range. The radiation beams are collimated by a spherical mirror and illuminate a grating. Three gratings are used, each of which operates only in the primary spectral region. As the wavelength scan proceeds, the Mark V automatically positions the correct grating in the spectral path. The radiation then illuminates the thermoelectrically cooled detector elements. Two types of detectors are used: silicon diode for short wavelengths and PbS for longer wavelengths. The system automatically selects the correct detector for the spectral range being detected. Separate detectors are used to acquire the target and reference spectra.

Signals from the detectors are processed through phase sensitive electronics tuned to 230 Hz. The output signals are sampled and converted to 15 bit digital data. The channel data is processed and stored as radiometric data. The spectral scans are stored for later processing as individual spectra calibrated for radiance, or as ratio spectra calibrated for percent reflectance.

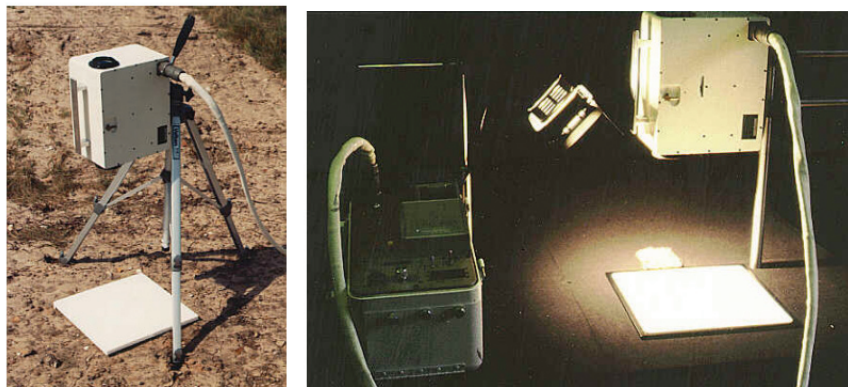


>> Figure 28: Deployment of the GER IRIS Mark V in the field (left) and in the lab (right).

Simple menu-driven programs control the setup, acquisition, and data manipulation functions. Various setup options are available such as integration time, spectral range to be scanned, file name and data display. When the data display option is chosen, the data comes on the computer screen within milliseconds of the time it is acquired.

Data in the computer memory can be processed immediately following the scan or can be called up later for analysis. The data files (typically about 16 kBytes in size) are written directly to the hard disk, allowing thousands of spectral scans to be stored.

<i>Optics</i>	
<b>Detectors</b>	Silicon Diode (300 nm to 1000 nm), PbS (1000 nm to 3000 nm)
<b>Spectral Bandwidth:</b>	2 nm in the 350 nm to 1.0 micron region, 4 nm in the 1.0 to 2.5 micron region.
<b>Spectral Range:</b>	350 nm to 2.5 microns.
<b>Design:</b>	125 mm focal length, off axis, Ebert monochromator.
<b>Effective Aperture:</b>	f/2.0.
<b>FOV:</b>	Dual 7° x 3°.
<i>Electronics</i>	
<b>A/D Converter:</b>	15 bits.
<b>Signal Processing:</b>	Phase sensitive detectors with narrow band tuning. Three stage lock-in amplifier. Three decade autoranging.
<b>Gain:</b>	2 decades of automatic gain.
<b>Dynamic Range:</b>	0 to 3x10 <sup>6</sup> digital counts.
<b>Sensitivity:</b>	Sensitivity in highest gain is detector noise limited. S/N ratio is determined by choice of time constant and integration time of the phase sensitive detector and electronic filtering stage.
<b>Scan Time:</b>	Programmable from 60 s - up depending on light level and operator selected speed factor and time constants.
<b>Communication:</b>	Parallel port.
<b>Power Requirements:</b>	Spectroradiometer head batteries (rechargeable gel cells): (1) 12 VDC at 5 to 12 W depending on operating mode. (2) 6 VDC at 3 W.

>> Table 8: Specifications of the GER IRIS Mark V.

**S2000 (Ocean Optics)**

The S2000 spectroradiometer (Figure 29) is a portable spectroradiometer measuring the absolute and relative light energy in the wavelength window from 350 nm to 1000 nm. Inside the instrument light is separated by a grating and detected by a 2048-channel silicon array with a spectral resolution of approximately 1.5 nm. Incident photons are converted to electrons in the sensor bulk material. Photoelectric current is converted to voltage and digitized by a 12-bit Analogue-to-Digital Converter. VITO's instrument is accompanied with a 3 m standard and water resistant fiber of approximately 25 degrees full angle. In combination with a cosine corrector the S2000 measures radiance within 180 degrees. The spectroradiometer can be combined with a second identical spectroradiometer to measure simultaneously upwelling and downwelling radiance which is especially interesting for water applications. The optical bench, optics and CCD array of both S2000 are thermoelectric temperature regulated to limit noise induced by a temperature change. When temperature drifts more than 0.1 °C, a temperature correction is made. The minimum integration time is 3 ms.

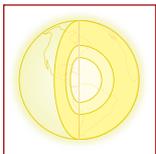
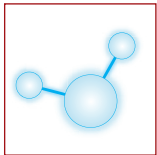


>> Figure 29: Picture of the Ocean Optics spectroradiometer setup.

### **PIMA™ (Spectral International INC)**

The PIMA™ (Figure 30) developed by Spectral International INC is a field portable, infrared spectrometer sensitive in the SWIR wavelength region from 1300 nm – 2500 nm. Measurement are made in a contact mode. The spectral resolution is 7 nm while the spectral sampling interval is 2 nm.



>> Figure 30: PIMA spectroradiometer (<http://www.pimausa.com/pima2.html>).

### **RAMSES spectroradiometer (TriOS)**

The RAMSES instruments developed by TriOS (<http://www.trios.de>) are robust and compact (30 cm long, 1 kg weight in air) CCD-based hyperspectral radiometers available in irradiance or radiance-measuring versions and measuring the UV/VIS range (320-950 nm) at 256 wavelengths with approximately 7 nm Full Wavelength Half Maximum (FWHM) spectral response function width.

Multiple instruments can easily be combined together and with, for example a GPS unit, via a data interface which logs all data simultaneously to a single PC. An example of a three sensor system suitable for seaborne measurements of water-leaving reflectance and an associated measurement protocol is described in HyperTeach Hands-on Lesson 3. For a full technical specification of the instruments the reader is referred to the manufacturers' web site.

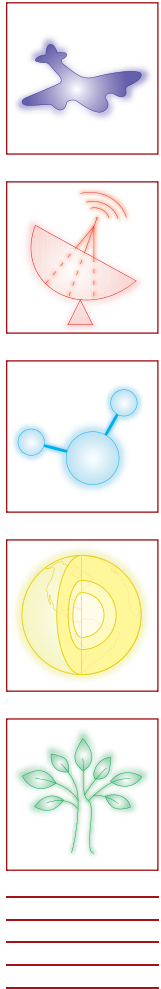


>> Figure 31: Picture of RAMSES ARC hyperspectral radiance sensor ([www.trios.de](http://www.trios.de)).

The RAMSES spectroradiometers described here can be used in combination with solar or artificial illumination. Advantages and disadvantages are listed in Table 9.

Solar illumination	Artificial illumination
Directly correlates with airborne or spaceborne measurement	More efficient measurements
Samples are not modified or disrupted by sampling process	More easily to control illumination and viewing geometry
No signal in atmospheric absorption bands	More easily to control sample geometry
Stable atmospheric conditions are required	More SWIR irradiance
Low SWIR irradiance beyond 2-3 hours from solar noon	Difficult to control distance to light source with irregular samples
Low SWIR irradiance during winter season	Can 'cook' vegetation samples

>> Table 9: Advantages and disadvantages of solar and artificial illumination.

### 5.2.1.1 Sun photometer (Microtops II)

Sun photometers are able to measure parameters that characterise the atmosphere at the time and location of the flight/overpass. The obtained parameters are input values for the radiative transfer model which is often used to atmospherically correct the airborne or spaceborne images. More information can be found in Section 8

The Microtops II (Figure 32) is a hand-held multi-band sun photometer capable of measuring the aerosol optical thickness (AOT) and direct solar irradiance in each band. Furthermore, the sun photometer is capable of deriving water vapour column. Optical depth or optical thickness is a measure of transparency and is defined as the fraction of radiation that is scattered between a point and the observer (think about fog). The instrument is equipped with 5 collimators with full angle of 2.5 degrees. Each channel is fitted with a filter and photodiode suitable for a particular wavelength range (440 nm, 675 nm, 870 nm, 936 nm and 1020 nm). Incident photons captured by the photodiodes, produces an electrical current proportional to the radiant power intercepted by the photodiodes. The analogue signal is amplified and converted to a digital number by a 20-bit Analogue to Digital Converter.

The AOT and water vapour column is calculated assuming Bouguer-Lambert-Beer law (see <http://www.solar.com/ftp/manuals/sunman.pdf> for more background information). The AOT is obtained after subtraction of the optical depth due to Rayleigh scattering from the total optical depth. Optical depth from  $O_3$  and  $NO_2$  is ignored. The water vapour column is based on simultaneous measurements at 936 nm (water absorption peak) and either 870 nm or 1020 nm (no water absorption).



>> Figure 32: Picture of the Microtops II sun photometer.

### 5.2.1.2 Global Positioning System

The Global Positioning System (GPS) is a location and navigation system based on a constellation of 24 satellites orbiting the Earth at altitudes of 20.200 km. The GPS was developed by the United States Department of Defence. In February 1978 the first GPS satellite was launched by the US Military forces. Civilian use only began in the early 1990's. The constellation of satellites and orbits is designed to ensure that at least 4 satellites are observable at all times from any point on Earth. Four satellites are required to calculate a unique position.

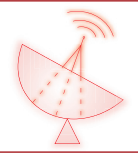
Each satellite transmits ranging signals on two frequencies: link 1 (L1) at 1575.42 MHz and link 2 (L2) at 1227.6 MHz. Two different ranging codes are modulated on the L1 and L2 signals: a 1.023 MHz coarse/acquisition code (C/A code) on L1 and a 10.23 MHz precision code (P code) on both L1 and L2. Either the C/A code or the P code can be used to determine the range between the satellite and the user, but the P code is normally encrypted and available only to authorised (military) users. A 50 Hz navigation message is superimposed on both the C/A and the P code. The navigation data includes satellite clock-bias data, satellite ephemeris (orbital) information, ionospheric signal propagation correction data and the satellite almanac for the entire constellation of satellites.

Based on the previous, GPS receivers can be divided into two categories:

- C/A code receivers: use the C/A code modulated on the L1 carrier signal to calculate a position
- Carrier phase receivers: use the L1 and L2 carrier signals to calculate a position

Another distinction often made is the one between single band receivers (they register only the L1 frequency) and dual band receivers (they register both L1 and L2). With dual band receivers higher positional accuracies (up to mm level) can be obtained since they are capable of making Real-Time Kinematic (RTK) observations (<http://www.atra.mod.uk/atra/rsabst/pdf/K-GPS/k01-gps.pdf>, <http://www.gpsworld.com>). VITO uses both types of GPS receivers: the single banded Trimble GeoXT (Figure 33) and the dual band Leica SR530 (Figure 34).

The interested reader can find more information about the theoretical background of GPS in some reference books on this topic (Hofmann-Wellenhof et al., 2001; El-Rabbany, 2002).



## Trimble GeoXT



>> Figure 33: Trimble GeoXT handheld GPS.

The Trimble® GeoXT is a handheld device, member of Trimble's GeoExplorer series. It is the most powerful single band GPS of Trimble that combines GPS with GIS functionalities. It is equipped with integrated Bluetooth for wireless connectivity to other Bluetooth-enabled devices, including cell phones and PCs. The GeoXT runs multiple applications, connects to the Internet, and has a familiar user interface. Although this is a single band receiver, sub meter accuracy\* is possible via differential-GPS (EVEREST technology is used for extra multipath correction near tall buildings which block GPS data and generate false data). The GeoXT has limited carrier phase capabilities; i.e. it is capable to process the carrier phase signals but it takes at least 10 min to come to an RTK precision of 30 cm\* (in post-processing). Real-time corrections from the integrated WAAS/EGNOS ([http://www.nav-now.co.uk/what\\_are\\_waas\\_and\\_egnos.htm](http://www.nav-now.co.uk/what_are_waas_and_egnos.htm)) receiver result in accuracies around 2-3 m\*.

The key features of this device are:

- single frequency (L1) receiver
- 12 channels
- position update rate: 1 Hz
- WAAS and EGNOS real-time corrections
- EVEREST multipath rejection technology to enhance accuracy near tall buildings
- Integrated Bluetooth for wireless connectivity
- Accuracy: theoretically 0.5 m – 1 m after d-GPS (real-time & post-processed)

## Leica SR530



>> Figure 34: Leica SR530 base station GPS.

The SR530 is a 24 channel, dual-frequency receiver with on-board RTK capabilities. It is the top model of the System 500 range, combining high performance with exceptional economy. The SR530 can be used either as

a reference or rover (VITO often uses this device as reference station). It can be set to receive either Leica or the standard RTCM (Radio Technical Commission for Maritime Services) format. The SR530 receivers are based on Leica's ClearTrak technology providing the best signal reception, satellite tracking, jamming resistance and multipath mitigation. Since it is a dual-band receiver it is able of measuring positions with very high accuracy (RTK), up to a few mm\*.

The key features of this device are:

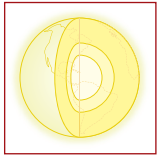
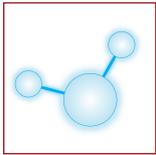
- dual band (L1 & L2) receiver
- 24 channels (12 L1 & 12 L2)
- position update rate: 10 Hz
- ClearTrack technology to reduce multipath, enhance signal-to-noise and resist to jamming
- Accuracy: 5 mm (RTK, stationary observations); 10 mm (RTK, moving); 25 cm (d-GPS using C/A code)

\*All accuracies mentioned are planimetric accuracies (in X/Y plane), expressed as RMSE. Accuracy in height (Z) = 2x positional accuracy.

### **5.3 Other auxiliary data**

Satellite remote sensing data is generally supplied as top-of-atmosphere (TOA) calibrated radiance or reflectance data, sometimes called Level 1, or bottom-of-atmosphere (BOA), sometimes called level 2 or atmospherically-corrected, calibrated radiance or reflectance data. For well-supported global missions the sensor calibration is usually assumed by users to be acceptable and it is not efficient to perform extra ground-based measurements to try to improve on this.

Atmospheric correction remains a critical problem for water applications and ground-level measurements of water-leaving reflectance by radiometer systems and/or of atmospheric optical properties by sun photometer systems may be necessary for the validation or improvement of BOA data. In some cases auxiliary data of use for atmospheric correction may be bundled with imagery as is the case, for example, with ozone and wind speed data from operational meteorological models, which is supplied with SeaWIFS data.

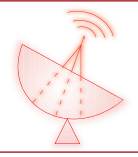




## 6 Sensor calibration

A well-calibrated imaging spectrometer is indispensable to guarantee the extraction of accurate information from imaging spectroscopy data.

Any sensor tends to drift over time, resulting in uncertainties. Periodic calibration is necessary to monitor the performance of the sensor over time. The objective of a sensor calibration is to characterise the sensor response in SI (Système International) units. Three broad calibration categories can be distinguished: lab calibration, in-flight calibration and vicarious calibration. Ideally, a lab calibration is performed before and after data acquisition. A lab calibration, the most time consuming of all the calibration categories, is performed in a controlled and stable laboratory with calibrated lamps. However, due to transport, mounting and operation conditions may differ from the conditions in the lab. Therefore in-flight calibration and vicarious calibration are necessary to verify the sensor's lab calibration during operation.



### 6.1 Lab calibration

There are three fundamental lab calibrations that need to be performed to convert the detector response to SI units: geometric, spectral and radiometric calibration.



#### 6.1.1 GEOMETRIC CALIBRATION

The purpose of the geometric calibration is to determine the spatial response function of each detector element. To achieve this a high precision tilt stage is used to direct a collimated beam into the Field Of View and scan the spatial response for each detector element across track.



#### 6.1.2 SPECTRAL CALIBRATION

The objective of the spectral calibration is the determination of the centre wavelength and the width for each detector element. For the spectral calibration of a spectrometer a wavelength standard with discrete emission or absorption lines throughout the complete sensitivity region of the spectrometer is used. The wavelength of the individual lines is very accurately known. Wavelength standards are often gas discharge lamps or filters. More accurate but also more expensive is to use a monochromator for the spectral calibration of the spectrometer. The objective of the spectral calibration is to assign a wavelength to each row of the detector array. The row to wavelength function is a linear function (assuming the alignment is perfect).

#### 6.1.3 RADIOMETRIC CALIBRATION

For the radiometric calibration of a spectrometer a radiance standard, that is a stable, uniform and Lambertian source of radiation, is used. Often an integrating sphere containing a standard lamp is used to reach these requirements. The current and luminance level of the source are tunable. For a certain current and luminance level the spectral radiance over the spectral range of the detector at the exit hole of the integrating sphere is known. This known radiance can be compared after spectral calibration and dark signal correction with the response (in DN) of the spectrometer to allow radiometric calibration. The detector response is assumed to be linear (Figure 35).

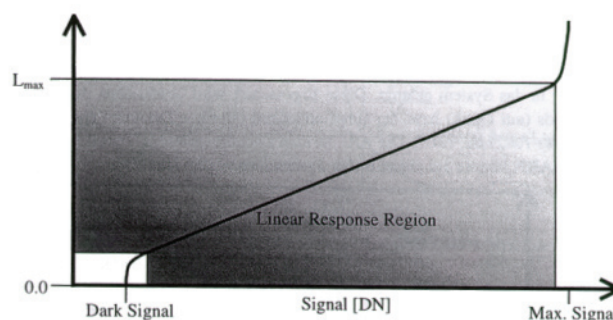
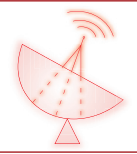


>> Figure 35: Relation between DN and radiance.



**6.2 Bundle adjustment**

To eliminate the positional offsets between the INS, the GPS and the hyperspectral sensor a method from photogrammetry called bundle adjustment is used in combination with differentially corrected positions of ground control points (GCP's). A bundle adjustment has to be performed each time after installation of the instruments.



**6.3 In-flight calibration**

The frequency of in-flight calibrations is higher than the cost- and labour intensive lab calibration. Often an on-board lamp is used as reference. An in-flight calibration is not a full calibration, but is a check of the lab calibration.



**6.4 Vicarious calibration**

The vicarious calibration is a means to validate the lab calibration. For the vicarious calibration simultaneous with the data acquisition, in-situ measurements are performed either in radiance or reflectance units. Atmospheric input parameters are necessary to model the atmosphere in order to link sensor data with in-situ data.



## 7 Geometric correction

### 7.1 Geometric distortions in airborne imagery

Raw airborne images suffer from spatial distortions due to the frequent motions of the aircraft caused by side winds and air turbulences. Mounting the sensor on a stabilised platform will reduce these distortions, however it can not compensate for all disturbances.

In general two types of geometric distortions are distinguished: internal and external distortions.

1. **Internal distortions** mainly result from the geometric characteristics or performance of the sensor, such as lens optics distortion, alignment error of CCD array, variation of sampling rate, ....
2. **External distortions** are caused by external parameters other than the sensor. This includes variation of the attitude and altitude of the aircraft, and differences in terrain elevation, i.e. topography. The attitude of the aircraft is expressed as roll, pitch, yaw. These effects are illustrated in Figure 36. The movement of the wings up or down is called roll. Pitch is the up or downward movement of the aircraft's nose. Yawing occurs when the the aircraft is flying straight and then turns its nose left or right.

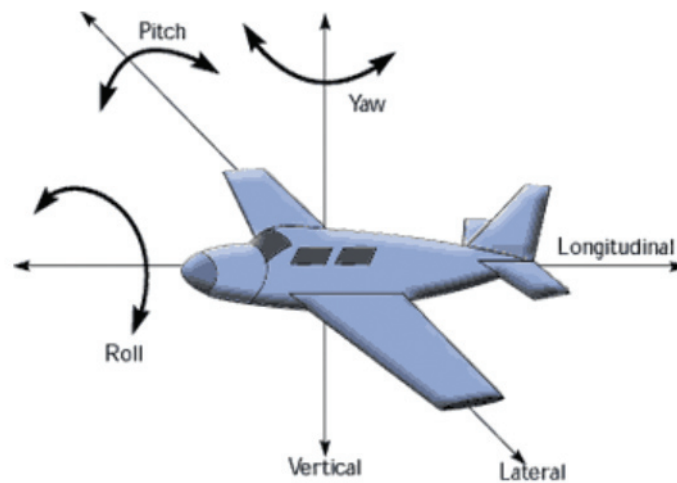


>> Figure 36: Roll, pitch, yaw. (Source <http://virtualskies.arc.nasa.gov/aeronautics/tutorial/motion.html>)

Changes in the attitude and altitude of the aircraft and topography variation cause distortions in the geometry of the recorded image. These distortions are summarised by Breuer and Albertz, 2000:

**Roll distortion:** The roll distortion yields offsets across the track. The amount of one offset remains not constant even for a constant roll angle. It grows with an increasing scan angle of the line-of-sight (Figure 37).

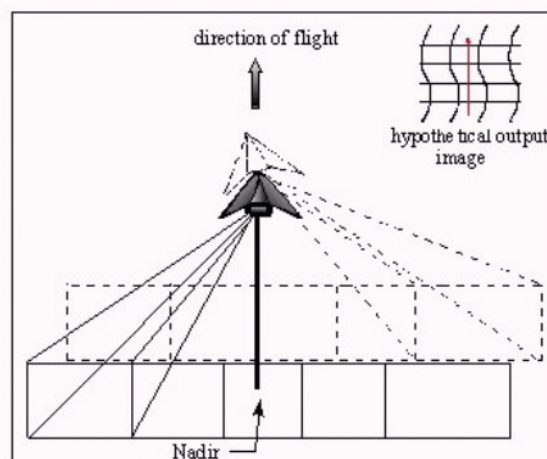


>> Figure 37: Scan-angle dependent roll distortion. (Source: [www.cis.rit.edu/research/thesis/bs/1998/kopacz/thesis.html](http://www.cis.rit.edu/research/thesis/bs/1998/kopacz/thesis.html)).

**Pitch distortion:** Movements of pitch can be important if they led to gaps in the image data. This can arise due to sudden forward or backward shocks that cannot be compensated by the stabilized platform. As a consequence some areas of the terrain are depicted repeatedly (over-sampled) whereas other parts remain unscanned (under-sampled) (Figure 38).

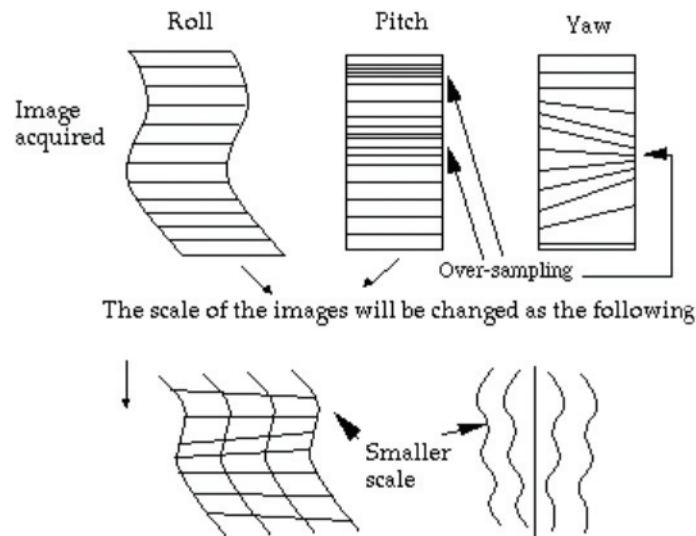


>> Figure 38: The effects of roll, pitch and yaw on image geometry  
(Source: <http://www.cnr.berkeley.edu/~gong/textbook/chapter4/html/sect42.htm>).

**Relief displacement** (Figure 39): Elevation differences of the terrain result in displacements that increase with growing scan angle. This effect is emphasized with increasing object height and distance from the nadir line. This is illustrated in

**Table 10** which gives the location error as a function of the scan angle and DEM elevation error.

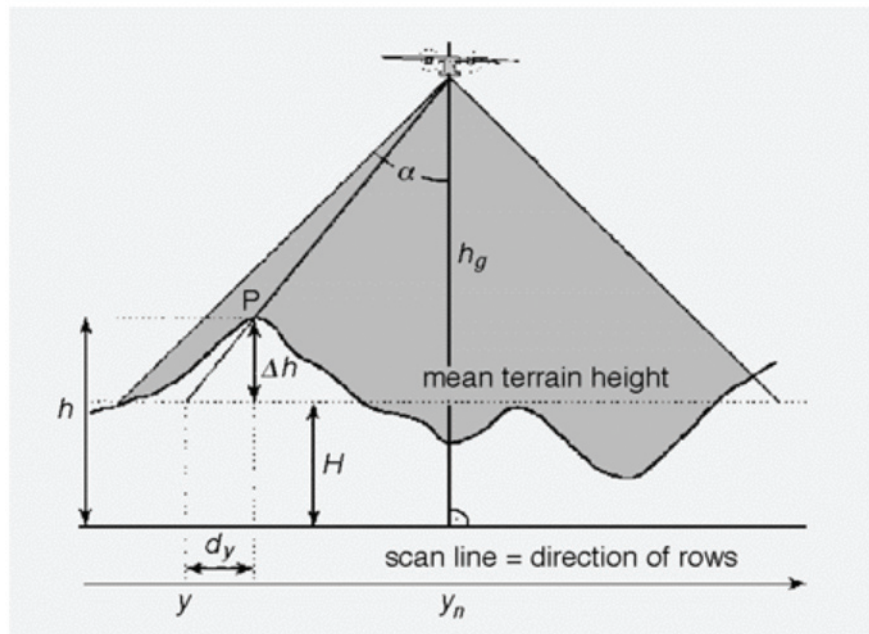
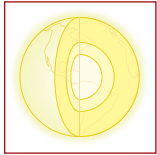
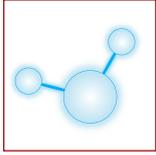


>> Figure 39: Relief displacement.



LOCATION ERROR (m)	Off-Nadir Scan Angle		
	10°	15°	20°
DEM vertical error			
$\Delta h = 5 \text{ m}$	0.9	1.3	1.8
$\Delta h = 10 \text{ m}$	1.8	2.7	3.6
$\Delta h = 20 \text{ m}$	3.6	5.4	7.3
$\Delta h = 50 \text{ m}$	8.8	13.4	18.2

>> Table 10: Location error (horizontal offsets from nadir) as a function of the scan angle and DEM elevation error.

These external geometric distortions need to be compensated for in the post-processing. Geometric correction methods are based on (1) parametric methods (7.1.2), (2) on polynomial mathematical models (7.1.3) or (3) on hybrid methods which are a combination of both.

## 7.2 Parametric geometric correction

The parametric geometric correction physically models the transformation between the image and ground spaces. The approach requires accurate auxiliary data like image/sensor general information, attitude (roll, pitch, yaw) and position information (latitude, longitude, altitude) of the sensor measured during the flight. The parameters are recorded with an Inertial Navigation System (INS) in combination with a Global Positioning System (see Sections 3.5.1.1 and 3.5.1.2). The local heights of the terrain must be provided in a Digital Terrain Model (DTM). The method is critically dependent upon the accurate and rapid measurement of the sensor exterior orientation (position and attitude). When these data are available with low accuracy only, some ground control points are still required to achieve good results. An example of commercially available geocoding software is PARGE. Interested readers are referred to the website of PARGE (<http://www.rese.ch/parge/index.html>).

## 7.3 Ground control points/polynomial mathematical models

In case no software is available for performing the parametric geocoding a non-parametric approach can be used. This approach requires a number of Ground Control Points (GCP's). Disturbances are corrected by applying a polynomial mathematical function. A disadvantage of this approach is that no information about the sensor position and attitude is used and that distortions caused by topography are not accounted for. This can result in low-fitting accuracy because of the local character of the distortions.

The non-parametric geometric correction consists of four steps, described below.

A more in depth discussion can be found in Section 2.2.2 of the Introduction to Satellite Remote sensing Module 1: Basic Concepts, K.U. Leuven.

### 1. Select Ground Control Points (GCPs)

Ground control points can be selected from maps and/or from field surveys. Some rules for selecting the ground control points are:

- Extractability: A good ground control point is a point that is perfectly known on the ground (or the reference map) and is perfectly identified on the image. Examples are : intersections of roads, towers, buildings, shoreline features
- Distribution: The GCPs should be selected throughout the whole scene and be placed as much as possible into the edges of the image
- Number: The number of GCPs should be sufficient for the polynomial transformation (see step 4)
- Stability: GCPs should not change over time. This is particularly important when using reference maps which are far older than your image. For obvious reasons moving objects like cars can't be used as GCPs!

### 2. Extract Pixel locations and map coordinates for each GCP

The next step is to create a table which lists the image coordinates (lines, pixels) and map coordinates (e.g. longitude, latitude) for the selected GCPs.

### 3. Determination of the transformation formula

A transformation equation has to be determined to interrelate the map reference coordinates to the image coordinates :

$$\begin{aligned}
 x' &= f1(x,y) \\
 y' &= f2(x,y) \\
 (x', y') &= \text{distorted image coordinates (column, row)} \\
 (x, y) &= \text{reference-map coordinates} \\
 (x'_r, y'_r) &= \text{retransformed reference-map coordinates (column, row)} \\
 f1 \ f2 &= \text{transformation functions}
 \end{aligned}
 \tag{7.1}$$

A wide range of transformation may be used to model the geometric distortion. These include :

- Linear Transformation (1<sup>st</sup> order polynomial): In case at least 3 GCPs are available a 1<sup>st</sup> order transformation can correct for translation, rotation and scaling in the two dimensional XY-space,

$$\begin{aligned}
 x' &= a_0 + a_1 x + a_2 y \\
 y' &= b_0 + b_1 x + b_2 y
 \end{aligned}
 \tag{7.2}$$

- Non-Linear Transformation (N-th order polynomial): More complex warpings can be achieved with a higher order polynomial. It is important to note that while a higher order polynomial will result in a more accurate fit in the immediate vicinity of the GCPs, it may introduce new significant errors in those parts of the image away from the GCPs.

To determine the transformations required to restore the image the Root Mean Square Error (RMSE) should be analysed. The RMSE is defined as:

$$RMSE = \sqrt{(x' - x'_r)^2 + (y' - y'_r)^2}
 \tag{7.3}$$

It indicates the difference between the desired output coordinate value for a GCP and the retransformed coordinate value. The residuals are used to check for outliers (i.e. where you have identified an incorrect control or check point) and to determine the quality of the transformation. The best order of transformation can be obtained using trial and error process.

### 4. Resampling and interpolation

This step determines the brightness value (DN, radiance or reflectance) for each pixel in the final geometrically corrected image. This is required because cells in the output matrix will not directly overlay a pixel in the original image. Three commonly used methods exist to determine the brightness value for each output pixel based on the input pixel (Burrough and McDonnell, 1998):

- Nearest Neighbour: The value closest to the output cell is assigned to the output cell (Figure 40). This is a zero order resampling.

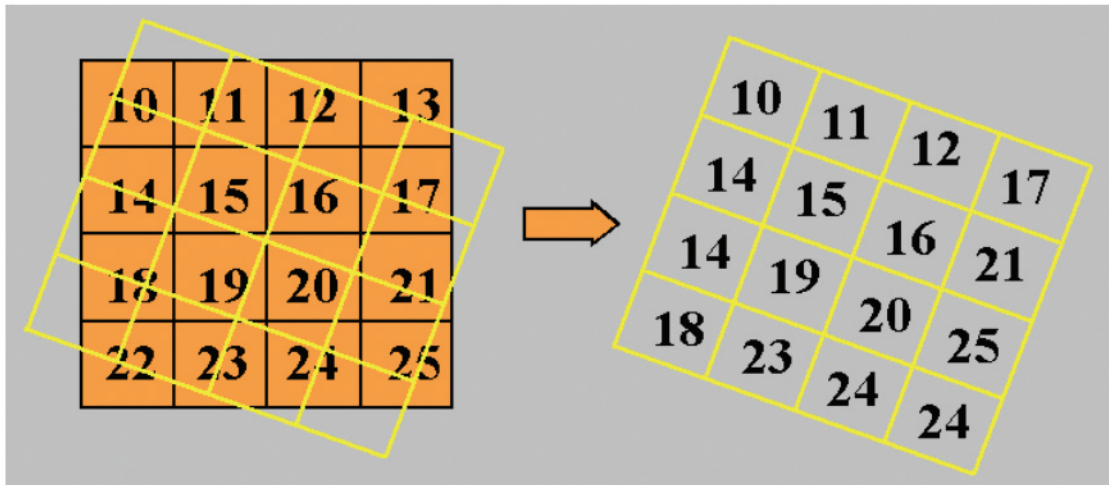


>> Figure 40: Nearest neighbouring method (Source : <http://www.nr.usu.edu/Geography-Department/rsgis/RSCC/v6.2/nn.html>).

- Bilinear Interpolation : Calculates the output cell value by calculating the weighted average of the four closest input cells (a 2x2 array) based on weighted distance.
- Cubic Convolution : Calculates the output cell value by calculating the weighted average of 16 surrounding input pixels (a 4x4 array).

## 7.4 Geometric correction of spaceborne imagery

### 7.4.1 AUXILIARY DATA FOR GEOREFERENCING OF SPACEBORNE IMAGERY

The georeferencing of satellite data can often be achieved without extra ground measurements by the user, who may typically rely on georeferencing information supplied by the satellite data provider possibly supplemented by the user via easily identifiable Ground Control Points in the image as described in Section 7.1.3.

Exceptions may occur for very homogeneous targets such as desert or particularly for offshore waters in regions without large buoys or platforms. In such cases a user of satellite data may need to deploy his/her own targets (e.g. buoy or boat for a water application or a large coloured sheet for a land application) of sufficient size and suitable colour to be visible in imagery.

For satellite imagery, georeferencing information is generally supplied embedded within the data file in the form of latitude and longitude coordinates for a regular grid of tie-points within the image or minimally (for small region images) at the image corner and centre points. The stable and well-controlled flight of spaceborne systems simplifies greatly the georeferencing of data and the problems of roll and pitch distortion described for airborne data (see Section 7.1.1) are generally avoided.

Georeferencing information supplied by satellite data providers is based on orbit predictions and/or navigation parameters measured onboard the satellite and on a simple geometric model of the Earth's surface and the sensor's optical geometry. This automated production of georeferencing information may be improved by a human operator, who will usually be the user. Though in certain cases (e.g. SPOT4 VEGETATION) it may be the satellite data provider. This human operator will identify Ground Control Points in imagery as described in Section 7.1.3 and correct the imagery accordingly. Errors in the georeferencing of satellite data, except those related to relief displacement (Section 7.1.1) are generally very systematic and many can be corrected with simple linear transformations (1<sup>st</sup> order polynomial).

As an example, slight errors in the satellite time for AVHRR sensors give a georeferencing error which can be corrected by a simple translation which will be fairly constant over a scene unless the region of interest covers many hundreds of kilometres. As a second example, errors in pointing of the CHRIS sensor onboard PROBA give a georeferencing error that can be well-corrected by a (linear 1<sup>st</sup> order) transformation combining rotation and translation.

## 8 Atmospheric correction

### 8.1 Land

#### 8.1.1 AIRBORNE AND SPACEBORNE

When electromagnetic radiation passes through the atmosphere it may be transmitted, scattered or absorbed. Scattering is the redirection of the electromagnetic radiation by suspended particles in the air or by large molecules of atmospheric gasses. There are three different types of scattering: **Rayleigh scattering**, Mie scattering and non-selective scattering. Rayleigh scattering mainly consists of scattering from atmospheric gases. This is caused by particles much smaller than the wavelengths scattered. This type of scattering is therefore wavelength dependent. The amount of scattering is proportional to  $\lambda^{-4}$ . This strong wavelength dependence of the scattering means that blue light is scattered much more than red light. It is the dominant scattering type in the atmosphere. If the atmospheric particulates are of roughly the same size as the wavelength of incident radiation, **Mie scattering** becomes important. It is caused by pollen, dust, smoke, water droplets and other particles in the lower portion of the atmosphere. Mie scattering is responsible for the white appearance of the clouds. Mie scattering is not strongly wavelength dependent. The last type of scattering is **non-selective scattering**. It occurs in the lower portion of the atmosphere when the particles are much larger than the incident radiation. This type of scattering is not wavelength dependent and is the primary cause of haze.

Absorption occurs when the radiation is absorbed by some of the constituents in the atmosphere. Energy that is absorbed is then re-emitted at a longer wavelengths. An absorption band is a range of wavelengths in the electromagnetic spectrum within which electromagnetic energy is absorbed by one of those constituents. Major absorbers of solar radiation are (1) ozone, (2) oxygen, (3) water vapour and (4) carbon dioxide as illustrated in Figure 41.

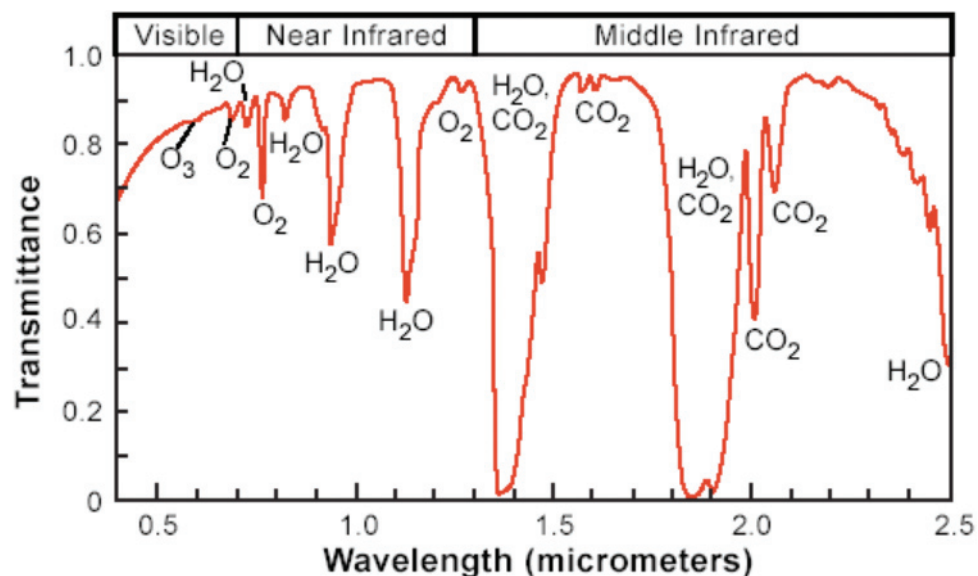


>> Figure 41: Plot of atmospheric transmittance versus wavelength.  
(Source : <http://www.microimages.com/getstart/pdf/hyprspec.pdf>)

The radiation from a land target that is received by a sensor comes from different sources as shown in Figure 42. First there is the radiation reflected by the target and directly transmitted into the Field Of View of the sensor; secondly, the atmospheric path radiance, this is the radiant energy diffusely scattered by the atmosphere and which found its way into the sensor Field Of View without having interacted with the land surface; thirdly, the radiant energy which is reflected off the nearby surface (adjacency effect). Only the radiant energy reflected by the target contains information about the target. In order to make comparisons between image spectra and laboratory reflectance spectra, an atmospheric correction is required to remove the other contributing effects, i.e. the atmospheric path radiance and the adjacency effect. Sensor offset (internal instrument noise) should also be corrected.

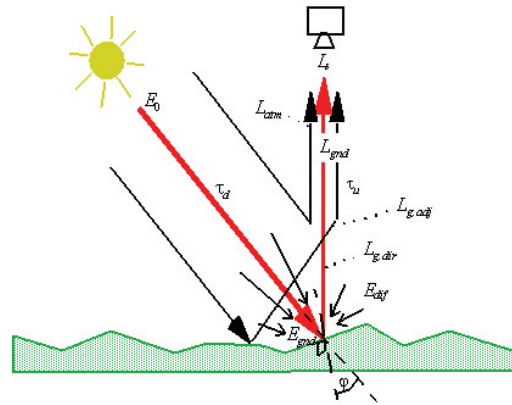
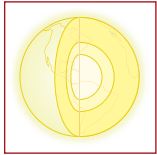
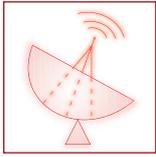


>> Figure 42: Sources of radiation received by a remote sensor.

The atmospheric correction approaches could be classified into (1) scene-derived corrections, (2) ground-calibrating methods and (3) radiative transfer models.

## 8.1.2 SCENE-DERIVED CORRECTIONS

### 8.1.2.1 Flat Field

The Flat Field correction method normalizes images to an area of known “flat” reflectance. The method is particularly effective for reducing hyperspectral data to relative reflectance. It assumes that somewhere in the image there is an area which fulfil following “flat field” criteria: (1) topographically flat; (2) spectrally flat, i.e. uniform spectral reflectance at all wavelengths without significant absorption features; (3) bright in order to reduce the effects of random image noise on the correction. The average flat field spectrum is almost pure signature of solar irradiance plus superimposed atmospheric scattering and absorption effects. The Flat Field method normalises each image spectrum to the flat field spectrum. With an appropriate flat field spectrum, this procedure will largely remove atmospheric and solar irradiance effects.

### 8.1.2.2 Internal Average Relative Reflectance (IARR)

This calibration technique is also known as Equal Area Normalisation (EAN) and normalises the image to a scene average spectrum. An average spectral radiance spectrum is calculated from the entire input image. This average spectrum is used as the reference spectrum. Each pixel of the image is then normalised to the reference spectrum. This shifts all spectral radiances to the same relative brightness. The resulting spectral values represent reflectance relative to the average spectrum. The method works best in arid climates with no vegetation. The IARR method has the advantage that no a priori knowledge of the site is required. A disadvantage is that the resulting reflectance may have some artefacts due to the fact that the average spectrum may include absorption features related to these surface materials instead of representing only atmospheric and solar irradiance effects.

## 8.1.3 EMPIRICAL LINE CALIBRATION

The Empirical Line Calibration technique is used to force image data to match selected field reflectance spectra. A limitation of this technique is that it requires field or laboratory reflectance spectra of at least two uniform ground targets. These targets should meet the following criteria: (1) be homogeneous, i.e. the pixel to pixel variations in the reflectance spectra are low; (2) be large enough to recognize the area in the image, as a rule of thumb the size of the target should be at least 5 times the pixel size; (3) the target should represent the albedo diversity of the scene, therefore at least one dark and one bright target should be used; (4) be near-Lambertian; (5) be featureless in terms of absorption features.

The targets are identified in the image and the average radiance spectra are extracted. For each spectral band a linear regression is calculated between the reference spectra and the image spectra (Figure 43). This way the linear transformation (gain and offset) for radiance to reflectance conversion is determined for each spectral band. The slope of the calculated line quantifies the combined effects of the multiplicative radiance factors (gain), while the intercept with the radiance axis represents the additive component (offset). Gain and offset are then used to predict the apparent reflectance spectrum for each pixel from its original image radiance spectrum.

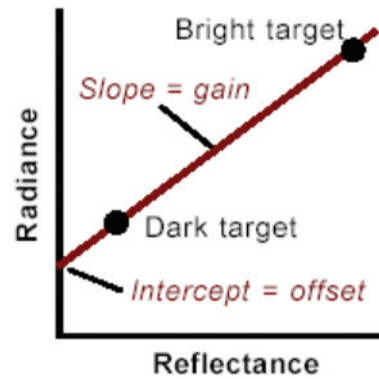
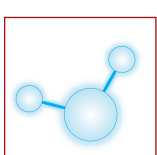
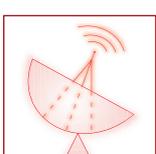
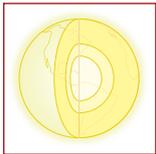


>> Figure 43: Reflectance conversion parameters for a single image band using known target reflectance values. (Source : <http://www.microimages.com/getstart/pdf/hyrspec.pdf>).

The final values should be considered as "apparent" reflectances because the conversion does not account for possible effects of topography within the scene. Topography introduces shading and atmospheric path length differences.

### 8.1.4 RADIATIVE TRANSFER CODES

Radiative transfer models, like the 6S model (Vermote et al., 1997) or MODTRAN (Berk et al., 1998), can be used to predict the atmospheric radiative properties and to model the radiance at the sensor. Several physical based atmospheric correction models such as ATCOR (Richter, 1996 and Richter, 2002), WATCOR (VITO), ATREM/TAFKAA (Gao and Davis, 1997 and Gao et al., 2000), ENVI/FLAASH (Research Systems, Inc.), ACORN (Analytical Imaging and Geophysics, LLC) and HATCH (Qu et al., 2000) are based on these radiative transfer models to convert at-sensor radiance images to apparent reflectances. These model-based methods require information on the flight geometry (heading, flight altitude), illumination and viewing angles and the atmospheric conditions (visibility, aerosol type, water vapour, ...) during the flight. The atmospheric parameters should be obtained through in-situ measurements (sun photometer and radiosonde data), estimated from the image itself or approximated from 'standard' atmospheres.

The models start with a simulated solar irradiance spectrum, then compute the scene radiance effects of solar elevation (derived from the day and time of the scene) and atmospheric scattering and absorption.

In the absence of measurements of actual atmospheric conditions, the user must estimate some input parameters, such as the amount and distribution of scattering agents. Absorption by well-mixed gases ( $\text{CO}_2$  and  $\text{O}_2$ ) is assumed to be uniform across a scene but absorption due to water vapour is often variable. Water vapour absorption effects can be estimated and corrected individually for each image pixel using portions of the spectra that include water absorption bands.

The final apparent reflectance values may still incorporate the effects of topographic shading, however.

## 8.2 Atmospheric correction for water

### 8.2.1 DESCRIPTION OF PROBLEM

For water targets the theory of atmospheric scattering and absorption is similar to that for land targets but with two important exceptions:

1. For water targets the air-water interface is an extra complication. Only photons which have penetrated the air-water interface and been scattered or absorbed by the water itself contain useful information. Photons which are reflected by the air-water interface have not interacted with the water and its constituents and thus represent an unwanted signal which must be removed. In general the atmospheric correction for water targets will group this air-water interface reflection with the atmospheric path radiance.
2. Water is generally much darker than land, often by a factor 10 or 100 or more and especially in the red and near-infrared where water absorbs very strongly. The signal detected by an airborne or spaceborne sensor may consist of up to 90% or more light scattered by the atmosphere or the air-water interface. An accurate atmospheric correction thus becomes very important since any errors in evaluating this large contribution

to the detected signal will yield very large relative errors for estimation of the signal from the water. In fact atmospheric correction is often the biggest problem when attempting to quantify water parameters such as total suspended matter (TSM) or chlorophyll *a* concentration from remote sensing imagery.

Figure 44 shows a schematic of photon paths for the case of single scattering in the atmosphere, at the air-water interface or in the water. Reality is more complicated than this single scattering picture because photons reaching the sensor may have undergone multiple scattering interactions in the atmosphere, at the air-water interface and in the water.

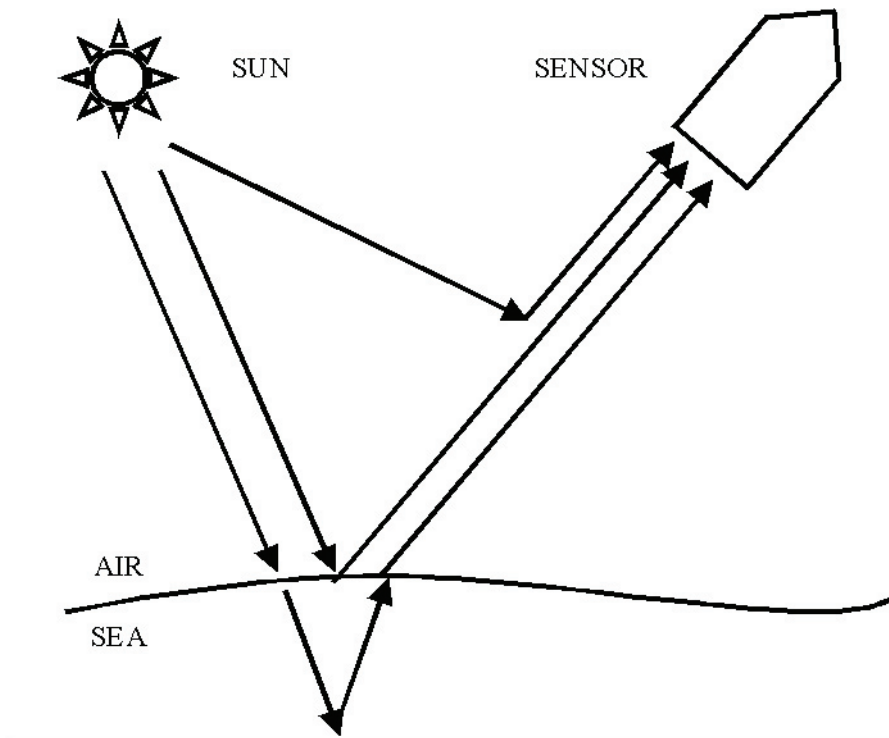


>> Figure 44: Photons paths from sun to sensor with a single scattering event in the atmosphere, at the air-water interface or in the water body.

Atmospheric processes for optical remote sensing of water are generally divided in four main classes:

1. **Absorption from gas molecules** (see also Section 8.1.1), the most important of which are water vapour (significant between 700 nm and 1000 nm), ozone (broadband absorption between 500 nm and 700 nm) and oxygen (a strong but spectrally narrow absorption band near 762 nm). In most cases the atmospheric absorption can be reliably estimated from the sun and viewing geometry and possibly climatological or auxiliary data for, e.g., total column ozone content. However, for the 900-1000 nm spectral region the water vapour absorption is so significant that no useful information on water targets can be retrieved for this range. Obviously absorption from gas molecules of photons traveling from the sun towards the water target or back from the target to the sensor will decrease the quantity of light detected. The atmospheric correction procedure will estimate this reduction factor and multiply the detected light accordingly.
2. **Rayleigh scattering from gas molecules** (see Section 8.1.1) is a very significant source of extra detected light which must be removed by atmospheric correction. The strong wavelength dependence of scattering by air molecules gives much more blue scattering than red (the sky is blue in the absence of clouds or haze). In fact, atmospheric scattering at wavelengths such as 412 nm or less is so significant compared to the desired signal from water targets that it is common for atmospheric correction to fail or give totally unusable results for such wavelengths.
3. **Aerosol scattering from particles in the atmosphere** (a combination of the Mie scattering and non-selective scattering mentioned in Section 8.1.1) is another source of extra detected light which must be removed by atmospheric correction. This contribution to the detected signal has less strong wavelength dependence than Rayleigh scattering and may be approximately white (wavelength-independent) for many marine and coastal situations, except if there is considerable influence from aerosols of urban origin or high

altitude or absorbing aerosols. The difficulty for atmospheric correction is that the aerosol scattering is highly variable in space and time and, thus, impossible to estimate from geometrical (sun and sensor angles) and climatological data alone.

4. **Air-sea interface reflection**, although not strictly-speaking an atmospheric process, is generally grouped with atmospheric processes in the atmospheric correction. The air-sea interface reflection can be further subdivided into sky glint (the specular reflection of sky light), sun glint (the specular reflection of direct sun light) and diffuse reflection from whitecaps. The sky glint is similar to the atmospheric Rayleigh scattering in colour and origin and so these are generally calculated together. Sun glint is the very bright reflection of the sun which can be seen when looking at the water in the direction of the sun. For a very calm sea this is like a mirror reflection of the sun but the presence of waves usually makes this reflection non-uniform in space and glittering with many short-lived but very bright flashes of light. In general sun glint cannot be corrected and sensors must be directed away from the direction of direct sun reflection. Finally for water subject to strong wind or other sources of breaking waves the "whitecaps" or white foam at the surface can reflect significantly sky and sun light from all directions as a diffuse reflector. Because the rest of the water surface is typically dark the whitecap reflection can be relatively significant for high wind speeds (e.g. greater than 10 m/s when measured at 10 m above sea level) when a reasonable fraction of the water surface is covered by whitecaps.

### 8.2.2 ATMOSPHERIC CORRECTION OF AIRBORNE DATA FOR WATER APPLICATIONS

In general the atmospheric correction of airborne data for water targets is achieved by running a atmospheric radiative transfer model with user-defined inputs for parameters such as sun and viewing geometry, sensor altitude, aerosol concentration and type or horizontal visibility, etc. Such models calculate scattering and absorption in the atmosphere and estimate what the atmospheric component of the at-sensor radiance should be corresponding to the defined inputs. These are termed "forward" models in contrast to the "inverse" models which calculate what the atmospheric parameters are for a given at-sensor radiance.

With a forward model it is important to have ground-based measurements or knowledge of one or more reference targets in an image to check that the user-defined input atmospheric parameters were accurately estimated. For example, if it is known that a reference target such as an airport runway or a stretch of sandy beach has a known reflectance (or that a water body in the scene has almost zero near-infrared reflectance) then this information can be used with the forward atmospheric model to check that the forward modeled at-sensor radiance corresponds to the measured at-sensor radiance for that target. In the case of discrepancies the input parameters to the atmospheric radiative transfer model, especially those relating to aerosols or horizontal visibility, can be varied interactively until a good match is achieved. Ground-based atmospheric measurements such as aerosol optical depth from a sun photometer may also be used to set one or more of the forward model input parameters. For easy of use the forward radiative transfer model can be prepared with a graphical-user interface as illustrated in Figure 45 for the WATCOR software.

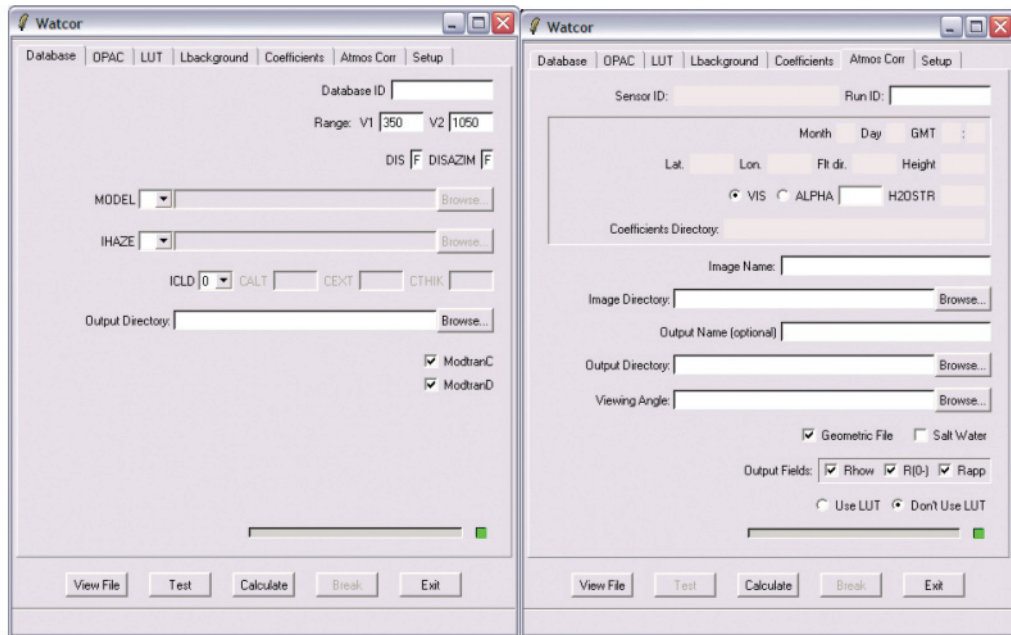
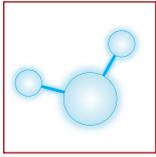
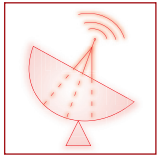


>> Figure 45: Screen print of the graphical user interface of the WATCOR software used for atmospheric correction of airborne imagery.

### 8.2.3 ATMOSPHERIC CORRECTION OF SPACEBORNE DATA FOR WATER APPLICATIONS

The interactive use of a forward atmospheric radiative transfer model as described for airborne data can also be used for spaceborne data. However, in general the processing of spaceborne data is highly automated to achieve an economy of scale for global missions and is often under the responsibility of national or international space agencies. The need for automation means that scene-specific reference targets are not generally available and atmospheric correction must be achieved using only the satellite data, possibly supplemented by auxiliary data available from global meteorological models and sometimes bundled with satellite data (e.g. SeaWiFS image data is supplied with auxiliary data for wind speed and ozone column content). In this context interactive forward models cannot be used and only inverse models working back from the satellite image data can be used. The calculations necessary for atmospheric correction generally represent the biggest task of a satellite data processing chain both in terms of programming lines and CPU time. A full description of such calculations is beyond the scope of this course. The reader interested in such details is referred to the SeaDAS software, provided free of charge by NASA for processing SeaWiFS imagery. The SeaDAS software is available publicly in source code version and is supported by an impressive collection of documentation describing both scientific algorithms and usage instructions. Here we summarise merely the main steps of atmospheric correction contained within data processing software such as SeaDAS:

- The atmospheric correction procedure takes as primary input the light detected by the sensor and calibrated as absolute spectral radiance or, more commonly, spectral reflectance after normalization of spectral radiance by the extraterrestrial downwelling irradiance.
- The absorption of the atmosphere is calculated for the sun and viewing geometry possibly supplemented with auxiliary data such as ozone column content.
- The atmospheric Rayleigh scattering and sky glint reflection are calculated for the sun and viewing geometry, usually with auxiliary data for water-level atmospheric pressure (the atmosphere column above a high altitude lake or for the sea under a low pressure system contains less molecules and hence gives less Rayleigh scattering).
- The atmospheric aerosol scattering is calculated by assuming that the water reflectance is zero in the near-infrared (for example the 765 nm and 865 nm bands of SeaWiFS) and calculating the aerosol concentration and type necessary for each pixel to achieve this. For turbid waters the near-infrared water reflectance is non-zero and a more complicated procedure is necessary to calculate the aerosol reflectance.
- Whitecap reflectance can be calculated from auxiliary data for wind speed or may be neglected for low wind



speed. Sun glint is usually not calculated but imagery is simply masked (not used) if the viewing direction is likely to be contaminated by sun glint.

- The above calculations are combined to estimate the total atmospheric path radiance and transmittance and hence correct the at-sensor reflectance to give the water-leaving reflectance. In general, this combination cannot be achieved purely sequentially but involves some degree of iteration because of interaction between the abovementioned processes.

At the end of the atmospheric correction procedure data, usually called "level 2" in contrast to the "level 1 top-of-atmosphere data, is available consisting typically of water-leaving reflectance for a number of spectral bands as well as some atmospheric parameters such as aerosol optical thickness calculated during atmospheric correction. These data may be accompanied by a number of processing "flags" which are set equal to one or zero for each pixel and denote whether special conditions were detected during processing. An example of the flags provided with SeaWiFS data is given in Table 11.

Number	Flag Name	Description
1	ATMFAIL	Atmospheric correction failure
2	LAND	Land
3	BADANC	Missing ancillary data
4	HIGLINT	Sun glint contamination
5	HILT	High radiance (less sensitivity)
6	HISATZEN	High satellite zenith angle
7	COASTZ	Shallow water
8	NEGLW	Negative water-leaving radiance (any band)
9	STRAYLIGHT	Stray light contamination
10	CLDICE	Clouds or ice
11	COCCOLITH	Coccolithophore
12	TURBIDW	Turbid water
13	HISOLZEN	High solar zenith angle
14	HITAU	High aerosol concentration
15	LOWLW	Low water-leaving radiance
16	CHLFAIL	Chlorophyll algorithm failure
17	NAVWARN	Questionable navigation
18	ABSAER	Absorbing aerosols
19	TRICHO	Trichodesmium bloom
20	MAXAERITER	Aerosol algorithm reached maximum iteration
21	MODGLINT	Corrected for sun glint
22	CHLWARN	Chlorophyll value out of range
23	ATMWARN	Aerosol type is outside reasonable range
24	DARKPIXEL	Rayleigh-corrected radiance is negative (any band)

>> Table 11. Quality and processing flags supplied with level 2 SeaWiFS imagery. Each pixel of radiometric data is accompanied by a 24-bit pixel for which each bit is set to one or zero according to the corresponding flag.

Because of the difficulty and importance of the atmospheric correction for water applications it is essential that the user of satellite data assess the quality of the level 2 data before use. The importance of this quality control cannot be understated: satellite imagery of lakes and seas gives very detailed information and often beautiful pictures, but in many cases the information can be completely erroneous because of atmospheric correction problems!

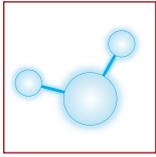
Quality assessment consists of a number of processes:

1. Use of processing flags: the processing flags provided with level 2 data contain valuable information on data quality. Many flags indicate that data should not be used in any circumstances: for example any data for which land, cloud, atmospheric correction failure or similar flags are raised (set equal to one) should obviously be discarded or "masked" by the user. Other flags may provide more subtle warnings of potential



problems or special circumstances that may lead to rejection of data in certain cases but acceptance in others. Flags are usually provided by satellite data providers but must be inspected by the remote sensing user.

2. Subjective analysis or "verification" of imagery. Are there parts of the image which seem to have unrealistic data? The user should be especially suspicious if shapes that appear in the water seem to be correlated with cloud-like structures (visible on top-of-atmosphere imagery but not always accurately detected by automated algorithms) or with regular geometric patterns caused by sensor deficiencies (striping, banding, etc.).
3. Dedicated validation campaigns as outlined in Section 9.2.5.



## 9 Data analysis and validation

### 9.1 Land

Most of the data analysis and validation techniques described in this section are ENVI® build-in algorithms. For more information the reader is referred to the ENVI® User's Guide.

#### 9.1.1 MINIMUM NOISE FRACTION, PIXEL PURITY INDEX, ENDMEMBER SELECTION

The high spectral and spatial resolution intrinsic to imaging spectroscopy, has one important drawback: the imaging spectrometers deliver huge quantities of data. However, much of the spectral data in the datasets is redundant. The selection of a small number of relevant spectral bands without loss of essential information for a given application is therefore a critical issue in any imaging spectroscopy application. The **Minimum Noise Fraction (MNF)** Transform segregates the spectral bands that are dominated by noise from the bands that contain important information contributing to the overall variance in the dataset. The MNF reduces the dimensionality of the dataset and retains a small number of noise-free components. Consequently the computational requirements for subsequent processing is reduced (Boardman and Kruse, 1994).

The MNF transform as given in Green et al. (1988) is in essence a two-step Principle Components Analysis (PCA). The first step calculates a noise covariance matrix and decorrelates and rescales the noise in the data. The second step is a standard principle components transform where the transformed spectral bands are ranked by decreasing variance. More detailed information on PCA can be found in Richards (1999).

The output of the MNF transform is an image cube of  $n$  MNF bands. The output MNF bands are ordered by decreasing signal-to-noise ratio. The low-order components have the highest information content, while most of the noise is concentrated in the higher-order bands (Figure 46). The inherent dimensionality can be evaluated by examination of the associated images. In the higher order bands surface features are no longer visible and the image is dominated by noise.

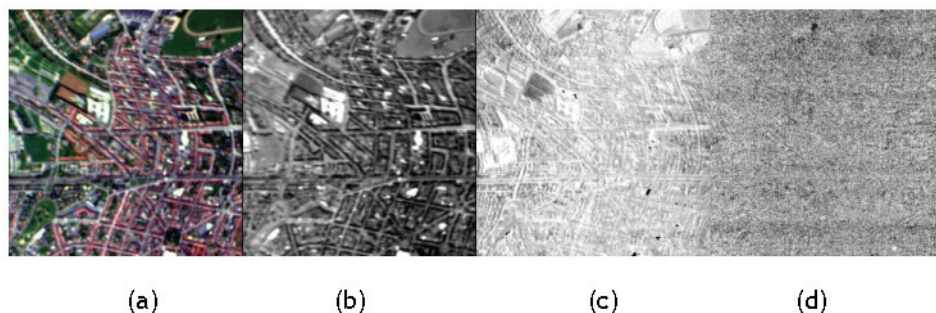


>> Figure 46: The MNF transform: (a) RGB display of original input image (96 spectral bands), (b) MNF band 2, (c) MNF band 8 and (d) MNF band 30.

An other approach to evaluate the cut off region between signal and noise is to examine the plot of the eigenvalues (Figure 47). Eigenvalues for MNF bands that contain information will be an order of magnitude larger than those containing noise only. The noise-dominated bands have near-unity eigenvalues. Generally most information is concentrated in the lower order MNF bands, but rare spectra may be found in the noisier MNF bands.

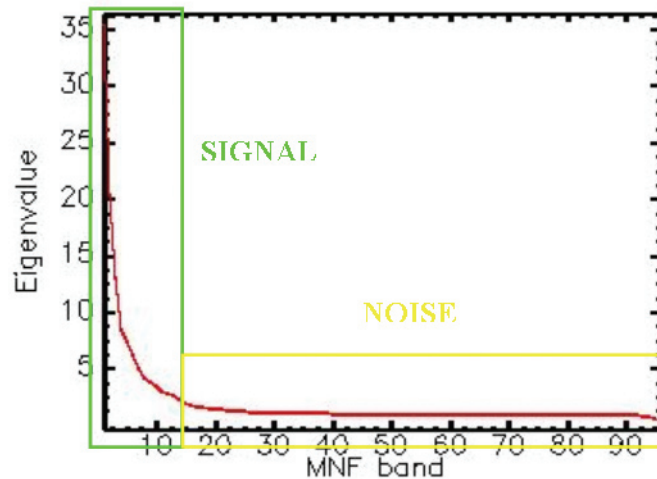
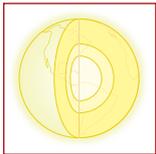


>> Figure 47: Plot of eigenvalues versus MNF output band showing approximate signal to noise cut-off.

The decreasing eigenvalue with increasing MNF band shows how noise is segregated in the higher-order MNF bands. As the curve approaches 1, one can assume that those bands are dominated by noise and do not contribute to the overall image variance. The information is concentrated in only a few low-order MNF bands

The **Pixel Purity Index (PPI)** is a technique to determine **endmembers**. Endmembers are pixels which are spectrally very pure or unique. Ideally an endmember should represent a single pure material. However pure pixels of each member are often not present in the image.

Due to the large amount of data, PPI is usually performed on MNF transformed data. If the image spectra are plotted in a  $n$ -dimensional space, the 'pure' pixels correspond to the corners (i.e. simplex vertices) of the multi-dimensional cloud of data points (Boardman, 1993). The PPI procedure automatically finds the extreme spectra along the margins of the  $n$ -dimensional space by continually projecting  $n$ -dimensional scatter plots onto a random unit vector (Figure 48). The extreme pixels for each projection are recorded and the total number of times each pixel is marked as extreme, is stored into an image. The higher values indicate pixels that are nearer to extremities of the  $n$ -dimensional data cloud, and thus are relatively purer than pixels with lower values. Pixels with values of zero were never found to be extreme. Pixels with high scores in the resulting PPI image are therefore excellent candidates to select as endmembers for subsequent processing.

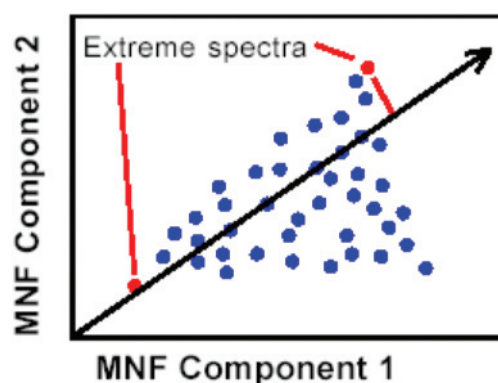


>> Figure 48: Single two-MNF component plot showing how the Pixel Purity Index determines potential extreme or pure image pixels. (Source: <http://www.microimages.com/getstart/pdf/hyprspec.pdf>).

### 9.1.2 DISCRETE WAVELET TRANSFORM

The most widely used (real-valued) signals are time–amplitude representations in the case of one dimension (Figure 49). For two dimensional (grey-scale) images we obtain a space–amplitude signal, i.e. each pixel at location  $(x,y)$  corresponds to some value (amplitude). Hyperspectral images are three dimensional in the sense that each pixel corresponds to  $N$  values, with  $N$  the number of bands. For this discussion, we will concentrate on one dimensional (1-D) signals, obtained by the  $N$  values of a particular hyperspectral pixel.

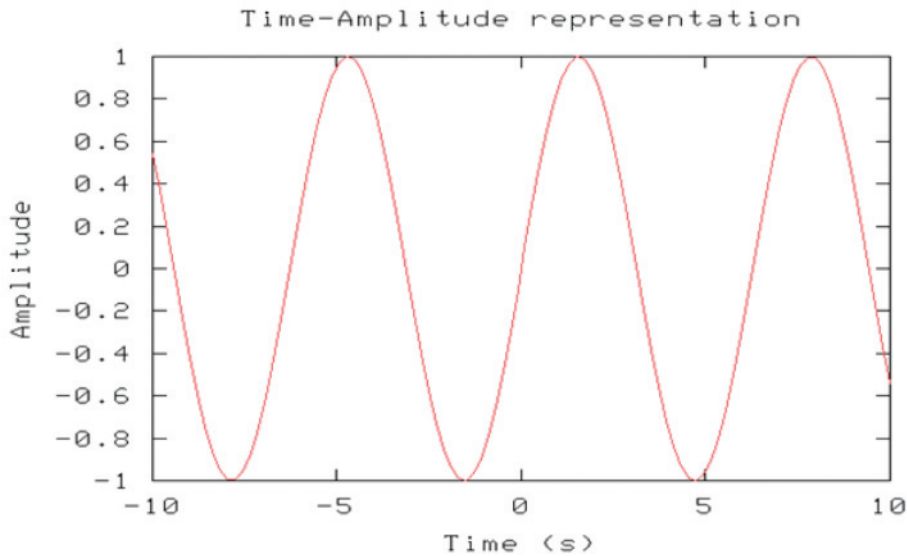


>> Figure 49: Example of a one dimensional signal (amplitude vs. time).

The same 1-D signal from Figure 49 can be represented in the Fourier domain, by transforming the time-amplitude into a frequency-amplitude representation. The Fourier transform  $X(f)$  of a signal  $f(t)$  gives us the information whether a certain frequency component exists (represented by its amplitude). Frequency representations are highly valuable for analysing the behaviour of signals. The presence of high frequency components corresponds to highly fluctuating signals, whereas signals with low frequencies are only "slowly" varying. Typical noise for example contains high frequencies, with no zero frequency. The zero frequency component corresponds to the mean value of the signal and is often referred to as the DC (Direct Current) component. The frequency domain for representing signals is very useful when using filtering techniques. Low pass filters remove high frequency components, which is often used for reducing noise. High pass filters can be used for detecting abrupt changes in a signal (edge detection).

The Fourier transform is independent where exactly in time the frequency component appears This explains the popularity of the Fourier transforms for stationary signals<sup>1</sup>. Most practical signals however are not stationary.

When we are interested at which location in time a frequency component appears, we can use the Discrete Wavelet Transform (DWT). However, in accordance with the principle of the Heisenberg uncertainty<sup>2</sup>, we are unable to know the exact time-frequency information (what spectral component exists at what instance of time). We can only know a time interval in which a certain band of frequencies occurs. Using the Fourier transform, we know the exact spectral component that occurs, but without any information about the point in time when it occurs.

The Wavelet Transform is a function of translation and scaling and it depends on the choice of a mother wavelet. The translation parameter gives us information about the time in which a frequency component occurs, whereas the scaling is inversely proportional to the frequency (scale=1/frequency)

The mother wavelet is used as the base function to represent the original function  $f(t)$  in the time domain, similar to the cosine function used in the Fourier transform. Using scaled versions of this mother wavelet allows us to analyse different frequency components of the function  $f(t)$ . An important property of the mother wavelet is its finite extent in time. This is a crucial difference with the infinite cosine function used for the Fourier transform which extends from  $t=-\infty$  to  $t=+\infty$ . Translating this finite function in time focuses on the original function  $f(t)$  within a specific time window.

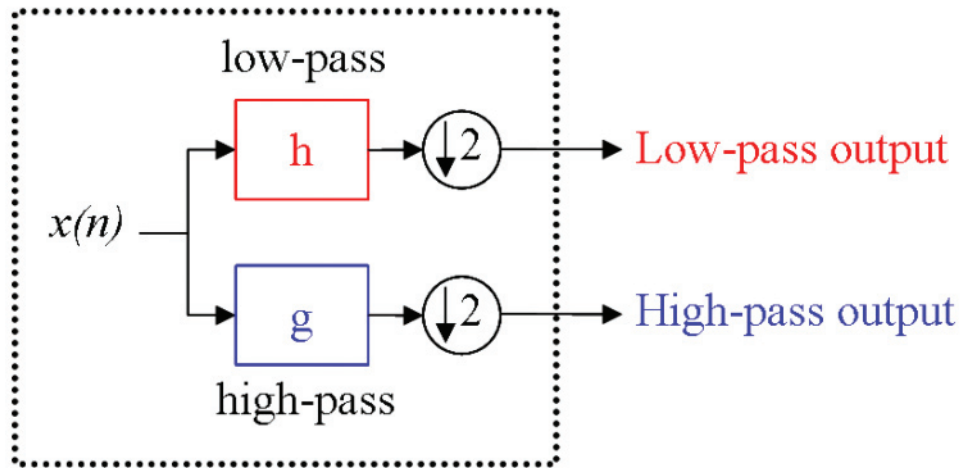


>> Figure 50: Low-pass (h) and high-pass (g) filter, followed by down sampling with factor 2.

In practice, multi-resolution analysis is carried out using 2 channel filter banks composed of a low-pass (h) and a high-pass (g) filter and each filter bank is then sampled at a half rate (down sampling with factor 2) of the previous frequency (Mallat, 1998). Notice that in Figure 50, the original function  $f(t)$  is replaced by  $x(n)$ . Instead of 1-D signals in time, we are interested in spectral signatures. In this case, the discrete parameter  $n$  indicates the band number of the hyperspectral sensor. By repeating this procedure, it is possible to obtain the wavelet transform at any scale (Figure 51).

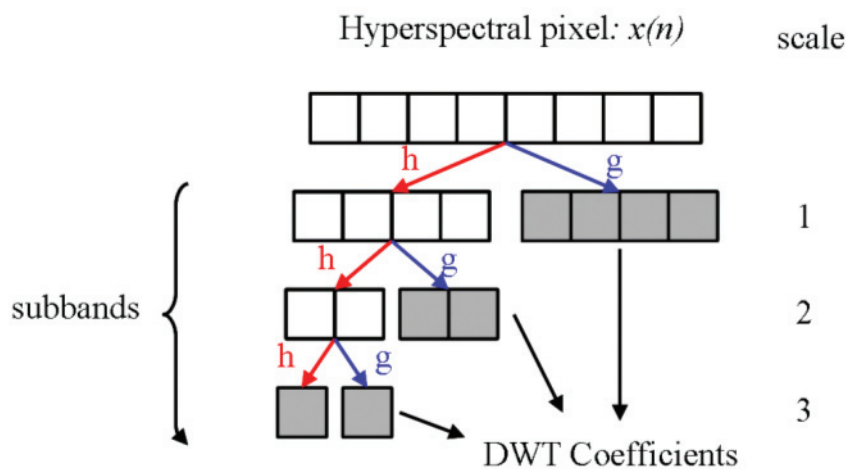


>> Figure 51: Analysis Filter Bank computing the Discrete Wavelet Transform.

Hence, the discrete wavelet transform gives a complete representation of the spectrum by recursively filtering the signal with a low and high pass filter and subsequently subsampling it. Each time the high pass filtered part is retained in the detail coefficients, and the recursion is continued with the low pass signal. This transform separates local details at different resolutions into different features. Those features can later be used for the classification task. In Figure 52, a typical vegetation signature and its derived DWT coefficients are shown. It is clear that the small difference between similar signatures (blue and red curves) are better visible in some scales than in others. Scale 1 corresponds to the highest frequency and a full resolution (1 nm). A scale of 9 corresponds to the mean (DC) value.

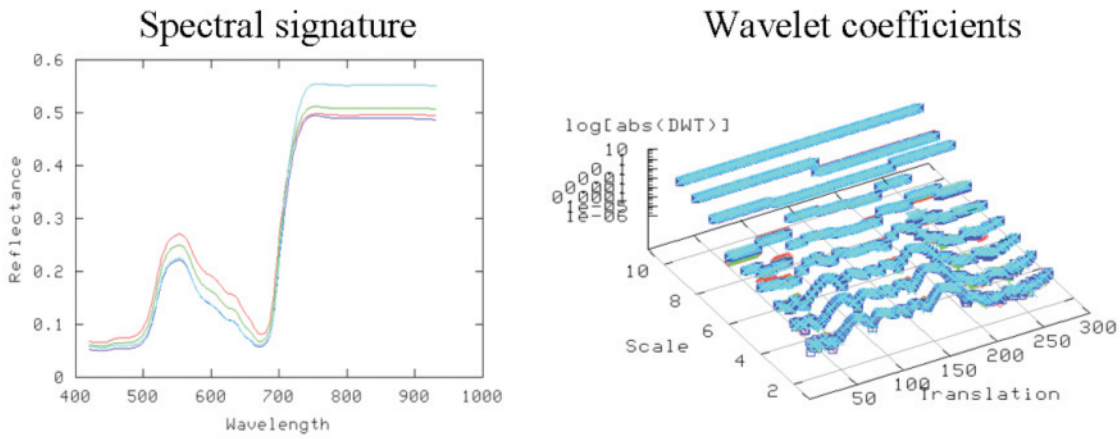
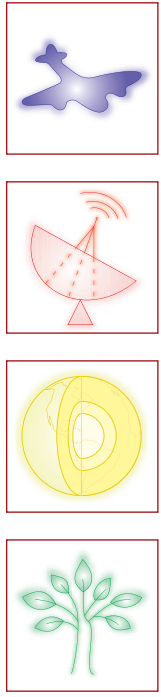
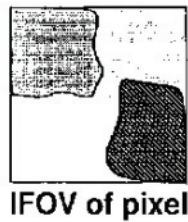


>> Figure 52: Typical vegetation signature in spectral domain (left) and its derived DWT coefficients (right).

### 9.1.3 ABUNDANCE TECHNIQUES

#### 9.1.3.1 Linear Spectral Unmixing

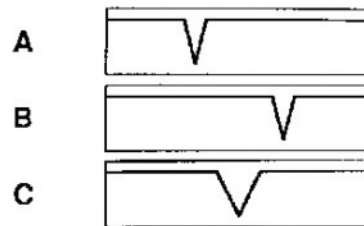
Linear Spectral Unmixing is a technique to determine the relative abundances of materials based on the material's reflectance spectrum (endmember spectrum). The technique assumes that the reflectance spectrum of a pixel is the linear combination of the reflectance spectra of the composing elements (endmembers) present in the pixel. For this technique all endmembers should be known. The result of spectral unmixing is a series of Mean and RMS gray-scale images, one Mean and RMS image for each endmember. High Mean values (bright) indicate high abundance values. The results are highly dependent on the endmembers used. The error on the unmixing process can be determined using the RMS image. Bright RMS values indicate large errors. Figure 53 illustrates the linear spectral unmixing principle.



a single pixel with three materials: A B and C

material	fraction
A	0.25
B	0.25
C	0.50

each endmember has a unique spectrum



the mixed spectrum is just a weighted average

$$\text{mix} = 0.25 \cdot A + 0.25 \cdot B + 0.5 \cdot C$$

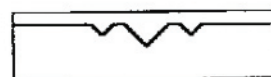


>> Figure 53: The linear spectral unmixing principle. (Source: [www.ltid.inpe.br/tutorial/images/tut14.htm](http://www.ltid.inpe.br/tutorial/images/tut14.htm))

For this technique all the endmembers should be known which is not always the case. If not all endmembers are known or if only the abundance of a few endmembers should be mapped, Matched Filtering or Mixture Tuned Matched Filtering performs better. These techniques are described in the next section.

### 9.1.3.2 Mixture Tuned Matched Filtering

Matched Filtering is a technique based on MNF images (Section 9.1.1) and is used to determine abundances of some of the endmembers. With this technique knowledge of all endmembers is not required. All materials you are not interested in can be regarded as background. The result of Matched Filtering is a series of gray-scale images, one for each endmember. The values represent the relative degree of match. A value of 1 is a perfect match. Mixture Tuned Matched Filtering is a technique to reduce the number of false positives that are sometimes found with Matched Filtering. Mixture Tuned Matched Filtering adds an Infeasibility Image for each endmember. Pixels with high Infeasibility values are likely to be matched false positives. Correctly matched pixels have a high Matched Filter score and a low Infeasibility score. Infeasibility values are expressed in sigma noise units which vary in DN (digital numbers) scale with matched filter score. A 2-D scatter plot is a means to identify pixels with high Mean score and low Infeasibility score.

For more background information the interested reader is referred to Boardman et al., 1995; Chen et al., 1987; Harsanyi et al., 1994 and Stocker et al., 1990.

### 9.1.3.3 Spectral Feature Fitting

Spectral Feature Fitting™ (SFF™) is a method for comparing absorption features (after normalising the spectra using a technique called continuum removal, see also Section 11.2.2) of image spectra and reference spectra using a least-squares technique. For each reference spectrum a Scale image and a Root Mean Square (RMS) image is created. The Scale value is a measure of absorption feature depth which is related to material abundance. The brighter Scale pixels indicate a better match to the reference spectrum (at least for pixels with a low RMS value). Dark RMS pixels indicate a low RMS error. A very useful instrument to select the pixels that best match a reference material (characterised by a high Scale value and a low RMS value) is a 2-D scatter plot of Scale versus RMS.

## 9.1.4 CLASSIFICATION TECHNIQUES

### 9.1.4.1 Spectral Angle Mapper

The standard Spectral Angle Mapper (SAM) is an ENVI® build-in classification algorithm that aims at assigning a class to each pixel of the image.

Spectral Angle Mapper (SAM) is a spectrally-based classification technique that uses the N-dimensional (N is the number of spectral bands) angle to compare a target spectrum with a reference.

The reflectance spectrum of each individual target pixel can be described as a vector in a n-dimensional space, where n is the number of spectral bands. The coordinates of the vector are the n reflectance values of the target pixel. Each vector is characterised by a certain length and direction. The length of the vector represents the brightness of the pixel while the direction represents its spectral features. Variation in illumination mainly affects the length of the vector, while spectral variability between different spectra affects the angle between their corresponding vectors (Kruse et al., 1993).

Figure 54 depicts a pair of three-dimensional spectra and indicates the Spectral Angle,  $\theta$ , between both spectra. Spectrally similar pixels will be characterized by a small  $\theta$  angle. The spectral angle is calculated according to the formula below and can vary between 0 and  $\pi/2$ .

$$\theta = \cos^{-1} \left( \frac{\sum_{i=1}^n t_i r_i}{\sqrt{\sum_{i=1}^n t_i^2 \sum_{i=1}^n r_i^2}} \right) \quad (9.1)$$

with n the numbers of spectral bands, t the target spectrum and r the reference spectrum.

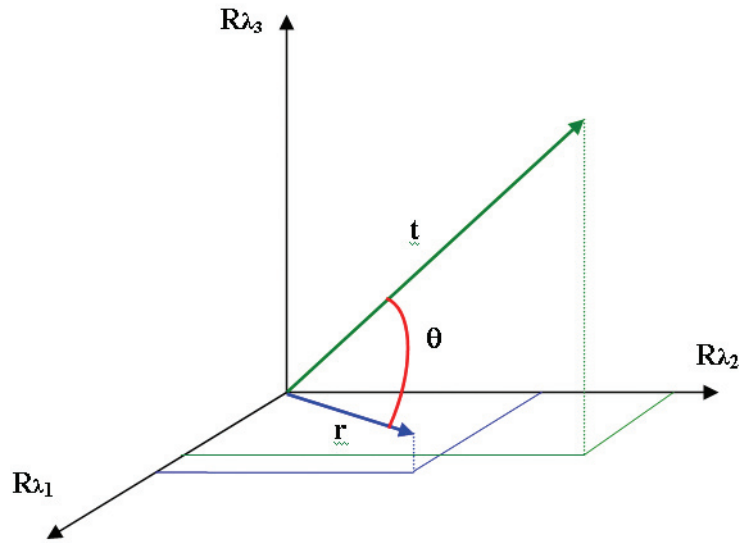
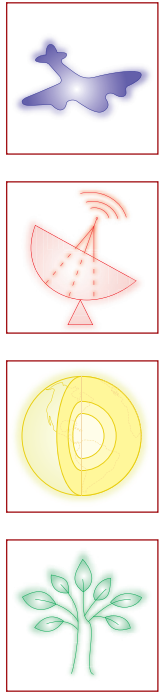


>> Figure 54: Visualization of the Spectral Angle,  $\theta$ , between two 3-D reflectance spectra,  $t$  = target spectrum,  $r$  = reference spectrum, using the reflectance at spectral bands  $\lambda_1, \lambda_2, \lambda_3$ .

The reference spectra used for material identification can either be derived from spectral libraries or can be collected from the image using Regions Of Interest (ROI). SAM is based on a linear architecture, using every available band and each reference spectrum as depicted in Figure 55. For every image pixel, the comparator selects one class based on the smallest Spectral Angle,  $\theta$ , calculated between the image target spectrum  $t$  and all reference spectra  $r_x$ . Each pixel will be assigned to a reference spectrum (class) according to the lowest spectral angle value.

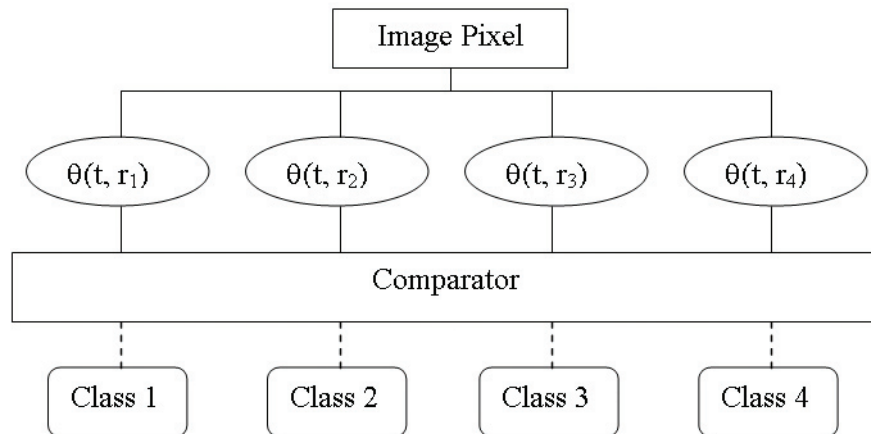


>> Figure 55: Class assignment in SAM.

### 9.1.4.2 Fisher's Linear Discriminant

Linear discriminant analysis (LDA) (Duda, 2001), also called Fisher's discriminant analysis, looks for optimal projections optimising the class separability. It assumes that  $c$  different classes can be described as normal distributions with equal covariance matrices. Although relying on heavy assumptions that are not true in many applications, Fisher's linear discriminant has proven to be very powerful. One reason is certainly that a linear model is rather robust against noise and most likely does not overfit<sup>3</sup>.

For  $c$  classes, LDA projects the feature space onto  $c-1$  dimensions, maximising the Fisher criterion:

$$J(w) = \frac{|W^T S_B W|}{|W^T S_W W|} \tag{9.2}$$

where  $W$  denotes the projection matrix,  $S_B$  is the between class scatter matrix and  $S_W$  is the within class scatter matrix:

$$S_B = \sum_{i=1}^c n_i (\bar{\mu}_i - \bar{\mu})(\bar{\mu}_i - \bar{\mu})^t \tag{9.3}$$

$$S_W = \sum_{i=1}^c \sum_{j=1}^{n_i} n_i (\bar{x}_{ij} - \bar{\mu}_i)(\bar{x}_{ij} - \bar{\mu}_i)^t, \tag{9.4}$$

with  $n_i$  the number of elements in class  $i$ ,  $\bar{x}_{ij}$  the  $j$ -th point in class  $i$ ,  $\bar{\mu}_i$  the mean vector of class  $i$  and  $\bar{\mu}$  the mean vector of all points. The optimal  $W$  can be found by solving the generalised eigenvalue problem

$$S_B \bar{w}_i = \lambda_i S_W \bar{w}_i. \tag{9.5}$$

The optimal  $W$  consists of the eigenvectors associated with the  $c-1$  largest eigenvalues.

In the special case of two classes (Figure 56), the vector  $\bar{w}$  that maximizes the Fisher criterion, is immediately obtained from

$$\bar{w} = S_W^{-1} (\bar{\mu}_1 - \bar{\mu}_2). \tag{9.6}$$

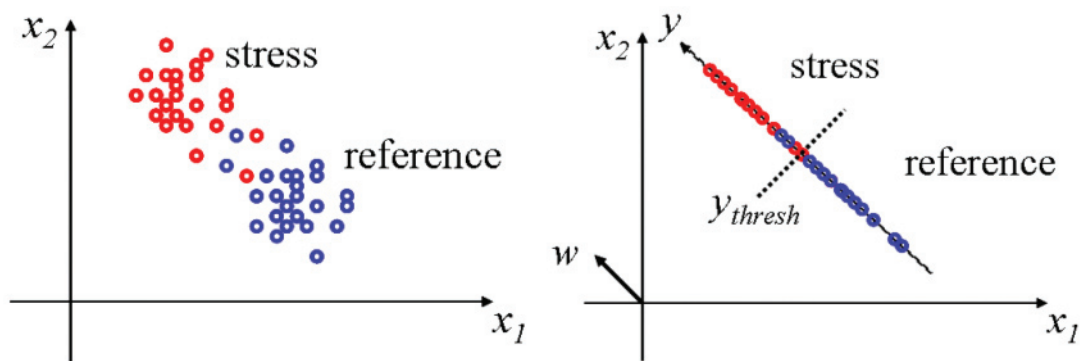


>> Figure 56: LDA, special case of two classes (red and blue) in two dimensions. The optimal projection vector  $w$  is shown at the right.

### 9.1.5 ACCURACY ASSESSMENT

Two methods to determine the accuracy of the classification outcome are described.

#### 9.1.5.1 Confusion matrix

A confusion matrix ( $n \times n$ , with  $n$  the number of classes, the ground truth classes are represented as columns, the image classes as rows) is used to compare the classification result with ground truth information. In order not to bias the accuracy assessment, the ground truth pixels should be selected randomly. From the confusion matrix an **overall accuracy, producer and user accuracy, Kappa coefficient** and **errors of commission and omission** can be calculated.

The **overall accuracy** is the sum of the number of pixels classified correctly divided by the total number of pixels in all the ground truth classes.

The **Kappa coefficient** (KHAT) represents the proportional reduction in error generated by a classification process compared to the error of a completely random classification and is calculated as follows (Congalton, 1991):

with

$r$  = the number of classes in the confusion matrix

$x_{ii}$  = the number of observations in row  $i$  and column  $i$

$x_{i+}$  = the marginal total of row  $i$

$x_{+i}$  = the marginal total of column  $i$

$N$  = the total number of observations in the matrix

The **error of omission** is calculated as the number of ground truth pixels classified incorrectly divided by the total number of pixels in the ground truth class.

The **error of commission** is calculated as the number of pixels of a given class but classified incorrectly divided by the total number of pixels in the ground truth class.

The **producer's accuracy** is a measure indicating the probability that a pixel is labelled into a certain class given that the pixel belongs to that ground truth class or the probability that a pixel classified to a given class is correctly identified on the map.

The **user's accuracy** is a measure indicating the probability that a pixel is in a certain class given that the pixel is labelled into this class or the probability that the pixel will appear on the ground as it is classified.

For further reading, see Congalton, 1991.

### 9.1.5.2 Leave-one-out

Leave-one-out is an alternative method to estimate the accuracy of a classifier. Assume the classifier uses  $N$  training pixels. To estimate the accuracy one training pixel is removed and the classification is performed with  $N-1$  training pixels. If the removed pixel is classified correctly, one point is attributed. This procedure will be repeated until each training pixel is removed once and the points will be summed. This summed points divided by the total number of training pixels is a measure of the accuracy of the classifier.

## 9.2 Water data analysis and quality control

This section describes how atmospherically-corrected data (see Section 8.2) in the form of water-leaving reflectance spectra are analysed for typical aquatic applications. For certain applications it may be sufficient to plot reflectance imagery for a simple visual analysis or to classify imagery according to areas of high turbidity, algae blooms, etc. However, in general a quantitative estimation of water quality parameters such as chlorophyll *a* or total suspended matter concentration is required. The design of algorithms for such parameters is a matter of ongoing research and is beyond the scope of the present source. A very brief summary is given here and the reader is referred to the various references for further reading.

### 9.2.1 CHLOROPHYLL A CONCENTRATION USING BLUE-GREEN RATIOS

Phytoplankton, the microscopic plant life that make up the base of the aquatic food chain, is commonly represented by the concentration of chlorophyll *a*, a photosynthetic pigment (Kirk, 1996). Because chlorophylls and other pigments absorb light for photosynthesis their presence changes the colour of water. While absorption spectra may vary according to species, in general phytoplankton absorb most strongly blue light for wavelengths between 400 nm and 490 nm. Water molecules themselves absorb very strongly red light. As a result if phytoplankton is the only substance affecting water colour then colour will vary from blue for water with little or no phytoplankton to green for water with high phytoplankton abundance. This is the so-called "Case 1" according to the optical classification proposed by (Morel, 1977). In such conditions chlorophyll *a* concentration is generally estimated by using the ratio(s) of water-leaving reflectance at two or more bands in the blue-green spectral region.

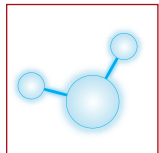
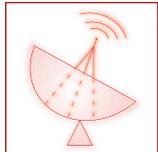
For example, the MERIS case 1 water algal pigment index product (Morel and Antoine, 2000), represented here by  $C$  and similar to chlorophyll concentration, is defined via:

$$\log_{10} C = \sum_{x=0}^m A_m (\log_{10} \rho_{443,555})^x \quad (9.7)$$

where

$$\rho_{443,555} = \frac{\rho_w(443nm)}{\rho_w(555nm)} \quad (9.8)$$

$\rho_w(\lambda)$  is the water-leaving reflectance at wavelength  $\lambda$ , and  $A_m$  is a set of empirical coefficients. A number of similar band ratio algorithms are reviewed by (O'Reilly, 1998).



### 9.2.2 CHLOROPHYLL A CONCENTRATION USING RED AND NEAR-INFRARED RATIOS

For water with high absorption in the blue-green spectral region because of non-algae particles or coloured dissolved organic matter (CDOM) the algorithms of Section 9.2.1 give erroneous estimations of chlorophyll *a* concentration. This is the so-called "Case 2", which in reality covers a wide range of cases or optical conditions. For highly reflective waters with high concentrations of suspended particles it may be possible to measure remotely reflectances in the red and near-infrared spectral range. In such cases the absorption by chlorophyll of red light with wavelength near 665 nm can be used. For example, (Gons et al, 2005) defined such an algorithm for MERIS by:

$$C = \frac{1}{0.016} \left( \frac{\rho_w(708nm)}{\rho_w(664nm)} [0.70 + b_b] - 0.40 - b_b^{1.06} \right) \quad (9.9)$$

where  $b_b$  is an estimate of the backscatter coefficient given by:

$$b_b = \frac{1.61\rho_w(778nm)}{0.082 - 0.6\rho_w(778nm)} \quad (9.10)$$

Such algorithms require high quality measurements of water-leaving reflectance in the red and near-infrared (not easy to achieve!) and generally work well only for high chlorophyll *a* concentrations, e.g. greater than 5 mg m<sup>-3</sup>.

### 9.2.3 CHLOROPHYLL A RETRIEVAL FROM MULTI-BAND ALGORITHMS

More complex and potentially more general methods are available for estimating chlorophyll *a* by fitting the full water-leaving reflectance spectrum to an optical model. The interested reader is referred to the references in (Ruddick et al., 2005) for more information.

### 9.2.4 TOTAL SUSPENDED MATTER

Total suspended matter (TSM) concentration is a commonly used parameter to represent the suspended particle load of a water body. This may be of interest for applications relating to sediment transport, and geomorphology (beach, sandbank erosion/deposition), dredging, water transparency (diving, biological productivity, subsurface military object detection), etc. Particles in suspension, i.e. present in the water because of turbulence, buoyancy or a local discharge, reflect light and their presence can often be seen even without complex image processing. For example, looking from a boat or an airplane it is often easy to spot areas of high TSM, which are much browner than surrounding water and are often marked by sharp "fronts", lines in the water where colour and other water parameters change abruptly as in . Because reflectance is approximately proportional to TSM for low to medium reflectances it is possible to use simple one band algorithms for estimation such as that proposed by (Nechad et al., 2003) for estimating TSM (in g m<sup>-3</sup>), denoted by  $T$ , from SeaWiFS:

$$T = 360.26 * \frac{\rho_w(765nm)}{0.187 - \rho_w(765nm)} + 4.16 \quad (9.11)$$

Many other algorithms exist for TSM, including multi-band spectral fitting algorithms and it is not possible to summarise all such approaches here. The interested reader is referred to (Dekker et al., 2001; Doxaran et al., 2002; Ouillon et al., 1997; Stumpf and Pennock, 1989) for more information.

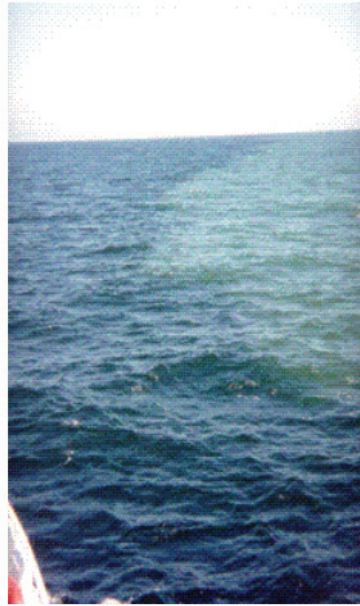
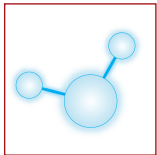


>> Figure 57: A coastal water front marking an abrupt change in water colour because of a change in total suspended matter concentration. Other parameters such as salinity, temperature, etc. often change abruptly at such fronts.

### 9.2.5 QUALITY ASSESSMENT

The assessment of the quality of remotely sensed products is composed of many steps. Firstly, satellite data products from the major space agencies such as NASA and ESA are generally supported by extensive calibration and validation programmes to assess the radiometric quality of the sensor and the derived products respectively. Sensors are carefully analysed before launch to provide a nominal pre-launch calibration. Calibration can be monitored during flight using on-board targets of known reflectance, generally nearly 100% reflective and near-perfectly diffuse plaques, which can be oriented to reflect the sun. Finally in-flight calibration can be monitored by comparing satellite measurements of stable ground targets, such as deserts or clear water, with corresponding ground reflectance measurements supplemented by atmospheric measurements. This is commonly called "vicarious" calibration. A well-documented example of ocean colour sensor calibration and validation is provided by the publicly available SeaWiFS Postlaunch technical Report Series ([http://oceancolor.gsfc.nasa.gov/cgi/postlaunch\\_tech\\_memo.pl](http://oceancolor.gsfc.nasa.gov/cgi/postlaunch_tech_memo.pl)).

Secondly, satellite data products from NASA and ESA are supplemented with a number of pixel-based quality and processing flags as described in Section 8.2.3. These are particularly useful for warning of problems in atmospheric correction.

Thirdly, since the quality and processing flags usually supplied with data are never perfect it is important to supplement this objective automated quality assessment with a subjective analysis of imagery by an experienced scientist, preferably one with understanding both of remote sensing and of the oceanography/limnology of the region under study. This allows detection of clearly unreasonable data which has passed the objective quality analysis. A typical example is erroneously high chlorophyll *a* concentrations caused by application of an inappropriate algorithm, such as a case 1 blue-green algorithms in areas of turbid water with many non-algae particles.

Finally, for a higher level of confidence it is important to carry out field measurement campaigns for the region of interest simultaneously with satellite overpass to enable a direct comparison of satellite data products for chlorophyll *a* or TSM concentration with conventional in-situ measurements. Such campaigns require great care because of the high accuracy requirements and are generally complicated by the requirement for a high degree of simultaneity, e.g. a one hour time difference is generally considered as the limit for coastal water validation measurements. Sample protocols are provided for such measurements in the detailed NASA/SeaWiFS protocol documents available online (Mueller et al., 2003).



## **10 Water**

### **10.1 Spectral properties of water bodies**

Most aquatic applications of optical remote sensing are based on mapping of optically-active water quality parameters such as chlorophyll *a* and total suspended matter concentration. To understand how these parameters affect water colour and hence can be remotely detected this section gives a brief summary of the spectral properties of water bodies and provides a simple model of water colour. This theory will be illustrated in the outdoor exercise of HyperTeach Hands-on Lesson 3 and the simple model will be provided for the exercises of HyperTeach Hands-on Lesson 3.

#### **10.1.1 INTRODUCTION: WATER AND ITS COLOURED CONSTITUENTS**

The colour of water is affected by certain constituents including: pure water molecules themselves (which absorb strongly red and near-infrared light), algae including free-floating often microscopic phytoplankton (which absorb light via various photosynthetic pigments and also scatter light), non-algae particles of mineral (e.g. resuspended bottom sediments or river sediments) or organic detrital nature, and coloured dissolved organic matter (CDOM) which results from degradation of plant-life either on land (which reaches rivers, lakes and the sea via groundwater) or in the water itself. Since these constituents affect the colour of the water it is possible in suitable circumstances to detect their presence in water and quantify their respective concentrations.

#### **10.1.2 APPLICATIONS, PARAMETERS AND LIMITATIONS**

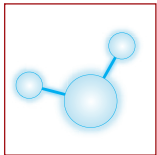
As a consequence of the water constituents which influence water colour, optical remote sensing of water bodies is generally aimed at the quantification and mapping of one or more of the following key parameters:

- Chlorophyll-*a* concentration (as a proxy for phytoplankton in general) with typical units "µg/l" or equivalently "mg/m<sup>3</sup>".
- Total suspended matter, also called "suspended particulate matter" or, if algae particle are removed, "non-algae particle" concentrations, with typical units "g/m<sup>3</sup>".
- Coloured dissolved organic matter absorption, typically expressed as an absorption coefficient for a reference wavelength.
- Water transparency, generally expressed as a Secchi depth (with units of m) or as a more rigorously-defined diffuse attenuation coefficient at a reference wavelength or over the range of wavelengths contributing to Photosynthetically Available Radiation (PAR).
- Water bottom substrate and water depth (though the latter is not normally well-measured by passive optical remote sensing as covered by the present course and the former is for many water bodies not visible).

In certain applications products related to or derived from these key parameters may be targeted such as primary production (the rate at which inorganic carbon is fixed by photosynthesis), certain harmful phytoplankton species, benthic (bottom) vegetation type, etc. Finally some applications may require a simple qualitative detection or classification of features, such as oceanic fronts or water masses, seagrass beds or coral, though most aquatic applications aim for a quantification of substances via a volume (or for bottom characteristics surface) concentration.

Aquatic applications for which optical remote sensing can be a useful tool include:

- Assessment of the global carbon cycle
- Monitoring of eutrophication (excessive production of algae related to high nutrient supply, often of human origin) in coastal and inland waters and/or detection of harmful algae blooms
- Support for sediment transport investigations, usually in combination with modelling and in-situ monitoring, relating to, for example, coastal erosion/deposition, dredging, coastal engineering works, etc.
- Support for oceanographic or limnological investigations, particularly relating to aquatic biology or to water masses
- Mapping of special aquatic habitats such as seagrass beds or corals
- Military activities including submarine and mine detection
- Professional and leisure diving activities



It is important to note the limitation that optical remote sensing using the sun as light source (passive remote sensing) can provide information only regarding the surface layer of water where a reasonable proportion of photons scattered by particles or molecules may subsequently exit the water body and potentially be picked up by a remote sensor. The depth of this surface layer depends on wavelength and water composition. As a very rough guide one can think of the Secchi depth (the depth at which a white disk disappears from view as will be demonstrated in Lesson 3) as an indication of the depth of this surface layer and as examples, the Secchi depth can reach tens of meters in the clearest blue oceanic waters, has values of a few metres in turbid coastal waters such as Belgian North Sea waters but can be as small as a few centimetres (or even less) in the most heavily sediment-loaded river waters. To be more precise a remote sensor will receive information from different depths according to an exponentially decreasing weighting where the rapidity of exponential decrease of this weighting is determined by a suitable defined wavelength-dependent attenuation coefficient. In general, the corresponding depth for red and near-infrared light will be much less than for blue light because of strong absorption of red and near-infrared light by pure water molecules. As any diver will tell you, the water looks very blue at anything more than a few metres depth.

Because of this limitation it becomes very difficult if not impossible to detect or quantify by optical remote sensing features which are more than a few metres below the surface and especially if their depth is also an unknown parameter. Examples include the subsurface chlorophyll maxima commonly found in stratified waters with surface nutrient depletion or, in general, sea bottom properties in regions where the sea bottom is not visible at the surface.

### 10.2 *A simple model of water colour*

#### 10.2.1 REFLECTANCE DEFINITION AND ASSUMPTIONS

In this section a simple model, the "HYPERTEACH ocean colour model", will be described to explain how the colour of water is affected by its constituents. This model is made available to students in the form of an Excel spreadsheet and will be demonstrated practically in the hands-on exercises of Lesson 3.

Optical remote sensing of water colour is generally based on the bottom-of-atmosphere (BOA) or "surface" or water-leaving reflectance spectra. In research publications many alternative definitions are provided for reflectance with consequent confusion of terminology and the need to define carefully in each study how the reflectance is calculated, particularly whether it is an above-water or below-water quantity (very different in magnitude because of refraction at the air-water interface) and whether it is calculated from (directional) radiance or hemispherical irradiance quantities. In the present text the terminology of water-leaving radiance reflectance is adopted, corresponding to the standard MERIS reflectance product. This is defined as

$$\rho_w^{0+}(\lambda) = \frac{\pi L_w^{0+}}{E_d^{0+}} \quad (10.1)$$

where  $L_w^{0+}$  is the abovewater water-leaving radiance (corrected for air-water interface reflection) and  $E_d^{0+}$  is the abovewater downwelling irradiance (Mobley, 1994). This parameter is very simply related to ( $\pi$  times) the commonly used remote sensing reflectance,

$$R_{rs}(\lambda) = \frac{L_w^{0+}}{E_d^{0+}} \quad (10.2)$$

Some typical water-leaving reflectance spectra for different water types are shown in Figure 58.

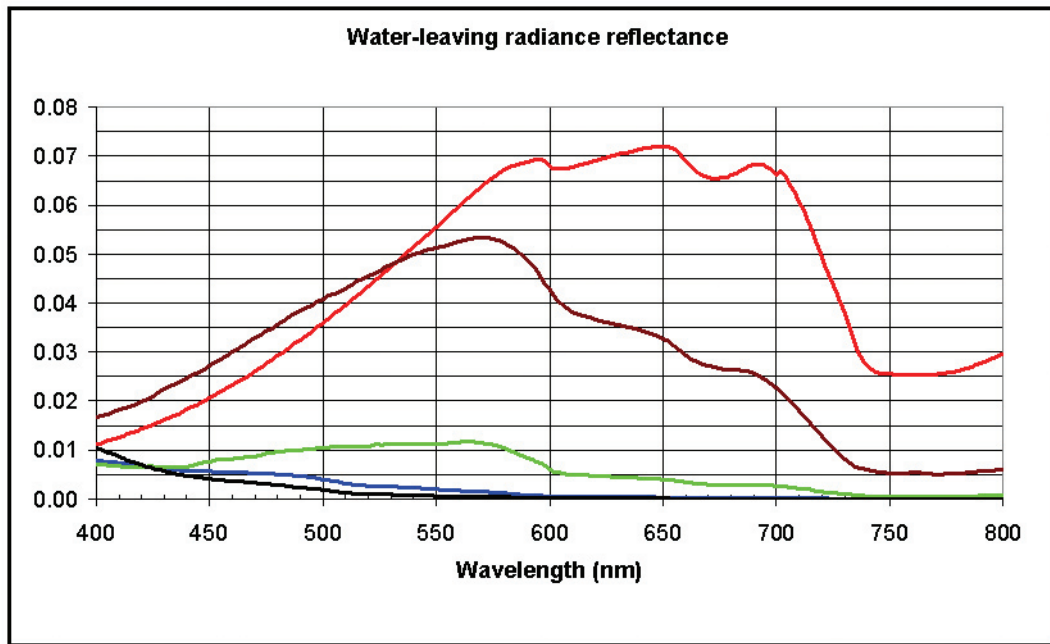


>> Figure 58: Typical reflectance spectra for water of various composition: very clear, blue water (black), clear water with some phytoplankton (blue), water with low particle concentration but high chlorophyll a (green), water with high total suspended matter (brown), water with extremely high total suspended matter and high chlorophyll a (red).

The interaction of light with sea water, including dissolved and particulate constituents, can be considered by applying radiative transfer equations where interactions are represented by inherent optical properties such as the total absorption coefficient and volume scattering function. Approximate solutions of the radiative transfer equations have been obtained (Gordon et al., 1975; Kirk, 1981; Morel and Prieur, 1977) allowing water-leaving reflectance to be expressed as a function of total absorption coefficient,  $a(\lambda)$ , and total backscattering coefficient,  $b_b(\lambda)$ . In this section such an approximate solution is presented in order to illustrate briefly the spectral shape of water-leaving reflectance and its variation with chlorophyll-a and non-algae particle concentrations and CDOM absorption.

Since the purpose here is to give a first impression of the colour of processes, in the present section it is assumed that the water column is vertically homogeneous (Philpot, 1987; Vasilkov et al., 1999) and that bottom reflection, (Ackleson, 2003) Raman emission, (Haltrin and Kattawar, 1993; Sugihara et al., 1984) phytoplankton fluorescence (Babin et al., 1996; Gower et al., 1999) and yellow substance fluorescence (Hoge et al., 1993) are neglected. For a more detailed description of exceptions to these assumptions the reader is referred to the above references.

### 10.2.2 THE HYPERTEACH OCEAN COLOUR MODEL

This section describes the simple HYPERTEACH ocean colour model, which takes as input the chlorophyll-a concentration,  $C$ , the concentration of non-algae particles,  $X$ , and the CDOM absorption at 443 nm,  $Y$ . From these three variables, using the theory of aquatic optics and certain simplifying assumption, the water-leaving radiance reflectance spectrum,  $\rho_w^{0+}$ , is calculated. By playing with the computer version of this model, students can vary continuously,  $C$ ,  $X$  and  $Y$  and observe the consequent variation of  $\rho_w^{0+}$ , thus understanding how the composition of water affects its colour.

#### a. Absorption

The total absorption coefficient is decomposed into components representing the absorption coefficients respectively of: pure water (molecules),  $a_w$ , phytoplankton,  $a_{ph}$ , non-algae particles,  $a_{NAP}$ , and coloured dissolved organic matter,  $a_{CDOM}$ , as follows:

$$a(\lambda) = a_w(\lambda) + a_{ph}(\lambda) + a_{NAP}(\lambda) + a_{CDOM}(\lambda) \quad (10.3)$$

where  $\lambda$  represents wavelength. Each of these components is in turn modelled as follows:

The tabulated data for  $a_w(\lambda)$  of (Buiteveld et al., 1994) is used

$$a_{ph}(\lambda) \text{ is modelled as an increasing, slightly non-linear function of chlorophyll-}a \text{ concentration, } C$$

$$a_{ph}(\lambda) = A(\lambda)C^{1-B(\lambda)} \quad (10.4)$$

where  $A(\lambda)$  and  $B(\lambda)$  are empirical spectral values tabulated by (Bricaud et al., 1995)

$a_{NAP}(\lambda)$  is modelled as a linear function of the concentration of non-algae particles,  $X$ , with spectral variation given by (Babin et al., 2003b)

$$a_{NAP}(\lambda) = Xa_{NAP}^*(443nm) e^{-S_{NAP}(\lambda-443nm)} \quad (10.5)$$

using a logarithmic spectral slope of  $S_{NAP} = 0.0123nm^{-1}$ , and specific absorption of

$$a_{NAP}^*(443nm) = 0.041m^2g^{-1}$$

and  $a_{CDOM}(\lambda)$  is modelled with respect to the CDOM absorption at 443 nm,  $Y = a_{CDOM}(443nm)$ , as an exponentially decreasing function of wavelength according to the measurements of (Babin et al., 2003b)

$$a_{CDOM}(\lambda) = Y e^{-S_{CDOM}(\lambda-443nm)} \quad (10.6)$$

using a logarithmic spectral slope of  $S_{CDOM} = 0.0176nm^{-1}$ .

### b. Backscatter

The total backscatter coefficient is similarly decomposed into components representing the backscatter coefficients respectively of: pure water (molecules),  $b_{bw}$ , phytoplankton,  $b_{ph}$ , and non-algae particles,  $b_{bNAP}$ , as follows:

$$b_b(\lambda) = b_{bw}(\lambda) + b_{ph}(\lambda) + b_{bNAP}(\lambda) \quad (10.7)$$

where  $\lambda$  represents wavelength. Each of these components is in turn modelled as follows:

$b_{bw}(\lambda)$  is modelled according to (Morel, 1974)

$$b_{bw}(\lambda) = 0.5 * 0.00288 * \left( \frac{\lambda}{500nm} \right)^{-4.32} \quad (10.8)$$

$b_{ph}(\lambda)$  is modelled using a simplified wavelength-independent version of the formulation of (Morel and Maritorena, 2001):

$$b_{ph}(\lambda) = \{0.002 + 0.01 * [0.50 - 0.251 \log_{10} C]\} * 0.416 C^{0.766} \quad (10.9)$$

$b_{bNAP}(\lambda)$  is modelled as a linear function of the concentration of non-algae particles,  $X$ , with power law spectral variation, (Morel and Prieur, 1977) specific scattering taken from (Babin et al., 2003a) and assuming a scattering to backscattering ratio of 0.02 from Petzold: (Mobley, 1994)

$$b_{bNAP}(\lambda) = 0.02 * 0.51m^2g^{-1} * X * \left( \frac{\lambda}{555nm} \right)^{-n} \quad (10.10)$$

For the purposes of this lesson the power law exponent is taken as  $n = 0$ , giving the simpler wavelength-independent formulation:



$$b_{bNAP}(\lambda) = 0.02 * 0.51 m^2 g^{-1} * X \quad (10.11)$$

### c. Reflectance

Finally the water-leaving radiance reflectance,  $\rho_w^{0+}$ , is modelled from radiative transfer studies such as that of (Morel and Gentili, 1996) as:

$$\rho_w^{0+}(\lambda) = \frac{\pi \mathcal{R}f'}{Q} \frac{b_b(\lambda)}{a(\lambda) + b_b(\lambda)} \quad (10.12)$$

According to optical theory the factor  $\gamma = \pi \mathcal{R}f' / Q$  may vary by a few tens of percent as function of sun and viewing angles, waves (and hence wind speed), particle type, etc. However, for the purposes of this lesson it will taken as a constant:  $\gamma = \pi * 0.53 * 0.09 = 0.15$ .

Although not imposed directly as an input variable, the total suspended matter (in  $g/m^3$ ),  $T$ , is calculated from the inputs for non-algae particle concentration (in  $g/m^3$ ) and chlorophyll-a concentration (in  $mg/m^3$ ) via:

$$T = X + 0.07C \quad (10.13)$$

### d. Implementation

Thus, the model can be summarized in the following steps:

User inputs  $C$ ,  $X$  and  $Y$ .  $T$  is not a free input variable but is calculated from  $C$  and  $X$ .

Spectral absorption and backscatter coefficients  $a$  and  $b_b$  are calculated from  $C$ ,  $X$  and  $Y$ . Spectral water-leaving radiance reflectance  $\rho_w^{0+}$  is calculated from  $a$  and  $b_b$ .

This model has been programmed in an Excel spreadsheet, which students will use in HyperTeach Hands-on Lesson 3.

# 11 Geology

## 11.1 Spectral properties of soil, rocks, minerals

When light interacts with matter, electronic transitions, vibrational or rotational processes occur (Figure 59).

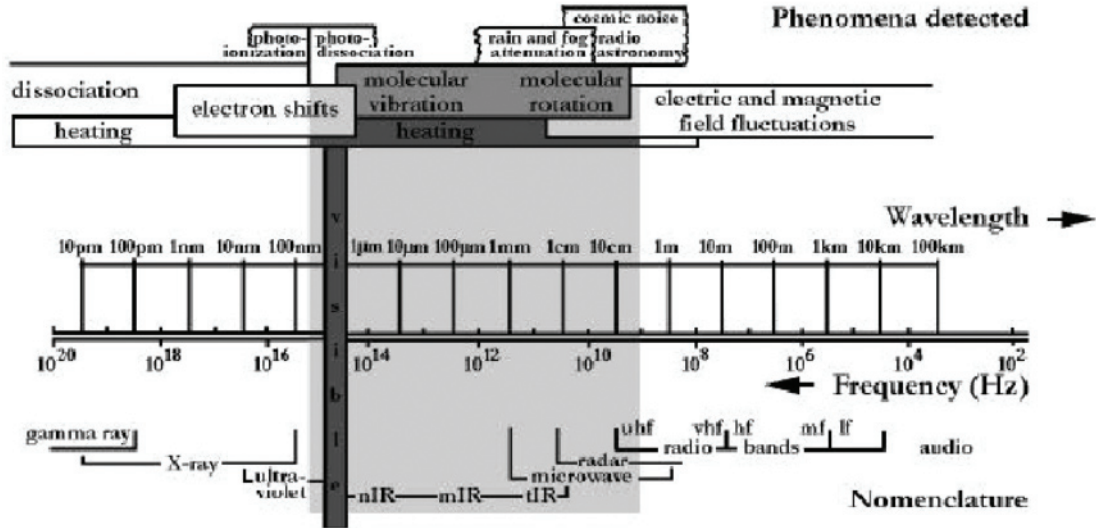


>> Figure 59: Electronic, vibrational and rotational transitions related to wavelength and frequency (from Drury, 1993 and Atzberger).

**Electronic** transitions happen when an electron moves from low orbit to higher orbit, require high excitation energies and thus occur at shorter wavelengths in the spectrum (ultraviolet and visible) (Figure 60). Electronic transitions occur in solids, liquids and gases.

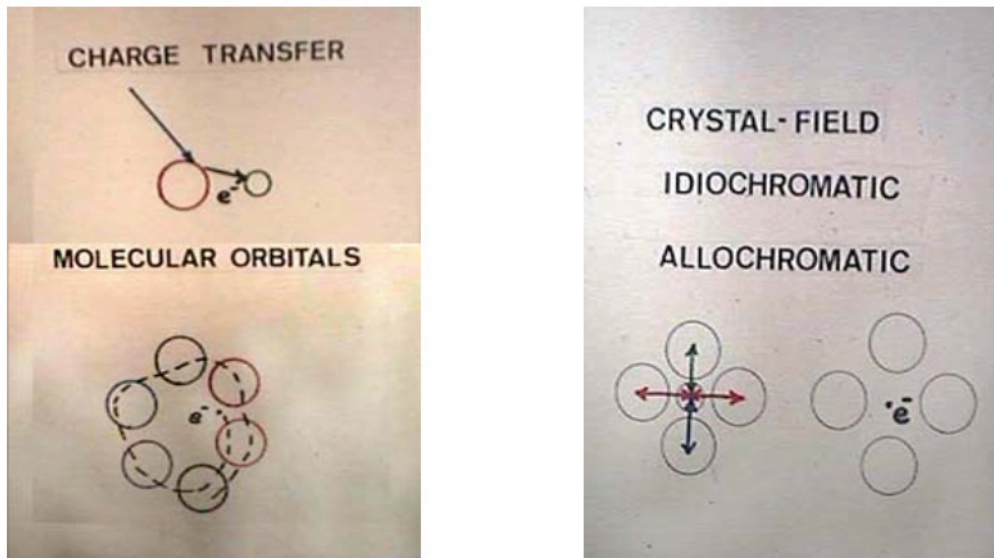


>> Figure 60: Electronic transitions.

**Vibrational** transitions like stretching or bending from one equilibrium state to another require less energy and thus occur at longer wavelengths (infrared and beyond) (Figure 61). Vibrational transitions occur in solids, liquids and gases.

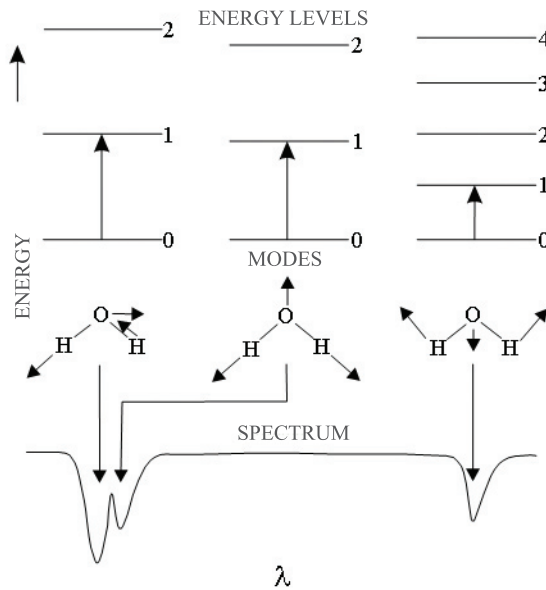
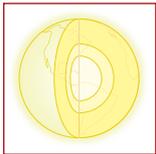


>> Figure 61: Possible vibrational states in a water molecule. Top: energy and energy levels; Middle: vibrational mode (in sense of arrow); Bottom: resulting spectrum.

**Rotational** transitions are related to changes in the momentum of inertia of the rotating molecules (Figure 62). Rotational transitions occur at infrared wavelengths and beyond. Rotational transitions are restricted to gases, but play an important role in remote sensing because of the major influence of the Earth's atmosphere.

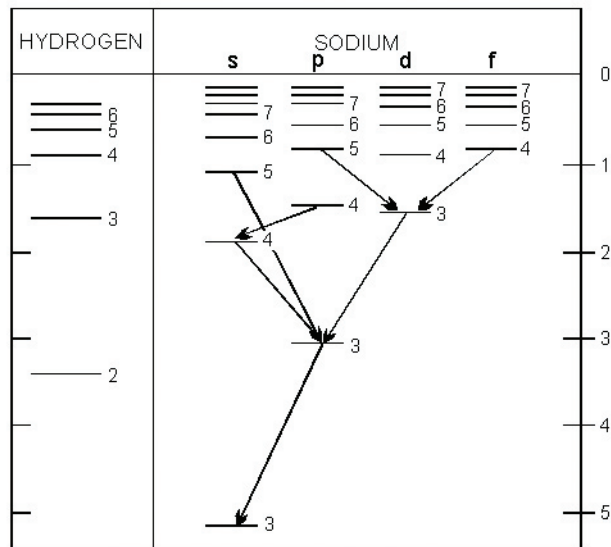


>> Figure 62: Rotational energy levels for one atom (hydrogen) and several (sodium) electrons. Some possible transitions are indicated.

Many visible colours are due to interactions between atoms. Charge-transfer colours result when photons cause an electron transfer from one atom to another. Molecular orbitals, common in organic materials, occur when electrons are bound collectively to entire molecules rather than single atoms. Colours due to specific atoms in a material are called crystal-field colours. The physics is very complex because neighbouring atoms distort the energy levels of orbital electrons. As shown in Figure 59, these interactions between energy and matter occur in a wider wavelength range than the visible.

Electronic transitions require highly energetic photons compared to vibrational and rotational transitions and therefore occur at shorter wavelengths (VNIR). The position, shape, depth and width of the absorption features are directly related to the crystal structure and the chemical composition of the Earth's surface material.

The VNIR and SWIR spectral range are excellent for detecting electronic transitions in minerals (e.g. iron oxides, Fe<sup>2+</sup> bearing minerals, etc.), vegetation (vegetation species, health, green leaf water content), and vibrational absorptions due to lighter elements (OH<sup>-</sup>, SO<sub>4</sub><sup>2-</sup>, CO<sub>3</sub><sup>2-</sup>, CH<sup>+</sup> etc., so that OH-bearing minerals, carbonates, sulphates and organics are detectable).

Actual detection of a material is dependent on the spectral coverage, the spectral resolution, and the signal-to-noise ratio of the spectroradiometer. The abundance of the material and the strength of its absorption features in the spectral region under consideration are also important factors affecting the detection.

### 11.1.1 REFLECTANCE PROPERTIES OF MINERALS

Natural surfaces are most often irregular and composed of small particles. Spectra of surfaces can be recorded using spectroradiometers in the field or in the laboratory. The radiation impinging on a detector interacted with the observed object (and thus contain information of the observed object): it was partially reflected, diffused (once or several times) and absorbed.

As described earlier, absorption happens preferentially at particular wavelengths. The complete spectrum of an object is characterised by a series of "absorption features" that uniquely define the spectral signature of an object. Signature features for minerals and rocks result from very characteristic electronic and vibrational processes since rotation is impossible in solids. The spectral characteristics of the different mineral components of rocks and composite minerals are so different that in most cases the individual pure minerals can be identified, though not in a linear way.

Besides rock and mineral fragments, soils may also contain an organic fraction and water. These elements have a major impact on the signature of the individual mineral components.

The shape of the spectrum is the result of physical processes and is closely related to the chemical composition of a mineral. Chemical variation in minerals is either the result of substitutions in the crystalline grid (solid solutions) or of variations in the architecture of the crystalline grid geometry (e.g. mica's).

Six major mineral families can be identified, each with their particular characteristic absorption features in their spectra:

1. feldspars and quartz
2. carbonates
3. ferromagnesian minerals
4. clays and mica's
5. alteration/hydrothermal minerals
6. oxides, hydroxides and sulfides

#### 1. Feldspars and quartz

As can be seen in Figure 63, quartz (SiO<sub>2</sub>) in its pure form possesses a flat spectrum without absorption features (spectrally white) and has a high albedo. The scarce features that can be observed in the VNIR and SWIR result of fluid (H<sub>2</sub>O) or solid (TiO<sub>2</sub>) inclusions or from impurities in the crystal grid.

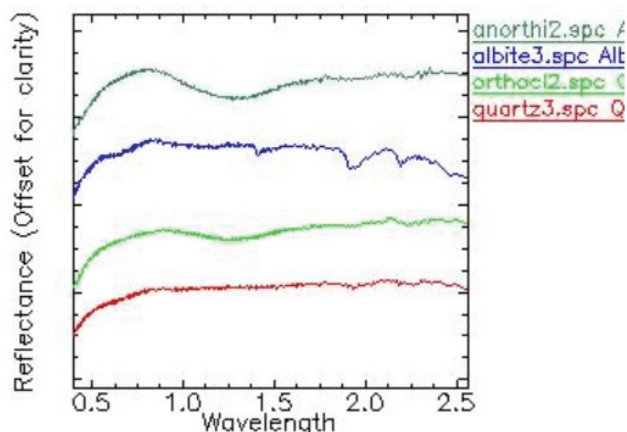


>> Figure 63: Reflectance spectra of quartz and feldspars. (Wavelength in μm)

Macroscopically, feldspars always possess a bright colour (white, pink, light green, .....). Just like quartz, the pure minerals are spectrally white and have a high albedo.

Sometimes, features exist due to the substitution of the  $Al^{3+}$  kation by  $Fe^{3+}$  (550 and 650 nm respectively), resulting in a decrease of reflectance in the blue part of the spectrum. The presence of fluid inclusions of  $H_2O$  and  $CO_2$  (at 1400, 1900 and 2200 nm) or solid inclusions like  $Fe_2O_3$  (native or through erosion) also result in dominant features.

### 2. Carbonates

Carbonates (dolomite, calcite, aragonite, magnesite, strontianite, malachite, etc.) possess the typical  $CO_3^{2-}$  ion that is linked to  $Ca^{2+}$ ,  $Fe^{2+}$ ,  $Mg^{2+}$ ,  $Mn^{2+}$ ,  $Cu^{2+}$ ,  $Sr^{2+}$ .

The vibrational properties of the carbonate ion result in five specific absorption features in the SWIR range between 1800 and 2500 nm. Other, broader features in the VNIR around 1000 nm are attributed to substitution of  $Ca^{2+}$ ,  $Fe^{2+}$ ,  $Mg^{2+}$ ,  $Mn^{2+}$ ,  $Cu^{2+}$ ,  $Sr^{2+}$  ions by  $Fe^{3+}$ .

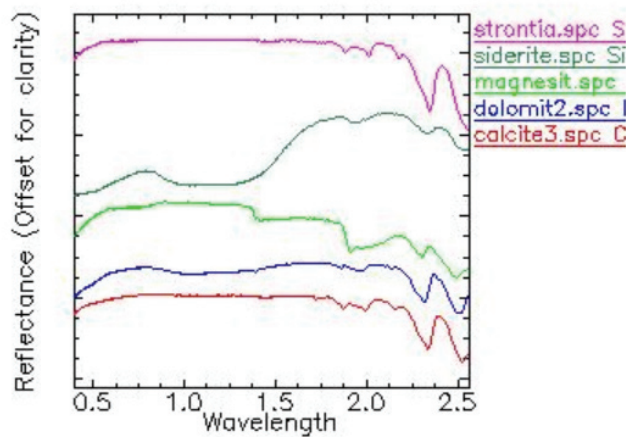


>> Figure 64: Reflectance spectra of carbonates. (Wavelength in  $\mu m$ )

### 3. Ferromagnesian minerals

Amphiboles and pyroxenes are dark coloured chain-like inosilicates (black, dark green or dark blue). For the pyroxenes it is very difficult to identify spectral discriminating criteria. The Fe ion is the only component that can generate absorption features in the VNIR and SWIR.

Just like for the pyroxenes, absorption peaks of amphiboles in the VNIR and SWIR part of the spectrum result from  $Fe^{2+}$  and  $Fe^{3+}$  ions. Amphiboles however, also possess narrow features at 1400 and 2300 to 2400 nm resulting from the vibration of the OH group in their crystalline grid.

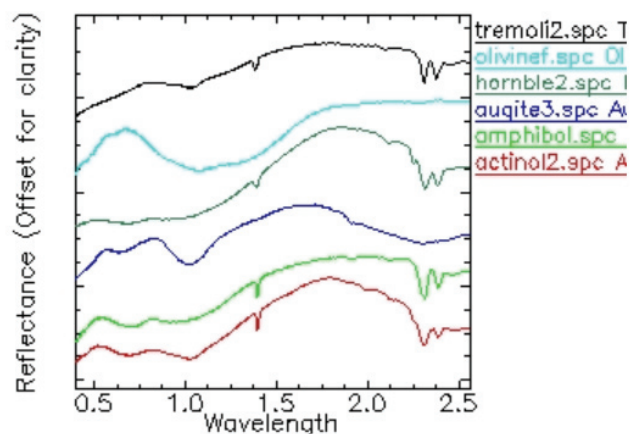


>> Figure 65: Reflectance spectra of ferromagnesian minerals. (Wavelength in  $\mu m$ )

### 4. Clays and mica's

The spectral signature of clays and mica's are dominated by a series of major absorption peaks in the SWIR range. These features are attributed to the presence of OH groups and intermolecular H<sub>2</sub>O.

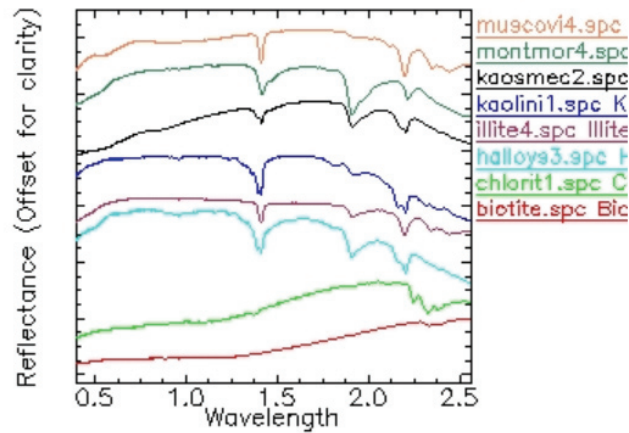


>> Figure 66: Reflectance spectra of clay minerals and mica's. (Wavelength in µm)

The position of the peaks at 1400 nm and between 2100 and 2400 nm is controlled by the di- or trioctaedric structure of the mineral. Dioctaedric (kaolinite, montmorillonite, halloysite, pyrophyllite) with Al-OH groups result in an absorption peak at 2000 nm, while trioctaedrics (talcum, serpentine, chlorite, mica's) with their Mg-OH group have a peak at 2300 nm.

### 5. Alteration/hydrothermal minerals

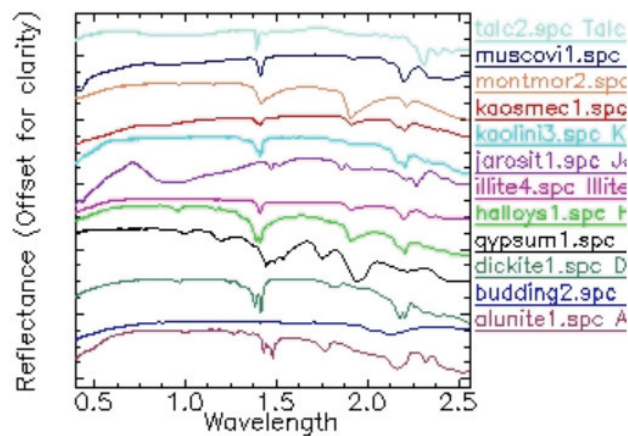


>> Figure 67: Reflectance spectra of some alteration minerals. (Wavelength in µm)

Hydrothermal minerals are mainly characterized by absorption features in the SWIR range due to vibrational transitions. Amongst them, the kaolinite and halloysite doublet with the main absorption peak at 2200 nm. Figure 67 shows the significant variations in wavelength and shape of the absorption peaks. Many of them are characteristic of a single species, though illite and muscovite spectra are very similar, and thus difficult to discriminate.

6. Oxides, hydroxides and sulfides

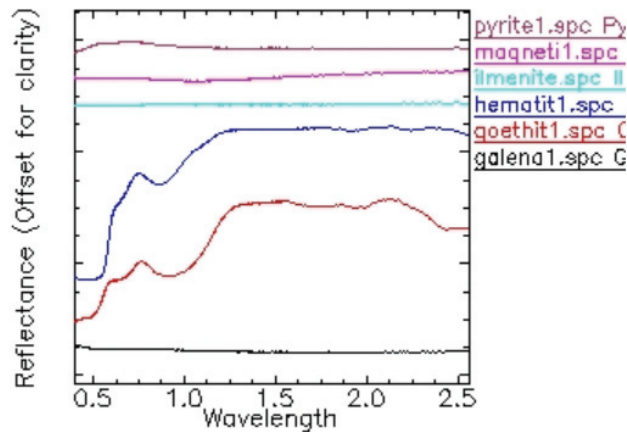


>> Figure 68: Reflectance spectra of some oxides, hydroxides and sulfides. (Wavelength in µm)

Most oxides, hydroxides and sulfides of Fe, Al and Mg (magnetite, ilmenite, pyrite, galena,...) have a flat featureless spectrum and a low albedo in the 400 to 2500 nm wavelength interval which is of interest for geological applications.

The presence of these minerals in a rock, even in small amounts, has a "flattening" effect on the spectral signature and often hides other features.

Minerals like hematite, goethite and limonite react like transopaques and can thus have well-marked features resulting from electronic transitions in the VNIR range.

11.1.2 REFLECTANCE PROPERTIES OF ROCKS

As shown in the previous section, minerals, which are the building elements of rocks (both solid and loose), possess characteristic spectral features, often giving them a unique spectral signature. Rocks also have a spectral signature, reflecting their respective composing individual minerals in a non-linear way. This non-linearity prevents a rock (or rock family) to be directly identified from its spectral signature in terms of chemical or mineralogical composition.

The spectral signature of rocks is determined by the optical path of the EMR, which is back scattered with spectral absorptions depending of the mineral species met during this path. Granulometry and texture also have an important influence in this process.

For magmatic rocks, the main classification criteria are the presence and amount of quartz and feldspars. Because the signature of both minerals is spectrally flat (Section 11.1.1) their presence will not influence the spectral signature of a magmatic rock.

Other components present in these rocks (ferromagnesian minerals, micas, opaque, carbonates) even in orders of magnitudes less than quartz and feldspar will have a major impact on the spectral signatures. In mafic rocks for instance, pyroxenes and amphiboles often have a significant contribution to the spectral signature.

Another typical example comes from opaque minerals: they have a damping effect that is not proportional to their relative amount.

The same phenomena apply for metamorphic rocks. An example is the strong contribution of minerals like glaucophane in the "blue schist" facies.

In sedimentary rocks, the most prominent spectral features come from clay minerals in shale, carbonate in limestone, oxides and hydroxides (red rocks).

Pure white sand, composed of quartz grains, will have no spectral absorption at all, and for this reason will be a good candidate for a flat field calibration procedure (Section 8.1.2.1).

**11.2 Spectral profiles and libraries in geology**

**11.2.1 MINERAL MAPPING WITH SPECTRAL LIBRARIES**

One approach to analyse a (hyper)spectral image in terms of mineral composition is attempting to match each image spectrum individually to one of the reference reflectance spectra in a spectral library. This approach requires an accurate calibration of image radiance data to reflectance. It works best if the scene includes extensive areas of essentially pure materials that have corresponding reflectance spectra in the reference library.

The spectral signatures in the spectral library can be either laboratory measurements from an existing database (e.g. USGS spectral library: <http://speclab.cr.usgs.gov/>), own spectral laboratory or field measurements or spectra extracted from the images.

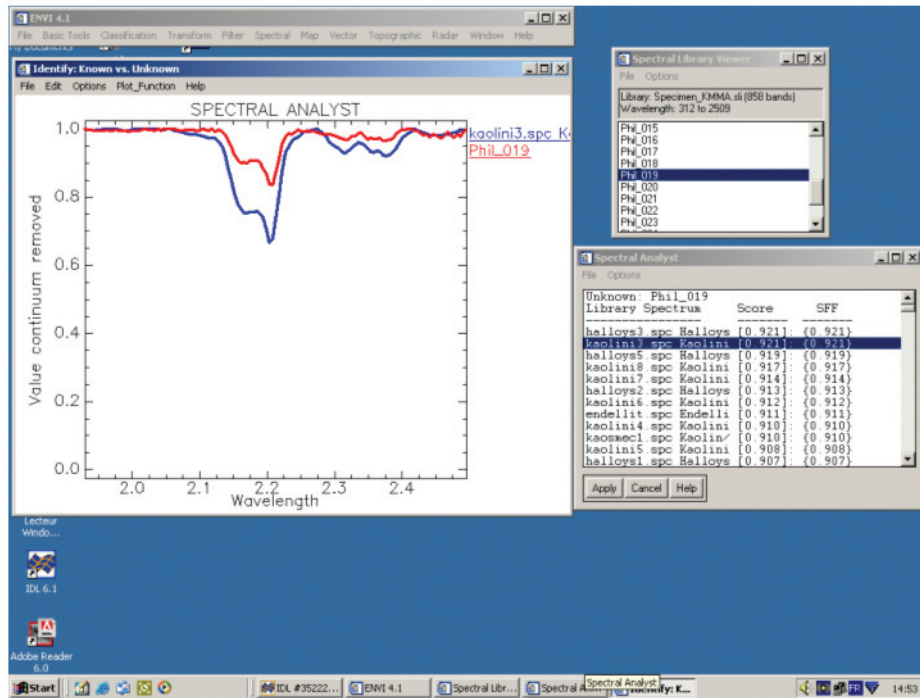


>> Figure 69: Spectral analysis of a hand specimen compared to the USGS mineral database.

An observed spectrum will typically show varying degrees of match to a number of similar reference spectra. The matching reference spectra must be ranked using some "goodness of fit" measure. Figure 69 shows the comparison of a spectral feature of a red clay siltstone, mainly composed of kaolinite with a small amount of iron oxide, with a pure kaolinite database signature in the SWIR range.

Spectral matching in remote sensing is complex due to the fact that most hyperspectral scenes include many image pixels that represent spatial mixtures of different materials. The resulting composite image spectra may match a variety of "pure" reference spectra to varying degrees, perhaps including some spectra of materials that are not actually present. If the best-matching reference spectrum has a sufficient fit to the image spectrum, then this material is probably the dominant one in the mixture and the pixel is assigned to this material. If no reference spectrum achieves a sufficient match, then no endmember dominates, and the pixel should be left unassigned.

The result is a so-called material map of the image that portrays the dominant material for most of the image cells, such as the example shown in Figure 70. Sample mixed spectra can be included in the library to improve the mapping, but it is usually not possible to include all possible mixtures (and all mixture proportions) in the reference library.

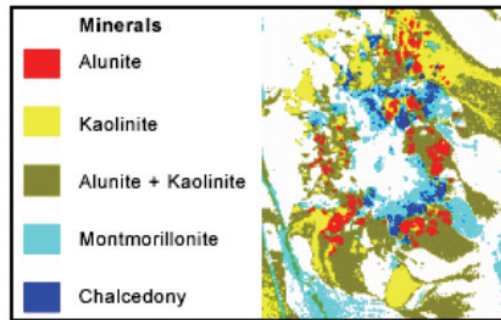
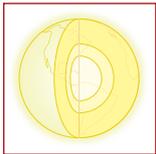
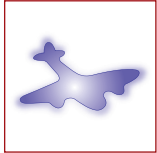


>> Figure 70: Example of a material map as a result of spectral library matching.

### 11.2.2 SPECTRAL ANALYSIS METHODS IN GEOLOGY

The shape of a reflectance spectrum can usually be broken down into two components: broad, smoothly changing regions that define the general shape of the spectrum and narrow, trough-like absorption features (Figure 71).

This distinction leads to two different approaches to matching image spectra with reference spectra.

Many pure materials, such as minerals, can be recognised by the position, strength (depth) and shape of their absorption features only. One common matching strategy attempts thus to match only the absorption features in each candidate reference spectrum and ignores other parts of the spectrum.

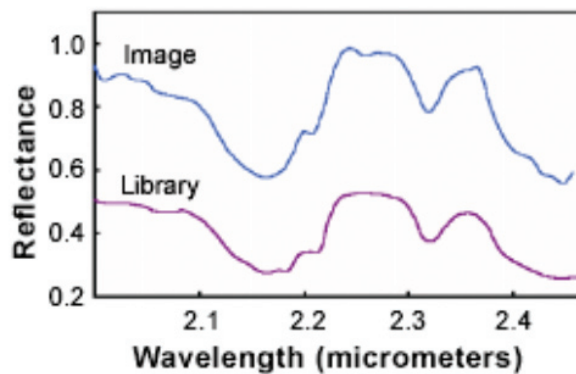


>> Figure 71: Sample image spectrum and matched spectrum of the mineral alunite from the USGS Spectral Library (goodness of fit = 0.91).

A unique set of wavelength range is therefore examined for each reference candidate, determined by the locations of its absorption features (Figure 71). The local position and slope of the spectrum can affect the strength and shape of an absorption feature, so these parameters are usually determined relative to the continuum, i.e. the upper limit of the spectrum's general shape.

The continuum is computed for each wavelength subset and removed by dividing the reflectance at each spectral channel by its corresponding continuum value (Figure 72). Absorption features can then be matched using a set of derived values (e.g. depth and the width at half-depth) or by using the complete shape of the feature.

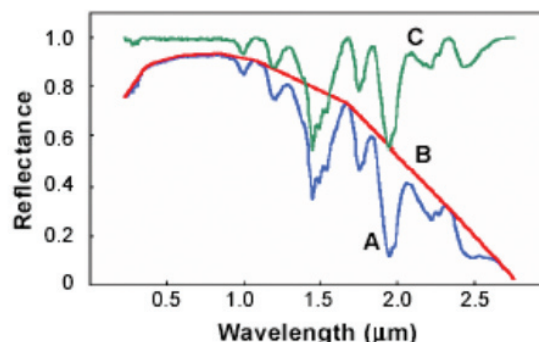


>> Figure 72: Reflectance spectrum for the mineral gypsum (A) with several absorption features. Curve B shows the continuum for the spectrum and C the spectrum after removal of the continuum.

These types of procedures have been organised into an expert system by researchers at the USGS Spectroscopy Lab (Clark et al., 1990).

### 11.2.3 LINEAR SPECTRAL UNMIXING

Linear spectral unmixing, as described in Section 9.1.3.1, is an alternative approach to simple spectral matching. Its underlying premise is that a scene includes a relatively small number of common materials with more or less constant spectral properties.

Furthermore, much of the spectral variability in a scene can be attributed to spatial mixing, in varying proportions, of these common endmember components. If we can identify the endmember spectra, we can mathematically “unmix” each pixel’s spectrum to identify the relative abundance of each endmember material.

The unmixing procedure models each image spectrum as the sum of the fractional abundances of the endmember spectra, adding up to 1. The challenge in linear unmixing is to identify a set of spectral endmembers that match actual physical components on the surface.

Endmembers can be identified directly from the image using field information or by an empirical selection technique such as partial unmixing (described in Section 11.2.4). Alternatively, endmember reflectance spectra can be selected from a reference library (described in Section 11.2.1 and 11.2.2), but this approach requires that the image has been accurately converted to reflectance values.

Variations in illumination can be included directly in the mixing model by defining a “shade” endmember that can mix with the actual material spectra.

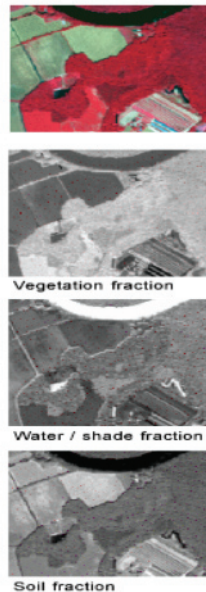
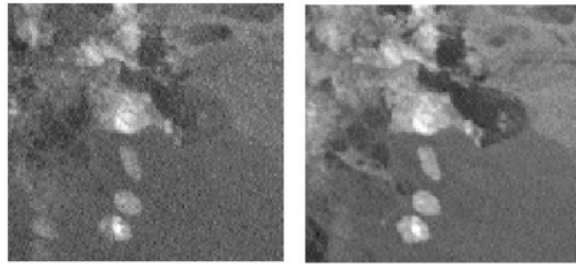
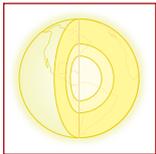
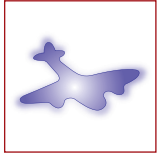


>> Figure 73: Portion of an AVIRIS scene with forest, bare and vegetated fields, and a river, shown with a color-infrared band combination (vegetation is red). Fraction images from linear unmixing are shown in gray-scale.

### 11.2.4 PARTIAL UNMIXING FOR GEOLOGIC APPLICATIONS

Some hyperspectral image applications do not require finding the fractional abundance of all endmember components in the scene. Instead, the objective may be to detect the presence and abundance of a single target material. In this case a complete spectral unmixing is not necessary. Each pixel can be treated as a potential mixture of the target spectral signature and a composite signature representing all other materials in the scene. Finding the abundance of the target component is then essentially a partial unmixing problem.

The procedures are the same as for the linear unmixing.



Fraction images produced by Matched Filtering (left) and Derivative Matched Filtering (right) for a portion of the Cuprite AVIRIS scene. The target image spectrum represents the mineral alunite. Brighter tones indicate pixels with higher alunite fractions. The image produced by Derivative Matched Filtering shows less image noise, sharper boundaries, and better contrast between areas with differing alunite fractions.

>> Figure 74:(Left) A simple example of linear unmixing a scene in its basic components. (Right): An example of partial unmixing; here only targeting the presence of alunite.

### 11.3 General analysis tools

The general hyperspectral analysis tools used in almost all the hyperspectral domains of applications can also be used for geological mapping.

After spectral range selection related to the type of spectral features that are looked for (e.g. the SWIR range to evidence vibrational processes), classical image processing like hyperspectral indexes, classifications, principal components analysis can be applied. For geologic applications, a mask based on a NDVI threshold is usually used to mask out vegetation.

The specific suite of operations known as the "ENVI hourglass" can be quite successful in mineral applications. It consists in successively applying:

- Minimum Noise Fraction
  - Pixel Purity Index
  - n-D visualizer and endmembers selection
  - Spectral analyst
  - Mapping tools
    - Linear Spectral Unmixing
    - Spectral Angle Mapper (SAM)
    - Spectral Feature Fitting (SFF)
- An automatic procedure can also be used:
- Sequential Maximum Angle Convex Cone (SMACC)

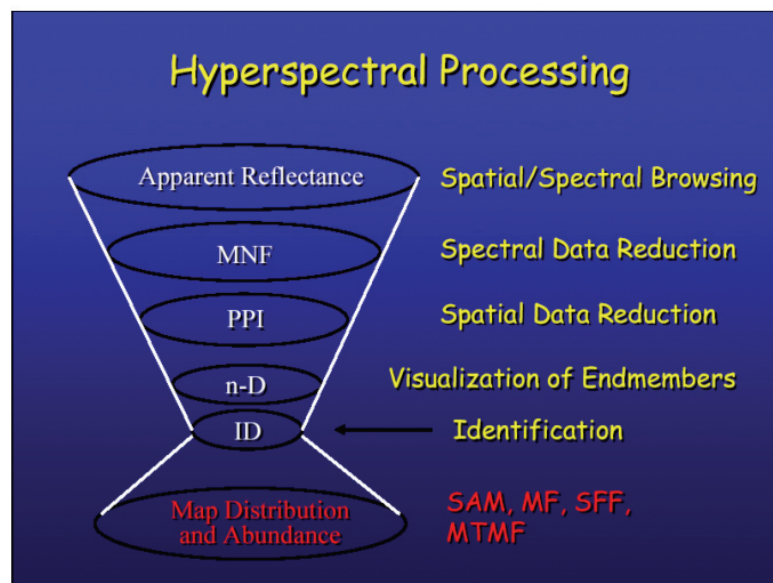


>> Figure 75: Schematic overview of the "hourglass" processing sequence.

However, it is very important to be aware that, due to the complexity of rock spectral signatures, "spectral endmembers" are not representative of rock facies.

For this reason, the latest methods will not be used for lithological mapping and their use will be restricted to the search for pure mineral occurrences.

### 11.4 Case study: The Cuprite test site (US, Nevada)

Cuprite is part of an active mining area in Nevada, US. Due to the (semi)arid environment and the fact that the geological setting of this area is very well known, this site is regularly selected by NASA to test new airborne and spaceborne sensor concepts.

The following example shows the results of such a test; in this case the purpose was to evaluate the quality of the data collected by the first hyperspectral sensor – HYPERION – which is carried on the Earth Observation 1 (EO1) platform.

The Hands-on Lessons 6, 7 and 8 will go much more detailed into the whole processing chain for spectral geological applications. We will use for this a dataset from the same airborne AVIRIS sensor that was used in this case study.

This mineral identification application in the SWIR range, by Dr. Pamela Barry of TRW Space & Electronic Group, and by Dr. Fred Kruse of AIGLLC, is presented in the frame of USGS case studies. It compares the performances of the HYPERION spaceborne sensor with the AVIRIS airborne sensor.

The test site geology is dominated by siliceous to basic volcanic rocks of tertiary age. The mineralisations are associated to hydrothermal alteration that will be mapped here.

The distribution of the alteration minerals in the Cuprite area is described in Figure 76.

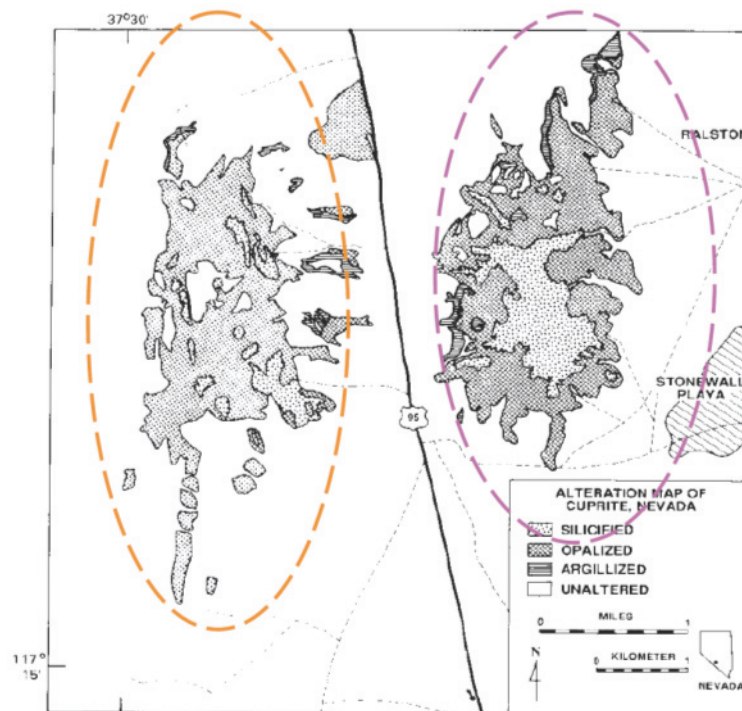


>> Figure 76: Alteration minerals at Cuprite.

#### Importance of Alteration

- Studying the presence and distribution of minerals provides insight into the history of what occurred in the area
- The history of the region can be combined with knowledge of the formation of minerals to provide valuable information about the area

## PART II: THEMATIC APPLICATIONS

- Remote sensing enables environmental assessment of areas around the world
- Pattern and distribution of visible minerals (e.g. alunite and kaolinite) can point to precious minerals which are not visible (e.g. gold)

For example: deposits of gold and silver associated with mineralising events that occurred during Tertiary time and were associated with late stage volcanic events.

The reference spectra of significant alteration minerals in Cuprite area are presented in Figure 77.

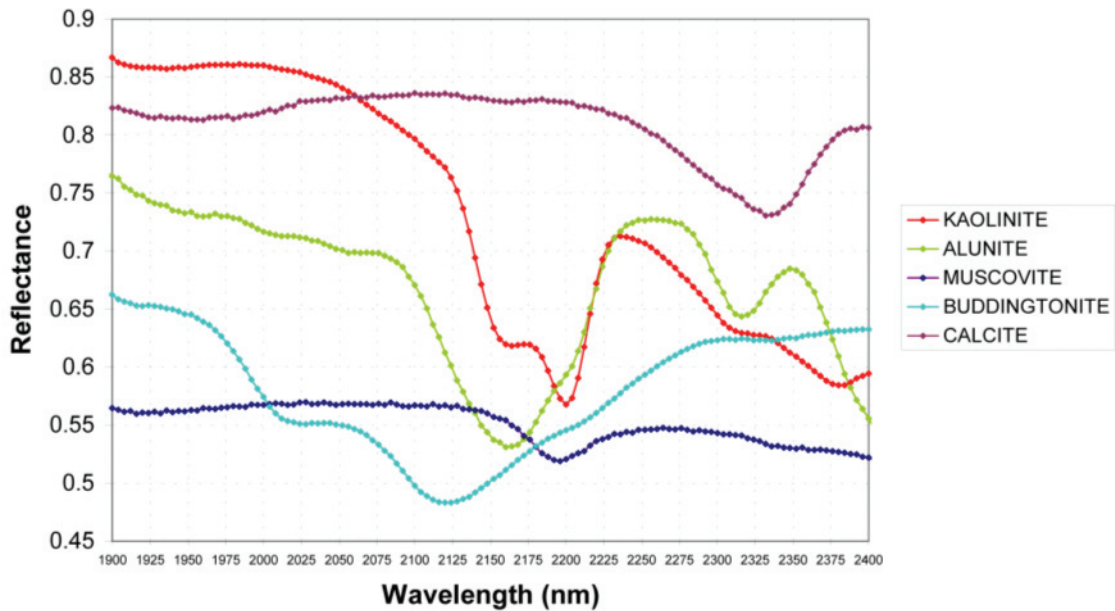


>> Figure 77: Reflectance spectra of alteration minerals in the Cuprite area (JPL spectral library in ENVI).

The sequence of operations performed to map the alteration minerals is shown in Figure 75 of Section 11.3. Figure 78a and 78b display the result of the processing of AVIRIS and HYPERION data.

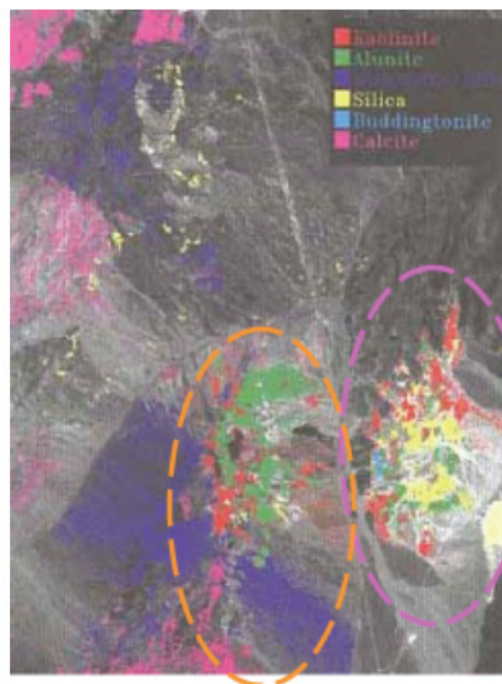


>> Figure 78a: HYPERION mineral mapping.

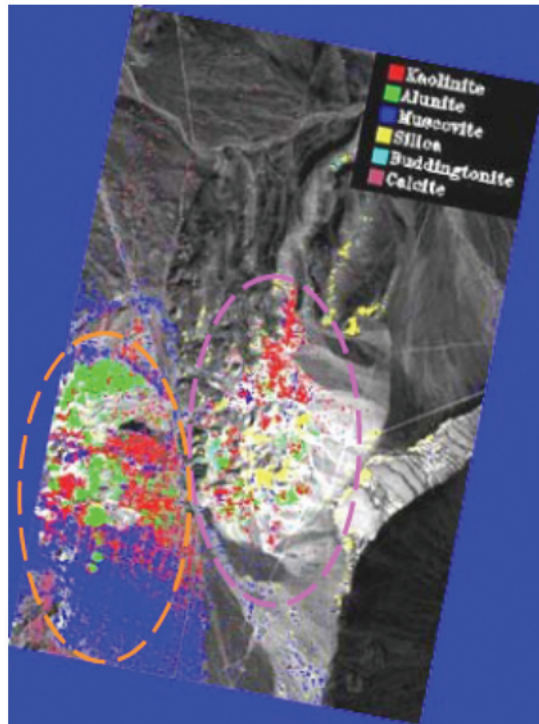
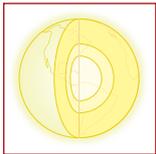
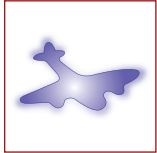
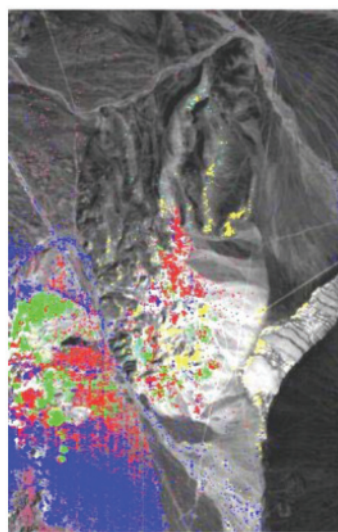
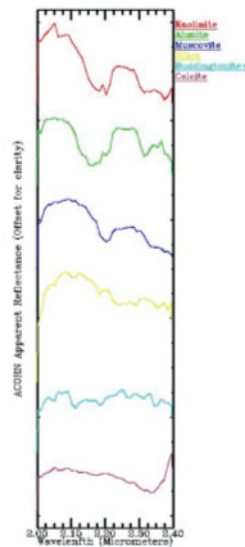


>> Figure 78b: AVIRIS mineral mapping.

In this case study, the processing of the SWIR data of the HYPERION images resulted in a good match to spectral libraries data, as shown in Figure 79.



**Hyperion SWIR Mineral Map  
By AIGLLC**



**Hyperion SWIR  
End member Spectra**

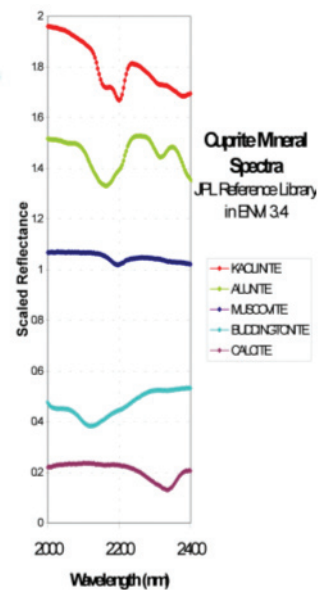


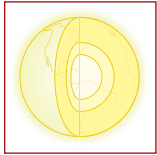
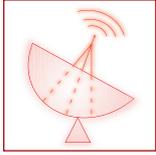
>> Figure 79: HYPERION SWIR mineral map (left). HYPERION SWIR apparent reflectance spectra (middle) and spectral library reference reflectance spectra (right).

The complete description of the technical methods used in this case study can be found on: <http://eo1.gsfc.nasa.gov/miscPages/Workshop/Sec-05.pdf>

One can conclude that in this case study:

- HYPERION spectra compares with spectral library reference spectra
- Identification capabilities are proven in the most challenging (because of a low signal to noise ratio) region of the Hyperion spectrum: the SWIR range.
- Identification algorithms depend on the users needs and on the availability of reference material

For further information, the interested reader is referred to <http://speclab.cr.usgs.gov/PAPERS/cuprite.clark.93/>, Abrams et al., 1980; Hook, 1990; <http://edcdac.usgs.gov/samples/goldfield.html>, <http://www.borstad.com/papers/CRSS2000.html>



**12 Biodiversity applications**

**12.1 Spectral properties of vegetation**

All plants are photo-autotrophic; they use sunlight and anorganic molecules for building up organic molecules. During photosynthesis, energy from the visual part of the solar spectrum is used for manufacturing the organic compounds plants use for maintenance and growth. The pigments in the chloroplasts absorb the energy from the light and use it to convert carbon dioxide and water into sugars (carbohydrate) according to the photochemical reaction

As sunlight strikes the leaves it is partially reflected, absorbed and transmitted. The relative importance of these processes depends on wavelength, incidence angle and roughness of the leaves as well as the different optical properties and biochemical composition of the leaves. The visible part of the vegetation spectrum is characterized by a low reflectance value due to very strong absorption of the leaf pigments (Table 12).

Type pigment	Characteristic absorption maximum (nm)
Chlorophyll a	420, 490, 660
Chlorophyll b	435, 643
β-Carotene	425, 450, 480
α-Carotene	420, 440, 470
Xanthophylls	425, 450, 475

>> Table 12: Leaf pigments and their absorption maxima.

Absorption is strong in the violet – blue and red part of the spectrum. The green part of the solar spectrum is less absorbed causing plants to appear green to the human eye. Because the energy content of the non-visible short infrared part of the solar spectrum is insufficient for photochemical reactions, light at these wavelengths is not absorbed by the chlorophyll and other leaf pigments. This results in a strong increased reflectance in the near-infrared around 690 nm, known as the red-edge, which is typical for vegetation spectra. The absorption in the near-infrared range of the spectrum is due to the internal cell structure of the leaves.

Figure 80 shows two arbitrary vegetation spectra, selected from a hyperspectral CASI-2 image, with an indication of the different spectral features.

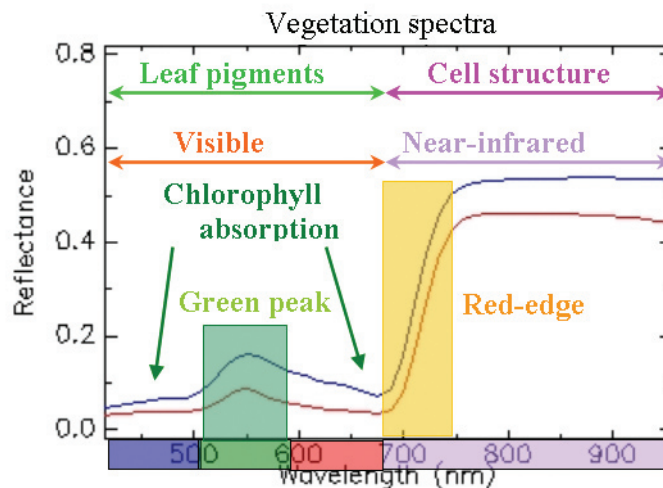


>> Figure 80: Typical reflectance spectrum characteristic to green plants.

Different vegetation types are distinguished by the relative and often subtle differences in the reflectance values in the visible (VIS) and near-infrared (NIR) part of the spectrum. For example the position and slope of the red-edge curve enables to differentiate between vegetation types.

## 12.2 Classification of vegetation species

### 12.2.1 INTRODUCTION

Different public authorities need actual and frequently updated vegetation maps of the active dunes, salt marshes and mudflats along the Belgian coast for managing the dunes. This information is used for coast protection, through which an optimal security against storms and floods is guaranteed. Besides, there is a need for vegetation maps to monitor biodiversity in the different nature reserves along the Belgian coast and to observe nature development.

At this moment, vegetation maps are made based on visual inspection of aerial photographs. This technique is time consuming, highly subjective and does not differentiate many vegetation classes. A more detailed, fast and objective mapping method would allow a much better evaluation and management.

Recently, advanced hyperspectral airborne sensors have been developed, acquiring images in hundreds of spectral bands with spatial resolution as low as one meter. In parallel, different digital image processing techniques have been developed which, by running on modern and fast computers, allow the hyperspectral imagery to be processed in a cost efficient and objective manner. Differences in the reflectance spectra, as measured by hyperspectral remote sensing techniques, are the physical basis for the proposed classification methods in this case study. These differences allow to distinguish between the different vegetation types, ecotypes or in general land use and are used to produce vegetation maps. By producing such maps on a regular time base, land changes and ecological processes can be evaluated.

### 12.2.2 AIRBORNE HYPERSPECTRAL CAMPAIGN

On October 11 2002, a flight campaign was executed with the objective of mapping the dune vegetation along the entire Belgian coast (about 30 square kilometres). Hyperspectral data was collected by the British Natural Environment Research Council (NERC). The Compact Airborne Spectrographic Imager or CASI-2 sensor (Figure 81) was mounted in a Dornier 228 aircraft and flown at an altitude of 970 m. The CASI-2 band setting is programmable and depends on the operation mode. In spatial mode the maximum swath is obtained but this will reduce the number of spectral bands. This mode is often used when the spectral signatures of the observed materials are well known. In spectral mode, the maximum number of bands can be used but this will reduce the spatial coverage. This mode is very useful when detailed spectra with high spectral resolution are needed.

This case study uses CASI-2 hyperspectral images collected in spectral mode with 48 spectral bands in the VNIR wavelength region with a spatial ground resolution of 1.3 m x 1.3 m. A small part of the imagery collected above the nature reserve 'De Westhoek' (Figure 82) is studied.



>> Figure 81: Monitor (left), control unit (middle) and optical sensor head (right) of the CASI-2 sensor (ITRES Research Limited, Canada).

Field of view (FOV)	37.8 Deg
Instantaneous field of view (IFOV)	1.3 mRAD
Spatial Resolution	0.5 - 10 m
Spectral Range	400 - 1000 nm
Spectral Channels	max. 288
Spectral Sampling Interval	1.9 nm
Spectral Resolution (FWHM)	2.2 nm
Dynamic Range	12 bits (4096)

>> Table 13: CASI-2 characteristics.

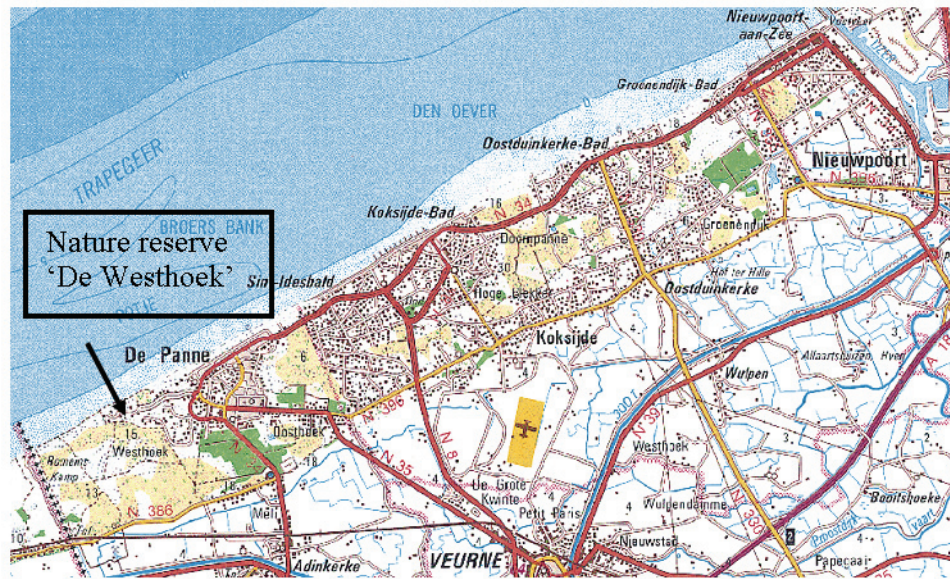
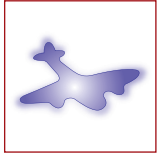


>> Figure 82: Location of the study area 'De Westhoek'.

The naming convention of the CASI-2 imagery is depicted below. In the Hands-on Lesson 10 these datasets will be used.

L1202rag10\_Wh :

- L12 = flight line number
- 02 = date, 02 indicates the year 2002
- rag = the image is radiometrically, geometrically and atmospherically corrected
- 10 = image pixel resolution; 10 indicates 1 m
- Wh = the image is a cut-out of the original flight track: (Wh = Westhoek)

### 12.2.3 PRE-PROCESSING

Naming extensions are added to the filenames as processing steps are performed on the data. Table 14 gives an overview of the different processing steps and their extensions used. The assignment of the extensions is done in the same order as the operations performed.

Extension	Image processing step
l	Look effect: correction for geometric look effects
p	Polished: noise removal of the spectral signatures
c	Cut-out: a number of bands with low signal to noise ratio were removed
ndvi	Normalized Difference Vegetation Index: ndvi image of the hyperspectral image
msk	Mask: mask image derived from the ndvi image
m	Masked: masked hyperspectral image using the ndvi derived mask

>> Table 14: The added extensions and their corresponding image pre-processing steps.

To obtain a workable set of hyperspectral images, some basic pre-processing of the raw data, as collected by the CASI-2 sensor, is needed. Standard pre-processing involves radiometric, geometric and atmospheric correction. The radiometric and geometric corrections were performed by the data providers. Atmospheric correction was performed by VITO using the ATCOR4 software.

The CASI-2 data was collected at 12-bit radiometric resolution. A radiometric correction is needed to convert the raw digital numbers from the sensors to a physical value, the radiance (1 Spectral Radiance Unit = 1 SRU = 1 nW cm<sup>-2</sup> sr<sup>-1</sup> nm<sup>-1</sup>).

As described in Section 2.1.2, the Bidirectional Reflectance Distribution Function (BRDF) is the reflectance of a target as a function of illumination geometry and viewing geometry. The BRDF depends on the wavelength and

is determined by the structural and optical properties of the surface. Due to the BRDF effect but also because of a possible overcorrection of non-NADIR pixels by the atmospheric correction algorithm, scan angle dependent geometric look-effects can be introduced for which should be corrected.

Hyperspectral images often contain noise due to the limited accuracy of sensor calibration, the measurement itself and the models used to perform the different data pre-processing steps. To compare the different spectra and subsequently classify the images, noise has to be removed.

### 12.2.4 VEGETATION MASK

Hyperspectral images contain a high degree of complexity due to the spectral variability in the scene. To reduce the complexity all redundant information has to be removed from the imagery. In this case all non-vegetation pixels can be regarded as redundant information and will be removed based on the 'Normalized Difference Vegetation Index' (NDVI). The NDVI is calculated as the normalized difference between the reflectance at the red part of the spectrum (at 676 nm) and the reflectance at the near-infrared (at 780 nm) part.

$$NDVI = \frac{\rho_{780} - \rho_{676}}{\rho_{780} + \rho_{676}} \quad (12.1)$$

By applying a minimum threshold level of 0.1, all vegetation pixels can be selected and a mask can be defined. This mask is applied to the hyperspectral image to remove all non-vegetation pixels. This process is illustrated in Figure 83. The threshold level was determined by the lowest NDVI value which was found for some sparse vegetation called *Festuca juncifolia* as observed during a field survey. In Figure 83, 'a' shows part of the hyperspectral image and 'b' the calculated NDVI. 'c' shows the mask image after applying the minimum threshold. This mask is finally applied to the hyperspectral image 'a' leaving the vegetation pixels only, as shown in 'd'.

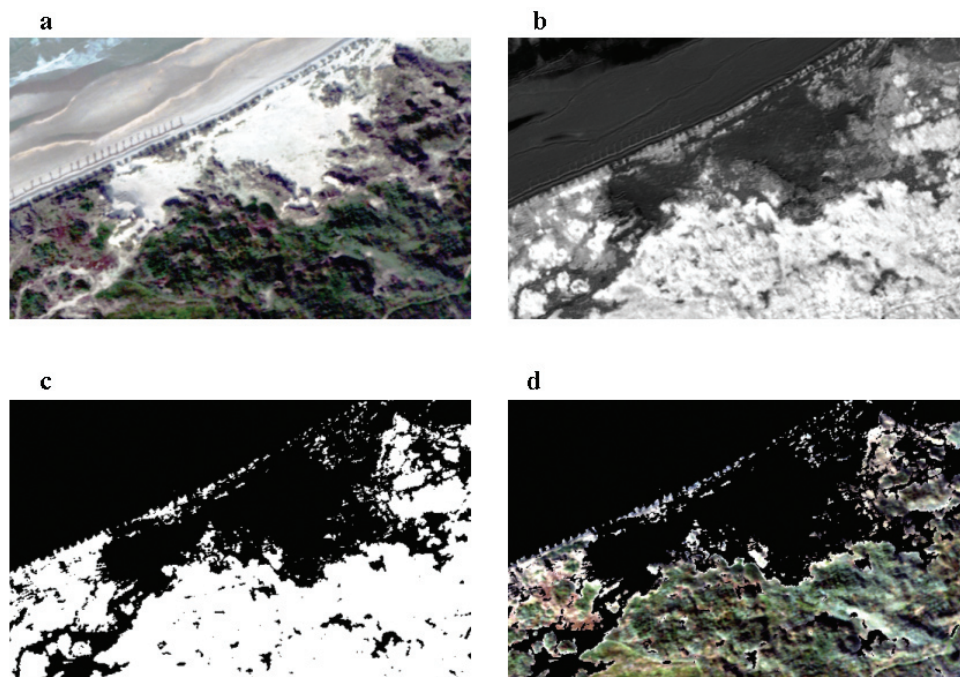


>> Figure 83. Reduction of the hyperspectral variability by applying a NDVI based mask for selecting vegetation pixels only. Where a = the hyperspectral image; b = NDVI image; c = mask; d = masked hyperspectral image.

### 12.2.5 FIELD SURVEY

During an extensive field campaign, performed by an experienced ecologist of the Institute for Nature Conservation (IN), the location of several hundreds of different vegetation plots were carefully measured using a dGPS. These locations are allocated to well known vegetation types and are used as references to specify the Regions Of Interest (ROIs). These ROIs are used for hyperspectral image classification and validation of the

## PART II: THEMATIC APPLICATIONS

classification result. The dGPS locations were available in 'shape'-format (SHP) and could be easily imported into ENVI. It is obvious that the geographic accuracy of the hyperspectral images must be very high in order to select the correct pixels according the measured polygons.

Figure 84 shows the hyperspectral track above 'De Westhoek' as an RGB image, using bands 14 (611.4 nm), 6 (520.6 nm) and 1 (412.9 nm) respectively. The ROIs collected during the field survey are indicated as coloured points. In this study a subset of the initial ROIs is used to perform a first classification. In total 13 ROIs were selected as listed in

Table 15. Because no dGPS positions were measured for the different grass vegetation types, these were manually selected from the imagery on the basis of field knowledge.



>> Figure 84: Part of the hyperspectral track above 'De Westhoek' nature reserve, indicating the different ROIs collected during field survey.

ROI name	Scientific name	English name	Dutch name	Nr ROIs	Nr Pixels	
Grass	A	-	Grass type A	Gras type A	5	133
	B	-	Grass type B	Gras type B	3	78
	C	-	Grass type C	Gras type C	2	42
	D	-	Grass type D	Gras type D	3	108
Ammoare	_Fix _Vit	Ammophila arenaria	Marram	Helm	4	106
					4	61
Hipprha	Hippophae rhamnoides	Sea buckthorn	Duindoorn	9	339	
Liguvul	Ligustrum vulgare	Wild privet	Wilde liguster	7	326	
Rubucae	Rubus caesius	European dewberry	Dauwbraam	3	51	
Salicin	Salix cinerea	Grey willow	Grauwe wilg	5	105	
Salirep	Salix repens	Creeping Willow	Kruipwilg	9	268	
Sambnig	Sambucus nigra	Elder	Gewone vlier	7	111	
Tortur	Tortula ruralis	Star moss	Duinsterretje	6	113	

>> Table 15: ROIs used for classification. In total 9 different ROIs were selected from the field survey. The grass type ROIs were manually selected from the imagery on the basis of field knowledge.

At the end of this section, a table with the different ROIs which represent the different vegetation types together with the scientific, common English and Dutch names, the number of ROIs initially collected in the field and the number of pixels in each vegetation type can be found.

### 12.2.6 SPECTRAL ANGLE MAPPER CLASSIFICATION

The classification algorithm applied in this case study uses of the ENVI build-in Spectral Angle Mapper (SAM), described in Section 9.1.4.1. This classification method takes as input a number of 'training classes' or reference spectra which, in this case study, are obtained from the imagery itself by means of Regions Of Interest (ROIs). The basis for these ROIs are the geographical locations of well known vegetation plots which are measured in the field by dGPS. The mean spectra of the different ROIs are used as reference spectra. The classification was performed after an MNF transform (see Section 9.1.1), reducing the spectral dimension. The first six MNF bands were used for classification. This number could be deduced from the eigenvalues plot (Figure 85) and after visual inspection of the remaining bands of the MNF image.

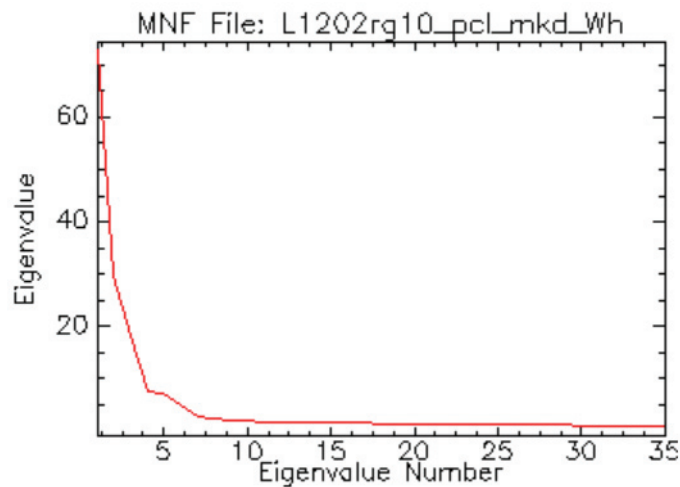


>> Figure 85: Plot of the eigenvalues obtained after MNF transform. The first 6 bands were used for SAM classification.

The result of the classification is shown in Figure 86. The obtained overall accuracy is 77%, with a Kappa coefficient of 0.75. The accuracy is calculated by the ENVI build-in confusion matrix (Table 16).

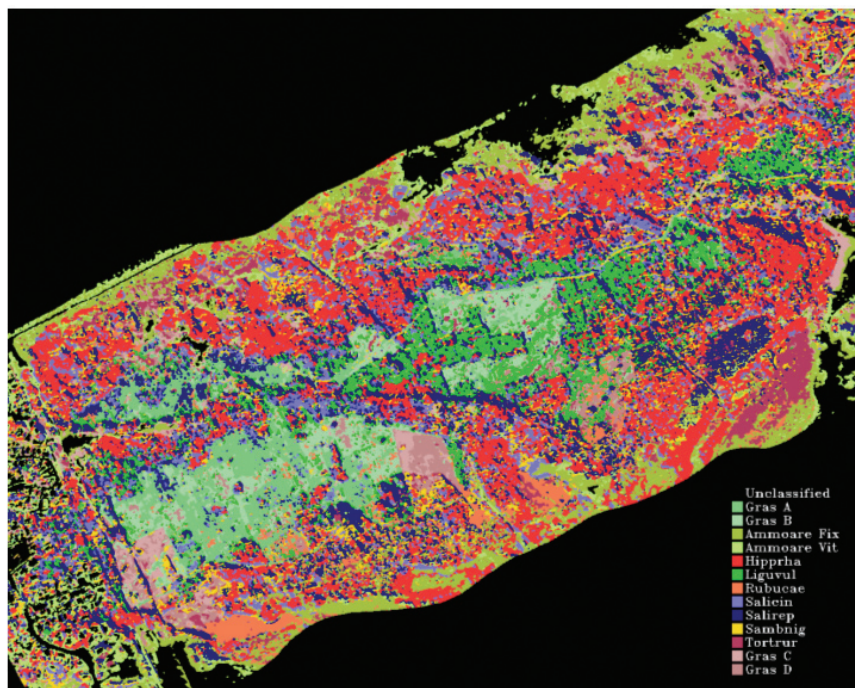
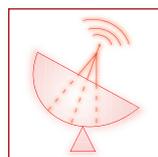


>> Figure 86: Classification result of 'De Westhoek' nature reserve, using 13 different ROIs (classes).

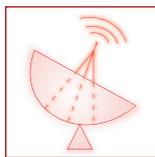
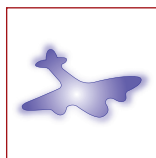


Class	Gras_A	Gras_B	Ammoare_Fix	Ammoare_Vit	Hipprha	Liguvul	Rubucac	Salicin	Salirep	Sambnig	Tortrur	Gras_C	Gras_D
Unclassified	0	0	5.26	0	0	0	0	0	0	0	0	0	0
Gras_A	100	16.67	0	0	0	11.76	0	0	0	15.38	0	0	0
Gras_B	0	83.33	0	0	0	5.88	0	0	0	15.38	0	0	0
Ammoare_Fix	0	0	63.16	21.74	0	0	0	0	0	0	0	0	0
Ammoare_Vit	0	0	15.79	73.91	0	0	0	0	0	0	0	0	0
Hipprha	0	0	0	0	82.35	0	0	42.31	11.54	0	0	0	0
Liguvul	0	0	0	0	0	58.82	0	0	0	0	0	0	0
Rubucac	0	0	0	0	0	0	100	0	0	0	0	0	0
Salicin	0	0	0	0	5.88	0	0	57.69	15.38	0	0	0	0
Salirep	0	0	0	0	11.76	20.59	0	0	73.08	0	0	0	0
Sambnig	0	0	5.26	4.35	0	0	0	0	0	53.85	0	0	0
Tortrur	0	0	10.53	0	0	0	0	0	0	7.69	57.14	4.17	0
Gras_C	0	0	0	0	0	0	0	0	0	7.69	7.14	87.50	0
Gras_D	0	0	0	0	0	2.94	0	0	0	0	35.71	8.33	100
TOTAL	100	100	100	100	100	100	100	100	100	100	100	100	100

>> Table 16: Confusion matrix calculated with ENVI. The obtained overall accuracy using 13 classes was 77% with a Kappa coefficient of 0.75.

The numbers in Table 16 indicate in percentage to which class the ground truth class pixels are attributed (classified). For example, from 100 pixels in the ground truth class Gras\_B, 16,67 are incorrectly classified as class Gras\_A, while 83,33 are correctly classified as class Gras\_B. From this confusion matrix, the error of omission, the error of commission, etc. can be calculated in order to evaluate the classification result.

This study is financed by the Belgian Science Policy Office and AWZ.



ROI name	Scientific name	English name	Dutch name	Nr ROIs	Nr Pixels
Alnus	<i>Alnus glutinosa</i>	European Alder	Zwarte els	1	22
Ammoare _Fix _Vit	<i>Ammophila arenaria</i>	Marram	Helm	9	306
Betula	<i>Betula pendula</i>	Silver Birch	Ruwe berk	4	61
Calaepi	<i>Calamagrostis epigejos</i>	Wood small-reed	Gewoon struisriet	2	59
Cratmon	<i>Crataegus monogyna</i>	Hawthorn	Meidoorn	3	78
Fraxinus	<i>Fraxinus exelsior</i>	Ash	Gewone es	5	54
General				1	36
Male	<i>Hippophae rhamnoides</i>	Sea buckthorn	Duindoorn	21	1007
Female	<i>Calamagrostis epigejos</i>	Wood small-reed	Duindoorn & Gewoon struisriet	6	227
& Calaepi	<i>Salix repens</i>	Creeping Willow	Duindoorn & Gewoon struisriet & Kruipwilg	10	434
& Salirep				10	285
Liguul	<i>Ligustrum vulgare</i>	Wild privet	Wilde liguster	2	218
Popualb	<i>Populus alba</i>	White poplar	Witte abeel	18	769
Popucan	<i>Populus canadensis</i>	Carolina poplar	Canadapopulier	1	52
Prunspi	<i>Prunus spinosa</i>	Blackthorn	Sleedoorn	1	15
Quercrob	<i>Quercus robur</i>	Common oak	Zomereik	1	51
Rosapim	<i>Rosa pimpinellifolia</i>	Burnet rose	Zomereik	3	26
Rosarub	<i>Rosa rubiginosa</i>	Sweet briar	Duinroosje	3	68
Rubucacae	<i>Rubus caesius</i>	European dewberry	Egelantier	2	34
Salicin	<i>Salix cinerea</i>	Grey willow	Dauwbraam	5	77
Salirep	<i>Salix repens</i>	Creeping Willow	Grauwe wilg	13	430
Sambnig	<i>Rubus caesius</i>	European dewberry	Kruipwilg	29	1255
Torttrur	<i>Sambucus nigra</i>	Elder	Dauwbraam	3	93
	<i>Tortula ruralis</i>	Star moss	Gewone vlier	18	603
			Duinsterretje	14	218

>> Table 17: Regions of interest collected during field survey.

---

---

---

---

## 13 REFERENCES

- Abrams, M.J., and Ashley, R.P., 1980, Alteration mapping using multispectral images - Cuprite Mining District, Esmeralda County, Nevada: U.S. Geological Survey Open File Report 80-367.
- Ackleson, S.G., 2003. Light in shallow waters: A brief research review. *Limnology and Oceanography*, 48(1): 323-328.
- Asner, G.P., Braswell, B.H., Schimel, D.S. and Wessman, C.A. 1998. Ecological research needs from multiangle remote sensing data. *Remote Sensing Environment* 63:155-165.
- Atzberger, C., [http://www.itc.nl/personal/atzberger/handouts\\_education\\_atzberger\\_remote\\_sensing.htm](http://www.itc.nl/personal/atzberger/handouts_education_atzberger_remote_sensing.htm)
- Babin, M., Morel, A., Fournier-Sicre, V., Fell, F. and Stramski, D., 2003a. Light scattering properties of marine particles in coastal and open ocean waters as related to the particle mass concentration. *Limnology and Oceanography*, 28(2): 843-859.
- Babin, M., Morel, A. and Gentilli, B., 1996. Remote sensing of sea surface sun-induced chlorophyll fluorescence: consequences of natural variations in the optical characteristics of phytoplankton and the quantum yield of chlorophyll *a* fluorescence. *International Journal of Remote Sensing*, 17: 2417-2448.
- Babin, M., Stramski, D., Ferrari, G.M., Claustre, H., Bricaud, A., Obolensky, G. and Hoepffner, N., 2003b. Variations in the light absorption coefficients of phytoplankton, nonalgal particles and dissolved organic matter in coastal waters around Europe. *Journal of Geophysical Research*, 108(C7): 3211, doi:10.1029/2001JC000882.
- Berk, A., Bernstein, L. S., Anderson, G.P., Acharya, P. K., Robertson, D.C., Chetwynd, J. H., and Adler-Golden, S. M., 1998. MODTRAN cloud and multiple scattering upgrades with application to AVIRIS. *Remote Sens. Environ.*, 65: 367-375.
- Boardman, J.W. and Kruse, F. A., 1994. Automated spectral analysis: a geological example using AVIRIS data, north Grapevine Mountains, Nevada. In: Proceedings ERIM Tenth Thematic Conference on Geologic Remote Sensing, Michigan, I-407 – I-418.
- Boardman, J.W., Kruse, F.A. and Green, R.O., 1995. Mapping target signatures via partial unmixing of AVIRIS data: in Summaries, 5<sup>th</sup> Airborne Earth Science Workshop, JPL Publication 95-1: 23-26.
- Breuer, M., Albers, J., 2000. Geometric correction of airborne whiskbroom scanner imagery using hybrid auxiliary data. *International Archives of Photogrammetry and Remote Sensing*, XXXIII (B3): 93-100.
- Broxmeyer C., 1964. *Inertial Navigation Systems*. McGraw-Hill Book Co., New York, N.Y., 254.
- Bricaud, A., Babin, M., Morel, A. and Claustre, H., 1995. Variability in the chlorophyll-specific absorption coefficients of natural phytoplankton: Analysis and parameterization. *Journal of Geophysical Research*, 100(C7): 13321-13332.
- Buiteveld, H., Hakvoort, J.M.H. and Donze, M., 1994. The optical properties of pure water. In: J.S. Jaffe (Editor), *Proceedings of Ocean Optics XII*. SPIE, 174-183.
- Burrough, P.A. and R. A. McDonnell. 1998. *Principles of Geographical Information Systems*. Oxford: Oxford University Press.
- Chen, J.Y and Reed, I.S., 1987. A detection algorithm for optical targets in clutter. *IEEE Trans. On Aerosp. Electron. Syst.*, V. AES-23 No.1.

- Congalton, R.G. 1991. A review of assessing the accuracy of classifications of remotely sensed data. *Remote Sensing of Environment* 37(1): 32-46.
- Dekker, A. G., V. E. Brando, J. M. Anstee, N. Pinnel, T. Kutser, E. J. Hoogenboom, S. Peters, R. Pasterkamp, R. Vos, C. Olbert, and T. J. M. Malthus. 2001. Imaging Spectrometry of Water, 307-359. In F. D. Van der Meer and S. M. de Jong [eds.], *Imaging Spectrometry*. Kluwer.
- Doxaran, D., J.-M. Froidefond, S. Lavender, and P. Castaing. 2002. Spectral signatures of highly turbid waters. Application with SPOT data to quantify suspended particulate matter concentrations. *Remote Sensing of the Environment* 81: 149-161.
- Drury, S., 1993: *Image interpretation in geology* 2<sup>nd</sup> Edition – Chapman & Hall, London
- Duda, R.O., Hart, P.E., and Stork, D.G., 2001. *Pattern Classification*, 2nd Edition. Wiley, 2001.
- El-Rabbany, A., 2002. *Introduction to GPS: The Global Positioning System*. Artech House Publishers, ISBN 1-8053-183-0, 196 pages.
- Gao, B.-C. & Davis, C. O., 1997. Development of a line-by-line-based atmosphere removal algorithm for airborne and spaceborne imaging spectrometers, in *Imaging Spectrometry III*, Eds. Michael R. Descour, Sylvia S. Shen, *Proceedings of SPIE Vol. 3118*, 132-141.
- Gao, B.-C., Montes, M. J., Ahmad, Z. and Davis, C. O., 2000. Atmospheric Correction Algorithm for Hyperspectral Remote Sensing of Ocean Color from Space, *Applied Optics*, 39(6): 887-896.
- Goetz, A.F.H., 1992. Principles of narrow band spectrometry in the visible and IR: instruments and data analysis. In: F. Toselli & J. Bodechtel (Eds.) *Imaging Spectroscopy: Fundamental and Prospective Applications*. Dordrecht, Kluwer Academic Publishers, 21-32
- Gons, H. J., M. Rijkeboer, and K. G. Ruddick. 2005. Effect of a waveband shift on chlorophyll retrieval from MERIS imagery of inland and coastal waters. *Journal of Plankton Research* 27: 125-127.
- Gordon, H.R., Brown, O.B. and Jacobs, M.M., 1975. Computed relationships between inherent and apparent optical properties of a flat, homogeneous ocean. *Applied Optics*, 14: 417-427.
- Gower, J.F.R., Doerffer, R. and Borstad, G.A., 1999. Interpretation of the 685 nm peak in water-leaving radiance spectra in terms of fluorescence, absorption and scattering, and its observation by MERIS. *International Journal of Remote Sensing*, 20(9): 1771-1786.
- Green, A.A., Berman, M., Switzer, P. and Craig, M.D., 1988. A transformation for ordering multispectral data in terms of image quality with implications for noise removal. *IEEE Transaction on Geoscience and Remote Sensing*, 26(1): 65-74.
- Haltrin, V.I. and Kattawar, G., 1993. Self-consistent solutions to the equation of transfer with elastic and inelastic scattering in oceanic optics: 1. model. *Applied Optics*, 32(27): 5356-5367.
- Harsanyi, J.C. and Chang C.I., 1994. Hyperspectral image classification and dimensionality reduction: An orthogonal subspace projection approach. *IEEE Transactions on Geoscience and Remote Sensing*, V. 32: 779-785.
- Hofmann-Wellenhof, B., Lichtenegger, H., Collins, J., 2001. *Global Positioning System: Theory and Practice*. SpringerWienNewYork, ISBN 3-211-83534-2. 382 pages.

- Hoge, F.E., Vodacek, A. and Blough, N.V., 1993. Inherent optical properties of the ocean: Retrieval of the absorption coefficient of chromophoric dissolved organic matter from fluorescence measurements. *Limnol. Oceanogr.*, 38(7): 1394-1402.
- Hook, S.J., 1990, The combined use of multispectral remotely sensed data from the short wave infrared (SWIR) and thermal infrared (TIR) for lithological mapping and mineral exploration: Fifth Australasian Remote Sensing Conference, Proceedings, Oct., 1990, vol.1, p. 371-380.
- Kirk, J.T.O., 1981. Monte Carlo study of the underwater light field in, and relationships between optical properties of, turbid yellow waters. *Australian Journal of Freshwater Research*, 32: 517-532.
- Kirk, J. T. O. 1996. Light and photosynthesis in aquatic ecosystems. Cambridge University Press.
- Kruse, F. A., Lefkoff, A.B., Boardman, J.B., Heidebrecht, K.B., Shapiro, A.T., Barloon, P.J., and Goetz, A.F.H., 1993. The spectral Image Processing System, (SIPS) – Interactive Visualization and Analysis of Imaging Spectrometer data. *Remote Sensing of Environment*, 44: 145-163.
- Lillesand, T.M., Kiefer, R.W., Chipman, J.W, 2004. Remote Sensing and Image interpretation, 5<sup>th</sup> edition. Wiley and sons.
- Mallat, S., 1998. A Wavelet Tour of Signal Processing. San Diego: Academic Press, 1998.
- Mobley, C.D., 1994. Light and water: radiative transfer in natural waters. Academic Press, London.
- Morel, A., 1974. Optical properties of pure water and sea water. In: N.G. Jerlov and E. Steeman-Nielsen (Editors), *Optical aspects of Oceanography*. Academic Press, 1-24.
- Morel, A., and D. Antoine. 2000. MERIS Algorithm Theoretical Basis Document 2.9: Pigment index retrieval in case 1 waters, 26. Laboratoire de Physique et Chimie Marines.
- Morel, A., and B. Gentili. 1996. Diffuse reflectance of oceanic waters. III. Implications of bidirectionality for the remote sensing problem. *Applied Optics* 35: 4850-4862.
- Morel, A. and Maritorena, S., 2001. Bio-optical properties of oceanic waters: a reappraisal. *Journal of Geophysical Research*, 106(C4): 7163-7180.
- Morel, A. and Prieur, L., 1977. Analysis of variations in ocean color. *Limnology and Oceanography*, 22(4): 709-722.
- Mueller, J. L., G. S. Fargion, and C. R. McClain [eds.]. 2003. Ocean optics protocols for satellite ocean color sensor validation. NASA.
- Nechad, B., V. De Cauwer, Y. Park, and K. Ruddick. 2003. Suspended Particulate Matter (SPM) mapping from MERIS imagery. Calibration of a regional algorithm for the Belgian coastal waters. MERIS user workshop, 10-13th November 2003. European Space Agency.
- Nieke J., 1997. Imaging spaceborne and Airborne Sensor Systems in the Beginning of the Next Century. In: *Proceedings of The European Symposium on Aerospace Remote Sensing (IEEE)*, 22-26 Sept. 1997, London, UK; Conference on Sensors, Systems and Next Generation Satellites III; Paper-No.: 3221-71
- Philpot, W.D., 1987. Radiative transfer in stratified waters: a single-scattering approximation for irradiance. *Applied Optics*, 26: 4123-4132.

- O'Reilly, J. E., S. Maritorena, B. G. Mitchell, D. A. Siegel, K. L. Carder, S. A. Garver, M. Kahru, and C. McClain. 1998. Ocean color chlorophyll algorithms for SeaWiFS. *Journal of Geophysical Research* 103: 24937-24953.
- Qu, Z., Goetz, A.F.H, Heidebrecht, K.B., 2000. High-Accuracy Atmosphere Correction for Hyperspectral Data (HATCH). JPL AVIRIS Proceedings.
- Ouillon, S., P. Forget, J. M. Froidefond, and J. J. Naudin. 1997. Estimating suspended matter concentrations from SPOT data and from field measurements in the Rhone River plume. *Marine Technology Society* 31: 15-20.
- Ranson, K.J., Irons, J.R. and Williams, D.L. 1994. Multispectral bidirectional reflectance of northern forest canopies with the Advanced Solid-State Array Spectroradiometer (ASAS). *Remote Sensing Environment* 47: 276-289.
- Richards, J.A., 1999. *Remote Sensing Digital Image Analysis: An Introduction*, Springer-Verlag, Berlin, Germany, 240.
- Richter, R., 1996. A spatially adaptive fast atmospheric correction algorithm. *Int. J. Remote Sensing*, 17: 1201-1214.
- Richter, R. and Schläpfer, D., 2002. Geo-atmospheric processing of airborne imaging spectrometry data. Part 2: atmospheric/topographic correction, *Int. J. Remote Sensing*, 23: 2631-2649.
- Ruddick, K., G. Lacroix, Y. Park, V. Rousseau, V. De Cauwer, and S. Sterckx. 2005 (submitted). Overview of Ocean Colour: theoretical background, sensors and applicability for the detection and monitoring of harmful algae blooms (capabilities and limitations). Real-time coastal observing systems for ecosystem dynamics and harmful algal blooms. UNESCO Monographs on Oceanographic Methodology Series.
- Stocker, A., Reed, I.S. and Yu, X, 1990. Multidimensional signal processing for electrooptical target detection. *Proceedings SPIE Int. Soc. Opt. Eng.*, V. 1305.
- Stumpf, R. P., and J. R. Pennock. 1989. Calibration of a general optical equation for remote sensing of suspended sediments in a moderately turbid estuary. *Journal of Geophysical Research* 94: 14363-14371.
- Sugihara, S., Kishino, M. and Okami, N., 1984. Contribution of Raman scattering to upward irradiance in the sea. *Journal of the Oceanographic Society of Japan*, 40: 397-404.
- Van der Meer, F., de Jong, S.M. and Bakker, W., 2001. *Imaging Spectrometry: Basic Analytical Techniques. Basic Principles and Prospective Applications*, Eds. F.D. Van der Meer, S.M. de Jong, Kluwer Academic Publishers, ISBN 1-4020-0194-0.
- Vasilkov, A.P., Burenkov, V.I. and Ruddick, K.G., 1999. The spectral reflectance and transparency of river plume waters. *International Journal of Remote Sensing*, 20(13): 2497-2508.
- Vermote, E.F., Tanre, D., Deuzé, J.L., Herman, M., and Morcrette, J.J., 1997. Second simulation of the satellite signal in the solar spectrum, 6S: An overview. *IEEE Trans. Geosc. Remote Sens.* 35(3): 675-686.
- Willekens, A., Verwimp, R. and Van Orshoven, J, 2001. *Introduction to Satellite Remote sensing Module 1: Basic Concepts*. Spatial Applications Division, K.U. Leuven Research and Development.

## 14 ANNEX

### 14.1 ASD2 Spectroradiometer: IRRADIANCE – measurements

#### 14.1.1 EQUIPMENT

The following equipment is also necessary to perform the measurements:

- Spectralon (+ tripod)
- Pistol (with RCR-fore optic)

**Turn on** the instrument, allow it to warm up for at least 15 to 30 minutes. **Connect** the parallel and power cable securely to the laptop and ASD. **Turn on** the computer, check if date and time of PC is correct. **Launch** the instrument software → **High Contrast RS<sup>3</sup>**

#### 14.1.2 SETUP

Open the Spectrum Save screen by selecting **Alt S** or **Control\Spectrum Save** on the toolbar. Enter the following details :

		Examples
Path name	C:\FR\...	C:\ASD\Coast
Base name	... → filename	
Starting spectrum number	000 → file-extension	
Number of files to save	Nnn	120
Interval between saves	hh:mm:ss	1 minute
Comment	...	

Select **OK** to accept details and close the window.

Open the **Control\Adjust Configuration** on the toolbar (or **Alt C + C**)

	Indoors	Outdoors
Fore optic	RCR	RCR
Spectrum	30	40
DC (Dark Current)	25	25
WR (White Reference)	30	40
Check <b>Absolute Reflectance</b> if using a calibrated Spectralon panel.		

Select **OK** to accept details and close the window.

Follow the instructions in section 14.1.3 to begin collecting data.

#### 14.1.3 MEASUREMENTS

1. Optimize : Point the fore optic at the white reference and press the **OPT**-button (or **CTRL-O**).
2. After optimizing and collecting a dark current the graph will display measurements in Raw DN and plot them against wavelength in nm.
3. Select **F9** or the **RAD**-button (with RCR) to collect an automatic dark current measurement and to get an irradiance spectrum. To display the **irradiance** measurement point the irradiance fore optic at the target.
4. Press the spacebar to start saving the spectrum data. The instrument beeps when the data is saved.

### 14.2 ASD2 Spectroradiometer: REFLECTANCE – measurements

#### 14.2.1 EQUIPMENT

The following equipment is also necessary to perform the measurements :

- Spectralon (+ tripod)
- Pistol

**Turn on** the instrument and allow it to warm up for at least 15 to 30 minutes. **Connect** the parallel and power cable securely to the laptop and ASD.

**Turn on** the computer, check if date and time of PC is correct.

**Launch** the instrument software → **High Contrast RS<sup>3</sup>**

## 14.2.2 SETUP

Open the Spectrum Save screen by selecting **Alt S** or **Control\Spectrum Save** on the toolbar. Enter the following details :

		Examples
Path name	C:\FR\...	C:\ASD\Coast
Base name	... → filename	
Starting spectrum number	000 → file-extension	
Number of files to save	Nnn	1
Interval between saves	hh:mm:ss	00:00:00
Comment	...	

Select **OK** to accept details and close the window.

Open the **ControlAdjust Configuration** on the toolbar (or **Alt C + C**)

	Indoors	Outdoors
Fore optic	Bare Fiber	Bare Fiber
Spectrum	10	40
DC (Dark Current)	25	25
WR (White Reference)	10	40
Check <b>Absolute Reflectance</b> if using a calibrated Spectralon panel.		

Select **OK** to accept details and close the window.

## 14.2.3 MEASUREMENTS

1. Optimize : Point the bare fiber or fore optic at the spectralon and press the **OPT**-button (or **CTRL-O**). After optimizing and collecting a dark current the graph will display measurements in raw DN and plot them against wavelength in nm.
2. White Reference : Point the fiber at the spectralon and press the **WR**-button (or **F4**). Selection of **REFLECTANCE** appears, the curve should be a horizontal line with value of 1. Save (press **spacebar** to save)
3. Measure target, wait for stable curve + save. Repeat this step (at least) 3 times
4. Measure spectralon as target and save.

Repeat step 2 to 4 for all points to measure. Don't forget to **save the result** by pressing the **spacebar**.

If during the measurements a **saturation** occurs, then **optimize** again and continue with the steps as described above.

## 14.3 GER1500 Spectroradiometer: REFLECTANCE – measurements

### 14.3.1 EQUIPMENT

The spectral range of the GER 1500 is from 350 nm to 1050 nm.

The following equipment is necessary to do the measurements :

- Spectralon (+ tripod)
- 8° fore optic
- Communication-cable

## 14.3.2 SETUP

- Power
- Menu → AVG x : the number of scans to be averaged is  $2^x-1$ , e.g. '4' → averages 8 scans
- Menu → INSTP mx : m : integration mode = A → automatic mode = blank → manual mode  
x : integration speed =  $5 \times 2^{x-1}$  ms  
e.g. 'A5' → integration speed is adjusted prior to a scan  
5' → integration speed : 80ms
- Menu → TRG cccc : **BOTH** : the trigger activates the laser when depressed and begins the acquisition when released  
SCAN : the trigger does not activate the laser when depressed but begins an acquisition when released  
LSR : the trigger activates the laser when depressed but does not begin an acquisition when released.
- Menu → Optic x : 1 : Standard, 8° FOV → reflectance  
2 : Fiber Optic Option  
3 : 15° FOV → reflectance  
4 : Cosine Receptor + 8° FOV → irradiance
- Menu → MEM xxx : the Memory Slot that stores the acquisition.  
Allowable value : 1 to 481

The standard parameters are marked in **Bold** .

## 14.4 MICROTUPS II SUN PHOTOMETER - measurements

### 14.4.1 BEFORE YOU LEAVE THE OFFICE

*Check if the GMT time is correct! Furthermore it is recommended to save the name, coordinates, altitude and pressure of the location where you will perform the measurements. You can still manually set the coordinates, altitude and pressure of the location when you're in the field. However, without a PC you can't assign a name to the location.*

#### 14.4.1.1 Switching on

To switch the instrument on, press the **ON/OFF button** on the bottom left hand side of the keypad. Keep the sensor heads covered with the black panel during the hardware setup and initialisation process. The instrument will beep, and start making dark current measurements. During this process the instrument should be kept in the shadow.

The opening menu will give the following message:

```
RDY Sitename... ID=1  
DDMMYY HH:MM:SS
```

Where sitename is the name of the site which has been pre-programmed into the Microtops or MANUAL in case the site is not pre-programmed

#### 14.4.1.2 Setting the time and date

It is recommended that you use GMT !!!! (for current GMT time check <http://wwp.greenwichmeantime.com/>)

Press the menu button 3 times, navigating past the menus **CLOCK, ADJUST CLOCK**, and then entering the **TIME AND DATE ZONE**. Use the right and left arrow keys to navigate along the date and time line, and then use the up and down keys to change these parameters accordingly. Press **ENTER** when the time is set correctly.

Press **ESCAPE** twice to return to the front screen.

### 14.4.1.3 Connecting the sun photometer to the computer and save location parameters Optional (recommended)

This is necessary for the setting up of a new site within the instrument parameter settings, and later for downloading your scans to the PC.

1. Connect to the serial port (COM 1) of your computer using the cable provided.
2. The jack end should be placed into the socket at the left-hand side of the Microtops itself.
3. Switch the sun photometer on.
4. Launch the Microtops Software (you will need to install this on your computer using the diskettes provided).
5. Navigate to the TOOLS menu, then choose Change Instrument Locations
6. Enter a new site name into one of the 6 site boxes.
7. Enter the site position in decimal degrees +N and +E. Accuracy to a 5 minute angle is adequate for both latitude and longitude.
8. Enter the height in metres above sea level in the final column.
9. Enter the pressure with an accuracy of about 20 mB.
10. Press SET. The parameter will now be sent to the instrument and will appear as a new site under the site location options.

## 14.4.2 COLLECTING MEASUREMENTS IN THE FIELD

### 14.4.2.1 Switching on

See Section 14.4.1.1.

### 14.4.2.2 Set the location

There are two options to set the location:

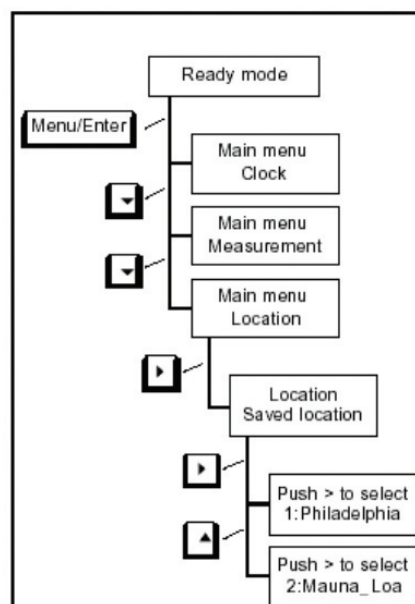
2 options :

#### a. you have saved the location to the Microtops beforehand (see 14.4.1.3)

It is necessary to program the head to the new site location.

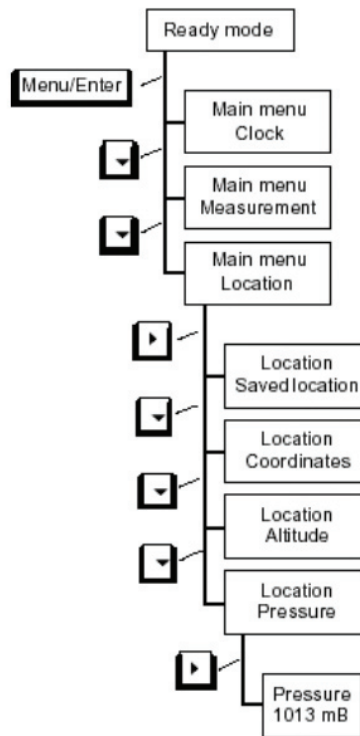
Press the [MENU/ENTER] button once, followed by the downwards pointing arrow cursor 2 times. This will display the LOCATION menu option. Then press the right arrow or [MENU/ENTER] to select this menu, and proceed through the **Saved Location** menu by pressing the right cursor again or [MENU/ENTER] .

Now scroll through the site options (there will be 6 in total), using the upwards cursor until you reach the desired site. To select this site, press the right cursor. Then press the ESCAPE button until you return to the main screen. **Your site name should now be displayed on the front screen.**



## b. the coordinates, pressure, altitude was not set beforehand

Press the [MENU/ENTER] key to enter the menu mode. Followed by the downwards pointing arrow cursor 2 times. This will display the LOCATION menu option. Press the right arrow cursor (or MENU/ENTER) to select this menu.



### Coordinates

Press the downwards pointing arrow once, select **location coordinates** by pressing the right cursor or [MENU/ENTER].

- Coordinates -  
40° 03' N 75° 08' W

The selected (underlined) item can be incremented/decremented with ^ and v keys and the selection can be changed with < and < keys.

Press the [MENU/ENTER] key to save the coordinates.

### Altitude

Press the downwards pointing button, select **location coordinates** by pressing the right cursor or [MENU/ENTER].

The selected (underlined) item can be incremented/decremented with ^ and v keys and the selection can be changed with < and < keys.

Press the [MENU/ENTER] key to save the coordinates.

### Pressure

Press the downwards pointing button, select **location coordinates** by pressing the right cursor or [MENU/ENTER].

The selected (underlined) item can be incremented/decremented with ^ and v keys and the selection can be changed with < and < keys.

Press the [MENU/ENTER] key to save the coordinates

Then press the ESCAPE button until you return to the main screen. **MANUAL should now be displayed on the front screen.**

### 14.4.2.3 Collecting measurements

1. The Microtops II is intended for use in cloud free conditions. Before deployment, please be sure there are no thin cirrus (or any other type of) clouds in front of the sun.
2. Open the optics cover completely.
3. Using the "Sun Target," aim the instrument at the sun. It is recommended to use a tripod to keep the instrument as steady as possible. See Figure 87.
4. With the sun in the centre of the "Sun Target," press the [SCAN/ESCAPE] button to make a measurement.
5. Make fourteen more measurements immediately. This is essential so that in post processing the data not pointed correctly at the sun can be removed.
6. Turn off the instrument using the [ON/OFF] button.
7. Be sure to turn the instrument off and on between each set of fifteen measurements. This helps account for temperature changes, as the dark current value is measured each time the Microtops II is turned on.



>> Figure 87: MICROTOPS II sun photometer and the sun target.

### 14.4.3 DOWNLOADING THE DATA TO PC

Once you have collected all measurements of one day, you will need to download the data and clear the memory of the sun photometer before the next day.

Note that the default installation of the Microtops software creates a database called data.dbf in the same folder as the program file. All data downloaded from the Microtops is appended to this file.

Before you download the data from the Microtops the file data.dbf **may not exist** on your PC or else the download will fail. **If the database does not exist, the program will prompt for it to be created.**

1. Connect the sun photometer to the serial port (COM 1) of your computer using the cable provided. The jack end should be placed into the socket at the left-hand side of the Microtops.
2. Switch the sun photometer on.
3. Check the [OPTIONS] [COMMUNICATIONS] menu, set the Baud Rate and the COM Port to Auto detect.
4. Click Download. The scans will be downloaded into the standard microtops DATA.DBF database which is located on C:\PROGRAM FILES\SOLAR LIGHT CO\MICROTOPS II ORGANIZER\DATA.DBF. Note that a DATA.MDX file is also created which is used by the Microtops software. All measurements of all locations are downloaded.

5. Provide a description for the database entry (e.g. site name).
6. Exit from the Microtops software before opening the data.dbf file (the database is empty until the program has been terminated).
7. Copy the data.dbf to an other folder to prevent overwriting your data and remove then it from the default directory to avoid problems when using different Microtops instruments.
8. The DBF file can be opened in Excel (Data → import data)
9. Clear the memory. This can be performed by selecting the CLEAR BUFFER command in the TOOLS menu. The user will be prompted to confirm that all data will be lost. Only perform this operation if you have already downloaded the data from the Microtops II to your computer.

## **14.5 GER1500-measurements**

### **14.5.1 STAND-ALONE MEASUREMENTS**

1. Remove plastic hood from the fore optic.
2. Use ▼ or ▲ to obtain the **REF xxx** message on the display. Focus the instrument on the Spectralon and take 10 reference scans to warm up the instrument.
3. Press EDIT button, set the memory location to **MEM 1** by pressing ▼ and press EDIT button again.
4. Use ▼ or ▲ to obtain the **REF xxx** message on the display. Focus the instrument on the Spectralon and take a reference scan.
5. Use ▼ or ▲ to obtain the **TAR xxx** message on the display. Focus the instrument on the target and take at least 3 target scans.
6. Focus the instrument on the Spectralon and take a target scan.
7. Repeat step 4 to 6 for all point to measure.
8. Turn the instrument Power **Off**

Downloading Data :

- The decimal symbol of the computer has to be a "." point !
- Connect the COM-cable between COM2 of the instrument and COM1 of the computer.
- Turn the instrument Power On.
- Start GER1500-software.
- Click File , first choose Data Options and than Format
- Choose Sig-file and Click OK
- Click Control in the main menu and choose Read Memory
- Click New File Name
- Choose drive, directory and File Base (= filename) to store the data. Click OK
- You can change the first and last scan to be read. Click OK
- A data file is created for each target scan.
- Click File and Exit
- You can import the data files in an Excel sheet .

**Attention :**

- ! No files are created for the reference scans !
- ! The data files are renumbered (file-extensions) !
- >>>Make sentences.

### **14.5.2 COMPUTER MEASUREMENTS**

The decimal symbol of the computer has to be a "." point !

1. Connect the COM-cable between COM2 of the instrument and COM1 of the computer.
2. Turn the instrument Power On.
3. Start GER1500-software.
4. Click File , first choose Data Options and than Format

5. Choose Sig-file and Click OK
6. Click File and click New
7. choose drive, directory and File Base (= filename) to store the data. Click OK
8. Click Control in the main menu and choose Measurement
9. Remove plastic hood from the fore optic.
10. To warm up the instrument : Focus the instrument on the Spectralon and take 10 Reference scans by clicking 10 times Reference .
11. Take a Reference scan by focusing on the spectralon and Click Reference
12. Focus the instrument on the target and take at least 3 target scans by clicking 3 times Target
13. Focus the instrument on the spectralon and take a target scan by clicking Target
14. Repeat step 11 to 13 for all points to measure.
15. Click File and Exit
16. You can import the data files in an Excel sheet .

**Attention :**

- ! No files are created for the reference scans !

## **14.6 Trimble GeoXT GPS–measurements**

### **14.6.1 EQUIPMENT**

- Trimble GeoXT1 – professional
- Trimble GeoXT2 – standard

### **14.6.2 GPS MEASUREMENTS (POINTS)**

1. Start **TerraSync** software.
2. Control in the **Status** window the number of satellites.
3. Activate the **Data** window and choose **New File**.
4. In the Create New Data File window choose :  
 File type : **Rover**  
 File Name : xxxxxx  
 Dictionary Name : **Punten**
5. Click **Create**
6. In the Choose Feature window, **Collect** is indicated, choose **Punt** and click **Create**
7. Write a **comment**, wait for about **20 soundings** and click **OK** , the coordinates of the point are now saved.
8. Repeat step 6 and 7 for all points to measure.
9. Click **Close** and click **Yes** to the question “Close this file, are you sure”
10. Close the TerraSync software by clicking the **X** symbol in the upper right corner of the window.

Instead of putting the measurements in a new data file you can append the measurements in an existing data file or update an existing measurement in an existing data file: pto.

**Attention :**

Touch the **F2-key** to backup the RAM to the harddisk !

### **14.6.3 TRIMBLE GEOXT GPS–MEASUREMENTS WITH REAL-TIME CORRECTION**

#### **14.6.3.1 Equipment**

- Trimble GeoXT1 – professional
- Trimble GeoXT2 – standard
- GSM Sony Ericsson – T610

!!! If you don't use the Bluetooth-function, then it is best to disable it to save energy.

### 14.6.2.2 Activate Bluetooth on GSM

Navigation buttons on GSM :

- Left button --- → select
- Right button --- → Meer
- Joystick in the middle → navigation in the menu's or Setup-menu if pressed

1. Switch on GSM + enter PIN-code
2. Activate Bluetooth :  
select MEER + Bluetooth AAN  
→ if the activation is ok then the Bluetooth symbol appears on top of display

### 14.6.3.3 Activate Bluetooth on Trimble

1. Switch on Trimble
2. Activate Bluetooth :  
F4 – Bluetooth manager  
Under the Enable – tab :
  - v - Enable Bluetooth
  - v - Always Authenticate
  - v - DiscoverableUnder the Scan Devices – tab :
  - SCAN - this might take a while→ the GSM will be found, only the line with the GSM-symbol must be kept, the others may be removed.
3. Close the Bluetooth Manager by pressing OK

### 14.6.3.4 Preparations of the GPS measurements

1. Start TerraSync software.
2. Select SETUP in the upper left corner
3. Select Real-time Settings  
Choice 1: External Source (without Realtime correction → select integrated WAAS)  
Choice 2: Uncorrected GPS  
Real-time Age limit: 1 min
4. In this window you can select the properties of the External Source by clicking the symbol behind the  
Choice1 : External Source  
Type: VRS → select this one  
Single Base  
Connection method: Direct dial  
Modem type: Sony 1  
Phone number: 022908326 → nearest station  
022908325 → virtual station  
Connection control: Manual
5. Close the setup-windows until you are back on the Options-menu (Setup)
6. Start / Stop the real-time connection by clicking Ext Source in the middle of the screen\_

Once you are connected you can start the GPS-measurements according the regular procedure (14.6). If you are finished with the measurements don't forget to disable Bluetooth on the GSM and the GeoExplorer to save power.

### 14.6.3.5 Checking the status of the real-time connection

1. Select STATUS in upper left corner
2. Select Real-time

---

---

---

---

3. If (on the right) SUMMARY is selected you get the following info :

External source            waiting/in use

If External is selected you get the following additional info :

Correction type

Connection up-time

Data received

Last correction

## **14.6.4 TRIMBLE GEOXT GPS–MEASUREMENTS – TRANSFER RESULTS**

### **14.6.4.1 Software**

To be able to transfer the results it is necessary to have the following software installed :

- GPS Pathfinder 3.0 (or higher)

- Microsoft ActiveSync → can be downloaded from <http://www.microsoft.com/windowsmobile/resources/downloads/handheldpc/default.aspx>

### **14.6.4.2 Transfer results**

1. Connect the Trimble GeoXT to your computer with the COM-port and switch it on. The ActiveSync-software will automatically detect the device.
2. Open GPS Pathfinder and select (or create) a project. A blank screen will appear.
3. Select Utilities → Data transfer ...

---

---

---

---

---

## ACRONYMS

A/D	Analogue to Digital
ACORN	Atmospheric CORrection Now
ADC	Analogue-to-Digital Converter
AIGLLC	Analytical Imaging and Geophysics Limited Liability Company
AIS	Airborne Imaging Spectrometer
AISA	Airborne Imaging Spectrometer
AOT	Aerosol Optical Thickness
APEX	Airborne Prism EXperiment
ARES	Airborne Reflective Emissive Spectrometer
ASD	Analytical Spectral Devices
ASTER	Advanced Spaceborne Thermal Emission and Reflection Radiometer
ATCOR	ATmospheric CORrection
ATREM	ATmospheric REMoval
AVHRR	Advanced Very High Resolution Radiometer
AVIRIS	Airborne Visual and Infrared Imaging Spectrometer
BOA	Bottom-Of-Atmosphere
BRDF	Bidirectional Reflectance Distribution Function
BRF	Bidirectional Reflectance Factor
C/A	Coarse/Acquisition
CASI	Compact Airborne Spectrographic Imager
CCD	Charge Coupled Device
CDOM	Coloured Dissolved Organic Matter
CHRIS	Compact High Resolution Imaging Spectrometer
CNES	Centre National d'Études Spatiales
DAIS	Digital Airborne Imaging Spectrometer
DC	Direct Current
DEM	Digital Elevation Model
d-GPS	differential Global Positioning System
DLR	Deutschen Zentrum für Luft- und Raumfahrt
DN	Digital Number
DTM	Digital Terrain Model
DWT	Discrete Wavelet Transform
EAN	Equal Area Normalization
EGNOS	European Geostationary Navigation Overlay Service
EMR	ElectroMagnetic Radiation
ENVI	ENvironment for Visualizing Images
EO-1	Earth Observing 1 (mission)
EPS	Environmental Protection Systems
ERTS	Earth Resources Technology Satellite
ESA	European Space Agency
ETM	Enhanced Thematic Mapper
ETM+	Enhanced Thematic Mapper plus
FOV	Field Of View

FWHM	Full Width at Half Maximum
GCP's	Ground Control Points
GER	Geophysical Environmental Research Corporation
GFZ	GeoResearch Center
GIS	Geographic Information System
GMT	Greenwich Mean Time
GPS	Global Positioning System
HATCH	High Accuracy ATmospheric Correction for Hyperspectral data
HIS	Hyperspectral Imaging
HRG	High Resolution Geometric
HRV	High Resolution Visible
HRVIR	High Resolution Visible and InfraRed
HyMAP	Hyperspectral Mapper
IARR	Internal Average Relative Reflectance
IFOV	Instantaneous FOV
IN	Institute for Nature Conservation
INS	Inertial Navigation System
IOCCG	International Ocean Colour Coordinating group
IRS	Indian Remote Sensing (satellites)
KHAT	Kappa coefficient
Landsat	Land Resources Satellite
LDA	Linear Discriminant Analysis
MERIS	Medium Resolution Imaging Spectrometer
METI	Ministry of Economy Trade and Industry
MIR	Middle InfraRed (interval of the EM spectrum)
MNF	Minimum Noise Fraction
MODTRAN	MODerate spectral resolution atmospheric TRANsmittance algorithm and computer model
MSS	Multi Spectral Scanner
NAP	Non-Algae Particles
NASA	National Aeronautical and Space Agency
NDVI	Normalized Difference Vegetation Index
NERC	Natural Environment Research Council
NIR	Near-infrared (interval of the EM spectrum)
P (code)	Precision (code)
PAR	Photosynthetically Available Radiation
PCA	Principle Components Analysis
PPI	Pixel Purity Index
PRISM	Panchromatic Remote-Sensing Instrument for Stereo Mapping
PROBA	Project for On Board Autonomy (mission)
PTFE	PolyTetraFluoroEthylene
RMS	Root Mean Square
RMSE	Root Mean Square Error
ROI	Regions Of Interest
ROSIS	Reflective Optics System Imaging Spectrometer
RTCM	Radio Technical Commission for Maritime Services

RTK	Real-Time Kinematic
SAM	Spectral Angle Mapper
SASI	Short wave infrared Airborne Spectrographic Imager
SeaWiFS	Sea-viewing Wide Field-of-View Sensor
SFF	Spectral Feature Fitting
SHP	shape-format
SI	Système International
SIS	Scanning Imaging Spectroradiometer
SMACC	Sequential Maximum Angle Convex Cone
SNSB	Swedish National Space Board
SPOT	Système Probatoire pour l'Observation de la Terre
SRU	Spectral Radiance Unit
SWIR	Short Wave InfraRed (interval of the EM spectrum)
TIR	Thermal InfraRed (interval of the EM spectrum)
TM	Thematic Mapper
TOA	Top-Of-Atmosphere
TSM	Total Suspended Matter
VIS	VISible (interval of the EM spectrum)
VNIR	Visible and Near-infrared (interval of the EM spectrum)
WAAS	Wide Area Augmentation System
WATCOR	Water ATmospheric CORrection
WGS84	World Geodetic System 1984

---

---

---

---

---

## Footnotes

- <sup>1</sup> A stationary signal is a signal that repeats into infinity with the same periodicity. (Page 54)
- <sup>2</sup> Originally applied to momentum and location of moving particles in Quantum Physics (Page 54)
- <sup>3</sup> Overfitting occurs when a classifier is too much focused on the training samples and is not able to classify new (unknown) samples well. (Page 58)